Dynamics of the storage ring free electron laser : theoretical and experimental study of two SRFELSs in Europe

Dynamics of the storage ring free electron laser: theoretical and experimental study of two SRFELs in Europe

by Cyrille Thomas

Omslagontwerp: J.W. Luiten, JWL producties
Druk: Universiteitsdrukkerij, TUE

CIP-DATA LIBRARY TECHNISCHE UNIVERSITEIT EINDHOVEN

Thomas, Cyrille A.

Dynamics of the storage ring free electron laser: theoretical and experimental study of two SRFELs in Europe / by Cyrille A. Thomas. -
Eindhoven : Technische Universiteit Eindhoven, 2003. -
Proefschrift. - ISBN 90-386-1685-6
NUR 924
Trefwoorden: vrije-elektronenlasers / nietlineaire dynamische systemen / opslagringen
Subject headings: free electron lasers / nonlinear dynamical systems / storage rings

Dynamics of the storage ring free electron laser: theoretical and experimental study of two SRFELs in Europe

PROEFSCHRIFT

ter verkrijging van de graad van doctor aan de Technische Universiteit Eindhoven, op gezag van de Rector Magnificus, prof.dr. R.A. van Santen, voor een commissie aangewezen door het College voor Promoties in het openbaar te verdedigen op dinsdag 27 mei 2003 om 16.00 uur

door

CYRILLE ALAIN THOMAS

geboren te Pessac, Frankrijk

Dit proefschrift is goedgekeurd door de promotoren:

prof.dr.ir. M.J. van der Wiel
en
prof.dr. M.E. Couprie

Copromotor:
dr. J.I.M. Botman

This research was supported by the European project number ERBFMRXC 980245 and was carried out within the framework of a 'co-tutelle' agreement with the Université Paris IX (Orsay, Fr).

...One ring to rule them all...

J.R.R. Tolkien (1892-1973)
Lord of the rings (1954)

à *ma mère*,

à *mon père*,

à *ma soeur*,

à *Sigolène*.

Contents

List of Tables

Chapter 1

Introduction

1.1 Introduction

Free Electron Lasers (FELs) are coherent and powerful lasers, continuously tunable in wavelength. Their principle lies in the interaction of light with a relativistic electron (or positron*) beam that travels through the permanent and periodical magnetic field of an undulator.
Based on the work of Motz† [1] and Phillips [2], Madey proposed a device at Stanford in 1971 [3], analogous to the 'ubitron' invented by Phillips‡. He named it 'free electron laser' to distinguish it from atomic lasers in which the electron is bound in an atom.
From the general concept, several free electron laser configurations have been developed: the first one, which has been demonstrated in 1976 by Madey and his team [4], consists of using relativistic electrons as an amplifier of a laser pulse. The second configuration is the 'oscillator' configuration: while traversing the undulator the relativistic electrons have a periodic trajectory in the transverse plane, and they emit electromagnetic radiation (Bremsstrahlung), called synchrotron radiation, which is the spontaneous emission of the free electron laser. The synchrotron radiation spectrum is composed of light at a fundamental wavelength, at a wavelength called the undulator resonant wavelength, and of the higher harmonics of resonant wavelength. Once stored in an optical cavity, the spontaneous emission may interact with relativistic electrons traversing periodically the undulator in the cavity. The successive interaction leads to the amplification of the spontaneous emission. An FEL based on this configuration was demonstrated for the first time by Madey in 1977 [5]. The amplifier configuration can be used for 'harmonic generation' [6]: an external laser or an FEL in an oscillator configuration interacts with electron bunches; this interaction provides energy modulation, and the energy modulation leads to a micro-bunching of the electron bunches at the resonant wavelength; once micro-bunched the electrons can then amplify coherently the harmonics of the resonant wavelength. A following free electron laser configuration

*In this thesis we discuss the case of electrons only, positrons have the same properties with regard to the FEL.

†Motz proposed that a periodic magnetic structure, which he termed an "undulator", could be used to generate quasi-monochromatic electromagnetic radiation from microwaves up to hard X-rays using electron beams with energies in the 1 MeV to 1 GeV range.

‡Phillips in 1957 invented a device called 'ubitron' which uses an undulator and a low energy electron beam to achieve amplification of microwave radiation.

is known as the Self Amplified Spontaneous Emission system (SASE): the electrons cross a long undulator and amplify their own radiation. The interaction between the synchrotron radiation and the electrons is sufficiently strong that saturation occurs in one pass at the end of the undulator. This has been proposed by Dattoli [7], Pelligrini [8] and Kim [9]. The first SASE FEL was demonstrated at Brookhaven [10]. Nowadays several groups in the world operate a SASE FEL [11]-[12]-[13]-[14]-[15]-[16].
The accelerators used to provide relativistic electrons for the FEL are generally linear accelerators (Linac), giving a Linac based FEL, or storage rings, giving a storage ring FEL (SRFEL).
The fundamental resonant wavelength of the spontaneous emission is in the case of a planar undulator:

$$\lambda_r = \frac{\lambda_u}{2\gamma_0^2}\left(1 + \frac{K^2}{2}\right), \tag{1.1}$$

where λ_u is the period length of the undulator, γ_0 is the Lorentz factor of the relativistic electrons, $K = \frac{eB_u\lambda_u}{2\pi m_e c}$ is the undulator strength, with B_u the maximum amplitude of the periodical magnetic field in the undulator, m_e the electron rest mass, e the electron charge, and c the speed of light in vacuum. According to expression (1.1) the FEL is continuously tunable, by varying the electron energy, the undulator period length or the amplitude of the undulator magnetic field. In practice the electron energy is set to a value given by the linear accelerator or the storage ring and can be tuned to different values, the period length of the undulator is fixed, and the spectral tuning is obtained mainly by varying B_0 and then K.
The electron energy in a Linac varies between several tens of MeV and a few GeV, with the length of the linac varying between several meters, like FELIX [17] (The Netherlands) or CLIO [18] (France), to a few kilometers, like the proposed linac for the SASE FEL of the TESLA test facility [15] (Germany). In storage rings the electron energy is usually in the GeV range. At Super ACO the electron energy for the FEL is 0.8 Gev, and at ELETTRA 0.9 and 1.5 GeV. For an undulator with $\lambda_u = 10$ cm, and K betwwen 1 and 5, the electron energy of 10 MeV, the resonant wavelength is in the range from 195 to 1760 μm, and with an energy of 1 GeV, the wavelength lies in the range from 19 to 176 nm.
Figure (1.1) presents the scheme of an FEL in the oscillator configuration. Relativistic electron bunches traverse periodically the undulator in the optical cavity, and emit spontaneous emission. The pulse interacts with the subsequent electron bunches and is amplified. The laser starts up and, as the intensity increases in the optical cavity, the maximum micro-bunching is reached at a shorter distance in the undulator, and the induced energy spread to the electrons is more and more important. When the energy spread is too large the gain decreases rapidly to the saturation level.
According to the Madey theorem [4], the gain, in the approximation of a small gain and small signal, is proportional to the derivative of the spontaneous emission spectrum, and is given by:

$$G \propto \frac{\partial}{\partial\nu}\left(sinc\left(2\pi N_u\nu\right)\right)^2, \tag{1.2}$$

with the function $sinc(x) = \frac{sin(x)}{x}$, and N_u the number of undulator periods, ν the spectral detuning given by $\nu = 2\pi\, N_u\, \frac{\lambda-\lambda_r}{\lambda_r}$. The number of eigenmodes of the optical

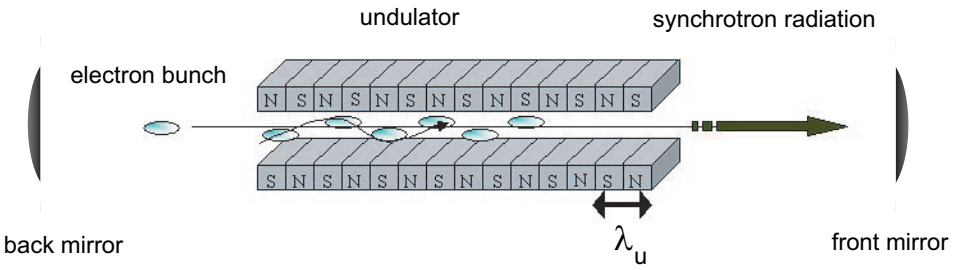

Figure 1.1: *Scheme of an FEL in the oscillator configuration: the relativistic electron bunch traverses the permanent periodical magnetic field of the undulator in the laser optical cavity and emits synchrotron radiation, which is the spontaneous emission of the laser. The successive interaction with the light pulse and the traversing electron bunches leads to the laser amplification. The saturation of the laser, due to the intra-cavity intensity of the laser, occurs when the electron bunch energy spread is so degraded that the gain reaches the level of the cavity loss.*

cavity that can be amplified can be calculated by the convolution of the gain expression with the infinite set of eigenmodes (represented by the Dirac comb distribution) and subtracting the cavity loss (η) (figure 1.2). As an example, one can consider the 18 m long cavity of the Super ACO FEL: the spectral free interval between the eigenmodes is given by $\nu_q = q\frac{c}{L_c}$, which give for Super ACO $\nu_q \approx 16.66\,q$ MHz (L_c being the cavity length). The eigenmode set is given by $f(\nu) = \sum_{q=-\infty}^{\infty} \delta(\nu - \nu_q)$ (with δ the Dirac functional). With the resonant wavelength $\lambda_r = 300$ nm, and the number of undulator periods $N_u = 50$, the spectral width $\Delta\nu \approx \frac{\nu}{2\,N_u}$ is of the order of 10^{13}. The number of eigenmodes that can be amplified is then of the order of 10^4. Compared to the spectral width of the spontaneous emission the laser spectral width is much smaller. In addition most of the amplified modes are in phase: the periodic structure of the electron beam provides a kind of mode locking, therefore the pulse duration tends to a minimum. The laser pulse duration ($\sigma_{Las} \leq 10$ ps) is then much shorter than the synchrotron radiation pulse (typically one order of magnitude). As a further example the spectral resolution, $\frac{\Delta\lambda}{\lambda}$, with $\Delta\lambda$ the spectral width at the laser wavelength λ, is around $3\,10^{-4}$ at the storage ring Super ACO. This value is between the Fourier limit[§] and the spectral width of the synchrotron radiation pulse. The laser pulse here is naturally synchronized with the synchrotron light pulse (from a bending magnet), which has a large broadband continuous spectrum.
The characteristics of the SRFELs, short pulses in the UV-VUV range and high spectral resolution, tunability and high repetition rate (MHz), are interesting tools for UV-VUV spectroscopy [19] as well as micro-spectroscopy [20]. Moreover they are unique for time resolved multi-photon spectroscopy [21]-[22]-[23]-[24]. The gain scales as $\frac{N_u^3\,\lambda_u^2\,K^2}{\gamma^3}$ (see chapter 2). For short wavelength a high electron energy is needed. A sufficient gain is needed for the lasing condition, e.g. a gain larger than the total cavity loss. This gives some problems: the undulator length $L_{und} = N_u\lambda_u$ is limited by the storage ring

[§]The Fourier Limit is given by the following expression: $\sigma_{Las}\dfrac{\Delta\lambda}{\lambda^2} = 1$

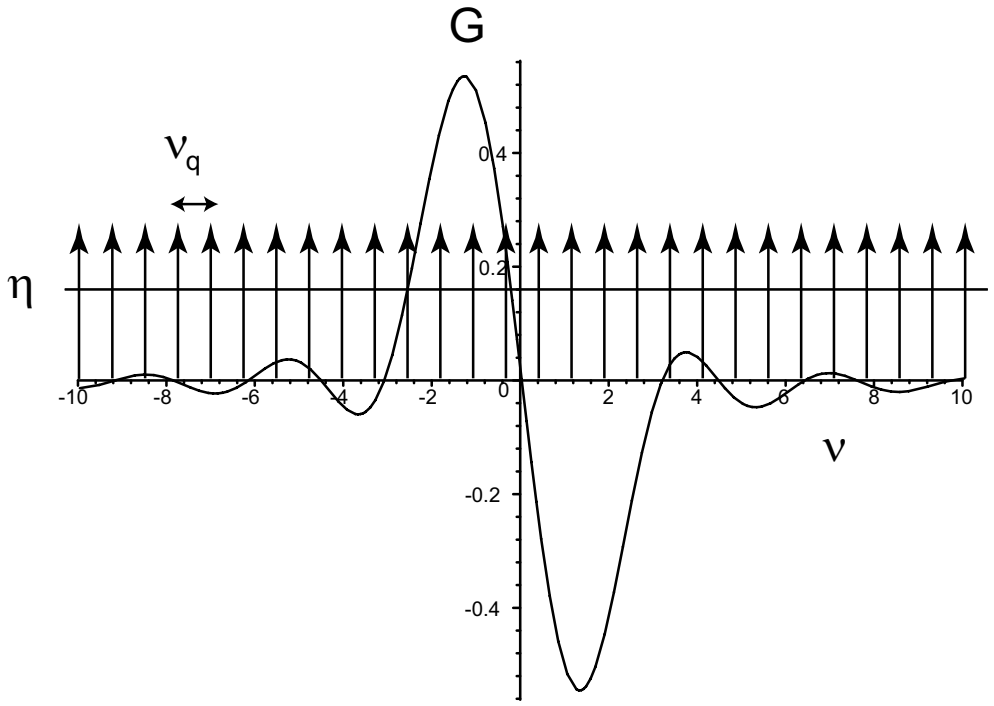

Figure 1.2: *Madey gain curve, $G(\nu)$. The eigenmodes of the optical cavity are represented schematically by the Dirac comb distribution, separated by the free spectral interval of the cavity, ν_q. The cavity loss, η, gives the level above which the gain is effective.*

straight section so that in general the gain in the UV-VUV domain is rather small. Consequently drastic requirements on the mirrors are needed [25]. In order to optimize the transmission through the mirrors and extract the maximum power, a very low absorption, less or much less than 1 %, is required. The mirrors are exposed to spontaneous emission which has a broadband spectrum covering the range from the fundamental wavelength, λ_r, to higher harmonics in the X-ray domain, with up to 10^{16} photons s^{-1} mm^{-2} rad^{-2}. In planar undulators this hard radiation causes heating of the mirrors and more important damage than in helical undulators, which has been observed first at UVSOR [26], so that their absorption in the UV-VUV increases [27]. These facts motivated studies for VUV optics [28], for the development of new diagnostics to analyze and understand the damage and for providing higher performing mirrors [29]-[30].

User applications require a stable and generally a powerful laser. In order to achieve this, stability of the optical cavity is needed, as well as a stable electron beam. A perfect isolation of the optical cavity from any mechanical or acoustical vibration, from heating, etc. is in general sufficient to stabilize the optical cavity. A stable electron beam for the operation of the FEL is then an issue, which can be reached by a deep understanding of the dynamics. A model in confrontation to experiments may provide enough knowledge to control the beam behavior.

The electrons are stored in a ring so that the same electrons interact at each passage in the optical cavity with the laser pulse. The FEL interaction leads to electron enhancement of the energy spread, which causes the stored relativistic electron bunch

in the ring to lengthen. The laser gain is strongly dependent on the electron bunch quality, which is degraded by the laser intensity. Due to the fact that the electrons are not refreshed at each passage, as in a Linac based FEL, there is a strong non-linear coupling between the electrons and the laser dynamics. The coupled dynamics is highly non-linear and sufficiently complex in itself that providing a good model is already challenging. Moreover a model that is able to describe the coupled dynamics in quantitative agrement with measurements also needs to take into account the instabilities that may occur in the electron bunch and in the laser pulse. Instabilities in the electron beam are most damageable to the laser operation, they induce jittering in position and in the spectrum [31], while they also induce intensity fluctuations.
The most observed longitudinal instability in storage rings is the so-called microwave instability [32]. This instability may be considered as the main longitudinal instability, which may degrade the electron beam quality so that the laser performance is affected. Taking into account the microwave instability, as it will be presented in this thesis, leads to a relatively good agreement between theoretical and experimental results on the laser dynamics. It gives a clearer picture of the complex dynamics, in particular the description of competition between the laser and the beam instabilities [33]-[34]. Moreover it gives the possibility to optimize the laser performance. In addition it shows that the laser is able to damp the instabilities. If it can not damp them then feedback systems [35]-[36] are necessary to stabilize the electron beam and consequently the laser.

1.2 State of the art

The first storage ring free electron laser operating in an oscillator configuration was on the $e^+ - e^-$ collider ring ACO, in Orsay (France) in 1983 [37]. This storage ring was used at that time as a synchrotron light source. The wavelength of the emission was in the visible range. The second storage ring free electron laser was at VEPP3 in Novosibirsk in 1988 [38].
Since the first FEL photons at ACO [37] considerable efforts have been made to make SRFELs suitable sources for applications. The first application of the FEL was demonstrated at Super ACO in 1993 [19]. Then the development of UV-VUV mirrors allowed the SRFEL to reach smaller wavelengths, in particular the smallest wavelength has been reached recently at ELETTRA with 189 nm [39] and and was 193 nm at DUKE [40]. Development and improvement of optical klystrons provided higher gain, and smaller spectral bandwidth, $\frac{\Delta\lambda}{\lambda}$, was achieved, down to 10^{-6} at 350 nm at VEPP 3 [41] using a Fabry-Perot in the optical cavity. Harmonic generation was demonstrated for the first time at Super ACO, providing an amplified pulse at 105 nm [6], and due to the development of this technique combined with the improvement of the beam emittance of storage rings, the FEL group at DUKE achieved recently harmonic generation at 80 nm. The performance of SRFELs makes them an interesting light source for applications. To dedicate more time for applications with these sources, the stability of the electron beam remains an issue, as it is observed at ELETTRA and DUKE. At the moment six SRFEL operate worldwide in the UV-VUV range: the Super ACO FEL (France), the ELETTRA (Italy), and FELICITA 1 (DELTA FEL, Germany), in Europe; the UVSOR FEL and the NIJI IV in Japan; the DUKE FEL in the United

Table 1.1: *SRFELs in the world and their characteristics*

SRFEL	Super ACO	ELETTRA	Duke	UVSOR	NIJI IV
Location	France	Italy	North Carolina (USA)	Japan	Japan
Energy (GeV)	0.8	0.9-1.5	1.2	0.75	1.5
Spectral range (nm)	450-300	350-189	730-193	700-238	750-211
Average power (W)	0.3	0.6	$3\ 10^{-3}$	1.2	-
@ wavelength (nm)	350	250	193	570	-
repetition rate (MHz)	8.3	4.6	11.1	11.2	20.2
pulse duration (ps)	7	3	3	7	5
Spectral resolution (10^{-4})	3	3	2	3	3
User Facility	yes	yes	yes	yes	no

States. Table (1.1) presents the main characteristics of these modern SRFELs.

1.3 Scope and outline of the thesis

Methodology

A storage ring free electron laser is a non-linear dynamical system. For investigating it, different approaches can be followed. First an experimental study is necessary to characterize the laser and its dynamics. Understanding and controlling the laser requires further experimental and theoretical study. In this thesis the goal is to develop a dynamical model for the interaction between the laser and the electron bunch, taking into account the microwave instability, and compare the results with the measurements.
When analytical modelling of the dynamical system can not be done, i.e. when the results of the modelling do not lead to an analytical expression that can be evaluated, which is often the case with non-linear systems, one has to rely on numerical simulations. In this thesis, the behavior of the SRFEL will be studied both theoretically, numerically, and experimentally.

Scope of the thesis

This thesis work, carried out mostly at the Technische Universiteit Eindhoven and at the L.U.R.E. laboratory of Université Paris Sud, is also part of the activities of a European network titled "Towards a storage ring free electron laser at 200 nm", which was funded 4 year ago. In particular the thesis work benefited from a close collaboration with the theoretician group of E.N.E.A Frascati leaded by G. Dattoli. Measurements at ELETTRA have been performed with the FEL group of ELETTRA leaded by R. walker. The main network objective was to acquire the knowledge necessary to operate SRFELs at 200 nm or below. To this end special studies have been devoted to the optics of the FEL, i.e. to the performance of the mirrors, and to the control of

the SRFEL dynamics, both being crucial for the SRFEL operation. At the same time developments of SRFELs as a light source, as well as of the applications like two-colors time-resolved spectroscopy were carried out. Concerning the SRFEL dynamics it was observed that although the theory and simulation codes explained many important features of the SRFEL dynamics, a satisfactory knowledge of the behavior of this system in real experimental conditions was still missing. In particular the investigation and the modelling of the instabilities in the electron beam due to their interaction with nearby media, the most important instability being the microwave instability, had to be done in a more extensive way.

The aim of the thesis is to increase the knowledge on the SRFEL dynamics in presence of instabilities such as the microwave instability, in order to predict the SRFEL behavior. We implemented a numerical code, 1-dimensional[¶] as a first step, to understand and predict the behavior of the SRFEL in the presence of the microwave instability. The simulations have been validated through the comparison with experiments. An experimental study has been carried out at Super ACO and at ELETTRA in order to understand the dynamics from an experimental point of view, and further to provide the system data required for comparison with the simulation results. The foundation of the theory of SRFELs has been mainly developed in Europe, in particular by Dattoli and Renieri [42]-[43] at E.N.E.A. Frascati (Italy), and we have based all our theoretical approaches on the theory developed there. In Japan, the models developed are based mostly on a phenomenological approach [44]: essentially a heuristic model based on the Sands equations [45], where a phenomenological model of the interaction of electrons with the vacuum chamber has been included; an interesting model has also been developed by Hara during his PhD thesis at Orsay [46], which focuses on the spectral multi-mode analysis. The group in Orsay has also developed heuristic models providing breakthrough in the understanding of the dynamics, in particular in the saturation of an SRFEL [47]. In DUKE, the model used to predict the SRFEL dynamics is a 3-dimensional code developed by Litvinenko [48], which is based on a model developed at Novosibirsk (Russia), solving the Fokker-Planck equations coupled with the 3-dimensional propagation equations of the laser.

We based our theoretical approach on the work of Dattoli and Renieri because we think that it combines the intuitive approach and the understanding from the heuristics model, with the rigorous approach of self-consistent theory.

The results we obtained so far have increased the level of knowledge of the SRFEL dynamics. Experiments and simulations have shown the importance of the microwave instability and how crucial it is to take that instability into account in the SRFEL dynamics. Relatively good agreement between simulations and experiments has been found. This allows to make predictions on the current range where to operate the laser, at what power, wavelength range and pulse duration, which is essential for user applications. The experimental study invited us to develop partly the theory concerning the instabilities of the electron beam and in particular to solve analytically the Haissinski equation for a purely inductive impedance of the storage ring vacuum chamber. The

[¶]The dimensionality of the code is defined by the spatial dimension: a code simulating the behavior of the laser pulse along the propagation axis is called 1-dimensional. If the same code simulates the behavior of the laser pulse along the propagation axis and in the transverse axis, assuming cylindrical symmetry, then the code is called 2-dimensional, etc. A code simulating the evolution of the laser intensity only is called 0-dimensional.

Super ACO FEL and ELETTRA FEL have an optical klystron[‖] in the optical cavity instead of an undulator, and the modelling of the laser dynamics is developed in this thesis for both the undulator and the optical klystron cases.

Outline of the thesis

A first introduction to the FEL physics describing the main properties of the laser will be presented in chapter 2. To study the behavior of the laser, it is important to characterize the dynamics of the electrons in the ring, in particular in presence of the microwave instability, which is observed in all storage rings. The study of the beam dynamics in presence of the microwave instability is shown in chapter 3. In a second part of chapter 3 we treat the behavior of the whole system, i.e. the laser coupled with the electron beam. We present a numerical code, describing the behavior of the system, and we use it to investigate the behavior of existing SRFELs, like the FEL at Super ACO or at ELETTRA. This code has been implemented using a one-dimensional model, where three differential equations accounting for the laser complex electric field, for the electron beam energy spread and for the microwave instability, are integrated. In parallel, experimental characterization of SRFELs has been performed at Super ACO as well as at ELETTRA, and the experimental behavior of these two representative systems is given in chapters 4 and 5. Diagnostics on the beam and the laser have been used to investigate the interaction between the laser and the electron beam. Finally, in chapter 5 a comparison between the numerical results and the measurements is done, showing the importance of modelling the instabilities of the beam and their effect on the laser dynamics.

References

[1] H. Motz. Applications of the radiation from fast electron beams. *Journal of Applied Physics*, 22:5, May 1951.

[2] R.M. Phillips. The ubitron, a high power traveling-wave tube based on a periodic beam interaction in an unloaded waveguide. *I.R.E. Trans. Electron Dev.*, 7:231, 1960.

[3] J. M. J. Madey. Stimulated emission of bremmstrahlung in a periodinc magnetic field. *Jounal of Applied Physics*, 42(5):1906, 1971.

[4] L. R. Elias, W. M. Fairbank, J.M.J. Madey, H.A. Schwettman, and T.I. Smith. Observation of a stimulated emission of radiation by relativistic electrons in a spatially periodic transverse magnetic field. *Physical Review Letters*, 36:717–720, 1976.

[5] D. A. G. Deacon, L. R. Elias, J. M. J. Madey, G. J. Ramian, H. A. Schwettman, and T. I. Smith. First operation of a free-electron laser. *Physical Review Letters*, 38:892, April 1977.

[‖] An optical klystron is simply two undulators separated by a dispersive section. A description is given in chapter 2.

[6] R. Prazeres, P. Guyot-Sionnest, J. M. Ortega, M. Billardon, and D. Jaroszynski. Production of VUV coherent light by harmonic generation with the optical klystron of super-ACO. *IEEE Journal of Quantum Electronics*, 27:1061–1068, April 1991.

[7] G. Dattoli, A. Marino, A. Renieri, and F. Romanelli. Progress in the Hamiltonian picture of the free-electron laser. *IEEE Journal of Quantum Electronics*, 17:1371, August 1981.

[8] R. Bonifacio, C. Pellegrini, and L. M. Narducci. Collective instabilities and high-gain regime in a free electron laser. *Optics Communications*, 50:373–378, July 1984.

[9] K.J. Kim. Three-dimensional analysis of coherent amplification and sefl amplified spontaneous emission in free electron lasers. *Physical Review Letters*, 57(15):1871–1874, 1986.

[10] M. Babzien, I. Ben-Zvi, P. Catravas, J.-M. Fang, T. C. Marshall, X. J. Wang, J. S. Wurtele, V. Yakimenko, and L. H. Yu. Observation of self-amplified spontaneous emission in the near-infrared and visible wavelengths. *Physical Review E*, 57:6093–6100, May 1998.

[11] M. Hogan, C. Pellegrini, J. Rosenzweig, G. Travish, and A. A. Varfolomeev. The UCLA high gain infrared free electron laser. *Nuclear Instruments and Methods in Physics Research A*, 393:216–219, February 1997.

[12] M. Hogan, C. Pellegrini, S. Reiche, J. Rosenzweig, G. Travish, A. Tremaine, S. Anderson, K. Bishofberger, P. Frigola, A. Murokh, and A. Varfolomeev. High Gain SASE FEL Studies at UCLA. In *American Physical Society, Particle Acceleration Meeting, May 12-16, 1997, abstract #4B.11*, page 4, May 1997.

[13] S. V. Milton, E. Gluskin, S. G. Biedron, R. J. Dejus, P. K. den Hartog, J. N. Galayda, K.-J. Kim, J. W. Lewellen, E. R. Moog, V. Sajaev, N. S. Sereno, G. Travish, N. A. Vinokurov, N. D. Arnold, C. Benson, W. Berg, J. A. Biggs, M. Borland, J. A. Carwardine, Y.-C. Chae, G. Decker, B. N. Deriy, M. J. Erdmann, H. Friedsam, C. Gold, A. E. Grelick, M. W. Hahne, K. C. Harkay, Z. Huang, E. S. Lessner, R. M. Lill, A. H. Lumpkin, O. A. Makarov, G. M. Markovich, D. Meyer, A. Nassiri, J. R. Noonan, S. J. Pasky, G. Pile, T. L. Smith, R. Soliday, B. J. Tieman, E. M. Trakhtenberg, G. F. Trento, I. B. Vasserman, D. R. Walters, X. J. Wang, G. Wiemerslage, S. Xu, and B.-X. Yang. Observation of Self-Amplified Spontaneous Emission and Exponential Growth at 530 nm. *Physical Review Letters*, 85:988–991, July 2000.

[14] J. W. Lewellen, S. V. Milton, E. Gluskin, N. D. Arnold, C. Benson, W. Berg, S. G. Biedron, M. Borland, Y.-C. Chae, R. J. Dejus, P. K. D. Hartog, B. Deriy, M. Erdmann, Y. I. Eidelman, M. W. Hahne, Z. Huang, K.-J. Kim, Y. Li, A. H. Lumpkin, O. Makarov, E. R. Moog, A. Nassiri, V. Sajaev, R. Soliday, B. J. Tieman, E. M. Trakhtenberg, I. B. Vasserman, N. A. Vinokurov, G. Wiemerslage, and B. X. Yang. Present status and recent results from the APS SASE FEL. *Nuclear Instruments and Methods in Physics Research A*, 483:40–45, May 2002.

[15] C. Pagani, E. L. Saldin, E. A. Schneidmiller, and M. V. Yurkov. Design considerations and analysis of potential applications of a high power ultraviolet FEL at the TESLA test facility at DESY. *Nuclear Instruments and Methods in Physics Research A*, 423:190–202, February 1999.

[16] J. Andruszkow, B. Aune, V. Ayvazyan, N. Baboi, R. Bakker, V. Balakin, D. Barni, A. Bazhan, M. Bernard, A. Bosotti, J. C. Bourdon, W. Brefeld, R. Brinkmann, S. Buhler, J.-P. Carneiro, M. Castellano, P. Castro, L. Catani, S. Chel, Y. Cho, S. Choroba, E. R. Colby, W. Decking, P. den Hartog, M. Desmons, M. Dohlus, D. Edwards, H. T. Edwards, B. Faatz, J. Feldhaus, M. Ferrario, M. J. Fitch, K. Flöttmann, M. Fouaidy, A. Gamp, T. Garvey, C. Gerth, M. Geitz, E. Gluskin, V. Gretchko, U. Hahn, W. H. Hartung, D. Hubert, M. Hüning, R. Ischebek, M. Jablonka, J. M. Joly, M. Juillard, T. Junquera, P. Jurkiewicz, A. Kabel, J. Kahl, H. Kaiser, T. Kamps, V. V. Katelev, J. L. Kirchgessner, M. Körfer, L. Kravchuk, G. Kreps, J. Krzywinski, T. Lokajczyk, R. Lange, B. Leblond, M. Leenen, J. Lesrel, M. Liepe, A. Liero, T. Limberg, R. Lorenz, L. Hua, L. Hai. First Observation of Self-Amplified Spontaneous Emission in a Free-Electron Laser at 109 nm Wavelength. *Physical Review Letters*, 85:3825–3829, October 2000.

[17] D. Oepts, A. F. G. van der Meer, and P. W. van Amersfoort. The free-electron-laser user facility felix. *Infrared Physics and Technology*, 36:297–308, January 1995.

[18] R. Prazeres, J. M. Berset, F. Glotin, D. Jaroszynski, and J. M. Ortega. Subpicosecond laser pulse generation on the CLIO FEL. *Nuclear Instruments and Methods in Physics Research A*, 358:212–215, February 1995.

[19] M. E. Couprie, F. Mérola, P. Tauc, D. Garzella, A. Delboulbé, T. Hara, and M. Billardon. First use of the UV Super-ACO free-electron laser: Fluorescence decays and rotational dynamics of the NADH coenzyme. *Review of Scientific Instruments*, 65:1485–1495, May 1994.

[20] M. Marsi, A. Locatelli, M. Trovò, R. P. Walker, M. E. Couprie, D. Garzella, L. Nahon, D. Nutarelli, E. Renault, A. Gatto, N. Kaiser, L. Giannessi, S. Günster, D. Ristau, M. W. Poole, and A. Taleb-Ibrahimi. UV/VUV Free Electron Laser Oscillators and Applications in Materials Science. *Surface Review and Letters*, 9:599–607, 2002.

[21] M. Couprie, E. Renault, D. Garzella, D. Nutarelli, G. de Ninno, F. Merola, and L. Nahon. Applications in biology with the super-ACO FEL and future prospects. In *Proc. SPIE Vol. 4633, p. 210-224, Commercial and Biomedical Applications of Ultrafast and Free-Electron Lasers, Glenn S. Edwards; Joseph Neev; Andreas Ostendorf; John C. Sutherland; Eds.*, volume 4633, pages 210–224, April 2002.

[22] E. Renault, L. Nahon, D. Garzella, D. Nutarelli, G. De Ninno, M. Hirsch, and M. E. Couprie. Transient absorption spectroscopy in biology using the Super-ACO storage ring FEL and the synchrotron radiation combination. *Nuclear Instruments and Methods in Physics Research A*, 475:617–624, December 2001.

[23] L. Nahon, E. Renault, M. Couprie, D. Nutarelli, D. Garzella, M. Billardon, G. L. Carr, G. P. Williams, and P. Dumas. Two-color experiments combining the UV storage ring free-electron laser and the SA5 IR beamline at Super-ACO. In *Proc. SPIE Vol. 3775, p. 145-154, Accelerator-based Sources of Infrared and Spectroscopic Applications, G. Lawrence Carr; Paul Dumas; Eds.*, volume 3775, pages 145–154, October 1999.

[24] M. Marsi, M. E. Couprie, L. Nahon, D. Garzella, R. Bakker, A. Delboulbé, D. Nutarelli, R. Roux, B. Visentin, C. Grupp, G. Indlekofer, G. Panaccione, A. Taleb-Ibrahimi, and M. Billardon. Two color experiments combining Free Electron Laser and Synchrotron Radiation. *Nuclear Instruments and Methods in Physics Research A*, 393:548–551, February 1997.

[25] D. Garzella, M. E. Couprie, and M. Billardon. Lasing at 300 nm and below: optical challenges and perspectives. *Nuclear Instruments and Methods in Physics Research A*, 375:39, February 1996.

[26] H. Hama, K. Kimura, M. Hosaka, J. Yamazaki, and T. Kinoshita. Testing for qualification of a helical optical klystron for UV storage-ring free electron lasers. *Nuclear Instruments and Methods in Physics Research A*, 393:23–27, February 1997.

[27] A. Gatto, R. Thielsch, N. Kaiser, M. Hirsch, D. Garzella, D. Nutarelli, G. de Ninno, E. Renault, M. Couprie, P. Torchio, M. Alvisi, G. Albrand, C. Amra, M. Marsi, M. Trovo, R. Walker, M. Grewe, S. Robert, J. P. Roger, and C. A. Boccara. Toward resistant UV mirrors at 200 nm for free electron lasers: manufacture, characterizations, and degradation tests. In *Proc. SPIE Vol. 4102, p. 261-275, Inorganic Optical Materials II, Alexander J. Marker; Eugene G. Arthurs; Eds.*, volume 4102, pages 261–275, October 2000.

[28] A. Gatto, N. Kaiser, R. Thielsch, D. Garzella, M. Hirsch, D. Nutarelli, G. de Ninno, E. Renault, M. Couprie, P. Torchio, M. Alvisi, G. Albrand, C. Amra, M. Marsi, M. Trovo, R. Walker, M. Grewe, J. P. Roger, and A. C. Boccara. Achromatic damage investigations on mirrors for UV-free electron lasers. In *Proc. SPIE Vol. 4347, p. 535-546, Laser-Induced Damage in Optical Materials: 2000, Gregory J. Exarhos; Arthur H. Guenther; Mark R. Kozlowski; Keith L. Lewis; M. J. Soileau; Eds.*, volume 4347, pages 535–546, April 2001.

[29] A. Gatto, J. Heber, N. Kaiser, D. Ristau, S. Günster, J. Kohlhaas, M. Marsi, M. Trovo, and R. P. Walker. High-performance UV/VUV optics for the Storage Ring FEL at ELETTRA. *Nuclear Instruments and Methods in Physics Research A*, 483:357–362, May 2002.

[30] A. Gatto, R. Thielsch, J. Heber, N. Kaiser, D. Ristau, S. Gunster, J. Kohlhaas, M. Marsi, M. Trovo, R. Walker, D. Garzella, M. Emmanuelle Couprie, P. Torchio, M. Alvisi, and C. Amra. High-Performance Deep-Ultraviolet Optics for Free-Electron Lasers. *Applied Optics*, 41:3236–3241, June 2002.

[31] M. E. Couprie. Storage ring free electron laser and longitudinal instabilities experiments. *Nuovo Cimento A Serie*, 112:475, May 1999.

[32] G. Dattoli, L. Mezi, A. Renieri, M. Migliorati, M. E. Couprie, R. Roux, D. Nutarelli, and M. Billardon. Storage-ring free-electron-laser dynamics and head-tail instability. *Physical Review E*, 58:6570, November 1998.

[33] G. Dattoli, A. Renieri, and G. Voykov. Storage-ring free-electron-laser amplifiers and the microwave instability. *Physical Review E*, 55:2056, February 1997.

[34] M. Migliorati, L. Palumbo, G. Dattoli, and L. Mezi. Saw-tooth instability in storage rings: simulations and dynamical model. *Nuclear Instruments and Methods in Physics Research A*, 437:134, November 1999.

[35] M. E. Couprie, D. Garzella, T. Hara, J. H. Codarbox, and M. Billardon. A longitudinal feedback for the Super-ACO free electron laser stability in the UV. *Nuclear Instruments and Methods in Physics Research A*, 358:374, February 1995.

[36] S. Koda, M. Hosaka, J. Yamazaki, M. Katoh, and H. Hama. Development of longitudinal feedback system for a storage ring free electron laser. *Nuclear Instruments and Methods in Physics Research A*, 475:211–216, December 2001.

[37] M. Billardon, J. M. Ortega, P. Elleaume, C. Bazin, M. Bergher, M. Velghe, Y. Petroff, D. A. G. Deacon, K. E. Robinson, and J. M. J. Madey. First operation of a storage-ring free-electron laser. *Physical Review Letters*, 51:1652–1655, October 1983.

[38] N. A. Vinokurov, I. B. Drobyazko, G. N. Kulipanov, V. N. Litvinenko, and I. V. Pinayev. Lasing in visible and ultraviolet regions in an optical klystron installed on the VEPP-3 storage ring (invited). *Review of Scientific Instruments*, 60:1435–1438, July 1989.

[39] M. Trovò, J. A. Clarke, M. E. Couprie, G. Dattoli, D. Garzella, A. Gatto, L. Giannessi, S. Günster, N. Kaiser, M. Marsi, M. W. Poole, D. Ristau, and R. P. Walker. Operation of the European storage ring FEL at ELETTRA down to 190nm. *Nuclear Instruments and Methods in Physics Research A*, 483:157–161, May 2002.

[40] T. J. Krupa. Duke free-electron laser breaks 2,000 angstrom wavelength barrier. *Optics & Photonics News*, 11:6, January 2000.

[41] V. N. Litvinenko, M. E. Couprie, N. G. Gavrilov, G. N. Kulipanov, I. V. Pinaev, V. M. Popik, A. N. Skrinskii, and N. A. Vinokurov. The results of lasing linewidth narrowing on VEPP-3 storage ring optical klystron. *IEEE Journal of Quantum Electronics*, 27:2560–2565, December 1991.

[42] A. Renieri. Storage ring operation of the free-electron laser - The amplifier. *Nuovo Cimento B Serie*, 53:160, September 1979.

[43] G. Dattoli, A. Torre, L. Mezi, J. C. Gallardo, and R. Caloi. Spectral structures of supermodes in free-electron lasers. *Physical Review A*, 39:4281, April 1989.

[44] H. Hama and M. Hosaka. Longitudinal beam dynamics and FEL interaction on a negative momentum compaction storage ring. *Nuclear Instruments and Methods in Physics Research A*, 429:172–178, June 1999.

[45] M. Sands. *The physics of electron storage ring, an introduction*, volume 121. SLAC report, November 1970.

[46] T. Hara. *Study of the free electron laser and its applications*. PhD thesis, Université Paris Sud, Orsay (France), July 1995.

[47] M. E. Couprie, T. Hara, D. Gontier, P. Troussel, D. Garzella, A. Delboulbé, and M. Billardon. Temporal dynamics of storage ring free electron lasers. *Physical Review E*, 53:1871, February 1996.

[48] V. N. Litvinenko, B. Burnham, J. M. J. Madey, and Y. Wu. Giant laser pulses in the Duke storage ring UV FEL. *Nuclear Instruments and Methods in Physics Research A*, 358:334, February 1995.

Chapter 2

SRFEL basic theory

2.1 INTRODUCTION

A storage ring free electron laser (SRFEL) in an oscillator configuration makes use of relativistic electron bunches circulating in the storage ring, and an undulator, in an optical cavity, traversed by the electron bunches at each turn (figure (2.1)). The undulator, which creates a periodic and permanent magnetic field, provides spontaneous emission (radiation emitted by the electron while traversing the undulator, the so-called synchrotron radiation). The interaction of relativistic electrons in the undulator with a light pulse leads to the laser gain. The first demonstration of an operating free electron laser was made by Madey [1] in 1977. The second operating free electron laser in the world was on a storage ring in 1983 at ACO* [2]. An SRFEL is a coupled system composed of an electron bunch circulating in a ring and a (free electron) laser oscillating in a cavity. The electron behaviour in the ring is fundamental to determine the laser dynamics. In this introductory chapter to the SRFEL dynamics we present first the electron beam dynamics in the ring. In the second part we present the free electron laser principle, calculating the spontaneous emission from which the laser starts, and then the laser gain. Once the gain is known, it is possible to build a simple model, based on a general laser equation coupled with an equation accounting for the electron beam energy spread, from which most of the dynamics can be retrieved.

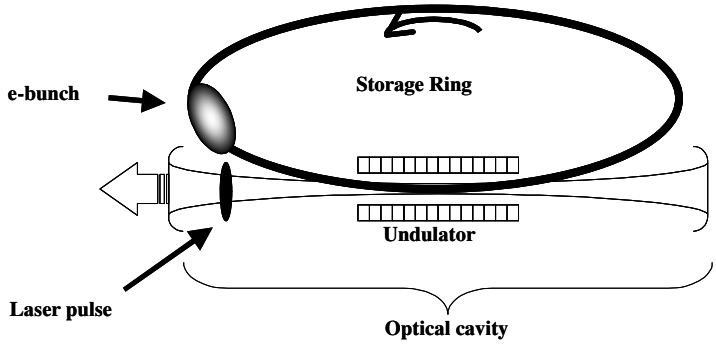

Figure 2.1: *Scheme of a storage ring free electron laser.*

*'Anneau de COllision', collider storage ring in Orsay, which has been shut down in 1988.

2.2 Stored electron beam in a ring

In storage rings the lattice describes the guiding magnetic field for the particles and defines a closed path. The guiding field is provided by a series of bending magnets and magnetic lenses (quadrupoles), which guide and focus the particles respectively. Figure (2.2) presents schematically a storage ring. The focussing by the lenses causes

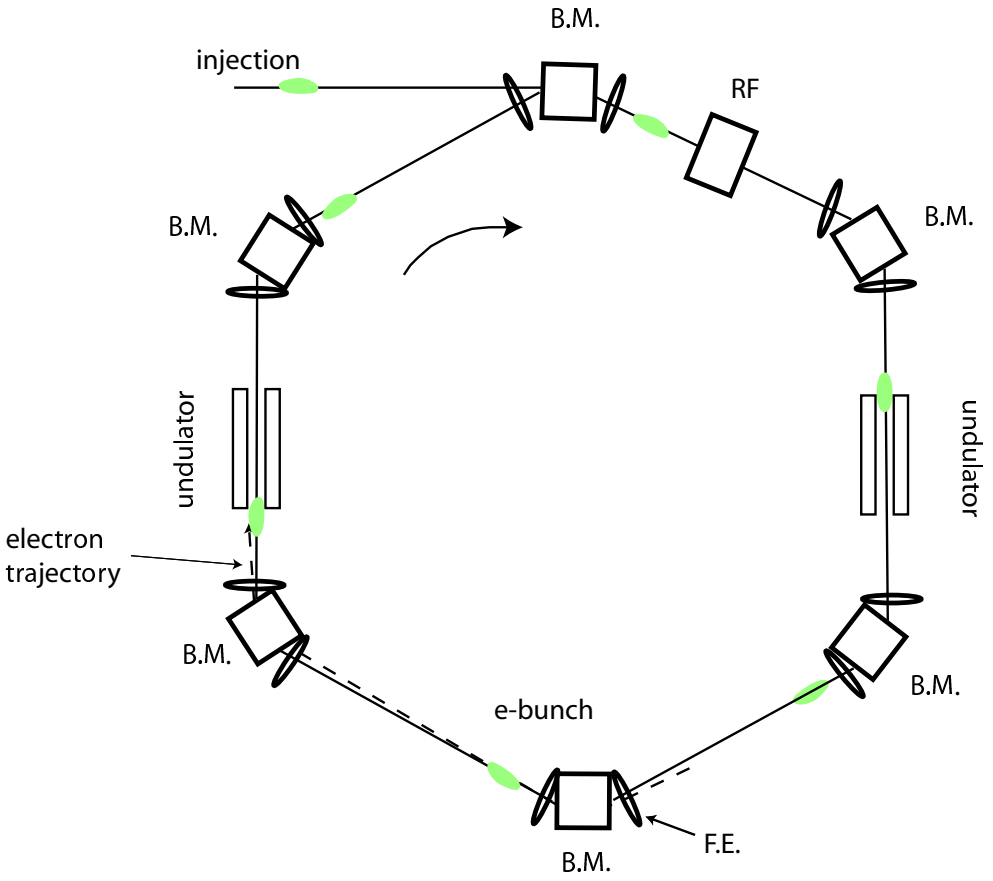

Figure 2.2: *Scheme of a storage ring. B.M. bending magnet, F.E. focusing element, RF, RF cavity, e-bunch: electron bunch. The trajectory of a sample electron undergoing betatron oscillation is represented by the dashed line.*

the electrons to oscillate in a lateral plane (vertical and radial) around the ideal orbit. This transverse oscillation is called the betatron motion. Along the path electrons bend in bending magnet or in insertion devices like undulators, and emit synchrotron radiation and loose a certain amount of energy. The synchrotron radiation has been used since the 60's as a light source for a large field of scientific applications [3]. To store the electron in the lattice the energy loss in one turn is compensated by the corresponding gain from the electric field of a radio-frequency (RF) cavity. The periodic RF field collects electrons into bunches circulating in the ring. The energy loss from synchrotron radiation together with the energy recovery from the RF field cause the electrons to oscillate in energy and in position around a reference particle, which has the nominal energy for the given lattice and is in phase with the RF field. This particle is called the synchronous particle, and the longitudinal oscillation is the synchrotron oscillation. The energy oscillations are damped with a typical time, τ_s, depending on

the RF field and the electron energy, which is called the synchrotron damping time.
The closed path is determined by the bending magnets (dipole magnets) providing a region where the magnetic field is constant. When electrons enter a bending magnet, they undergo the Lorentz force $\overrightarrow{F} = e\overrightarrow{v_e} \times \overrightarrow{B}$ and follow a circular trajectory. Their radius of curvature is given by:

$$\rho_0 = \frac{E_0}{e\,c\,B}, \tag{2.1}$$

with e the electron charge, v_e the electron velocity, $\overrightarrow{B} = B\hat{y}$ the magnetic field of the bending magnet, E_0 the nominal electron energy, c the speed of light in vacuum. The field of the magnet is adapted to the electron energy.
Figure (2.3) presents the coordinate system used to describe the electron dynamics in the ring.

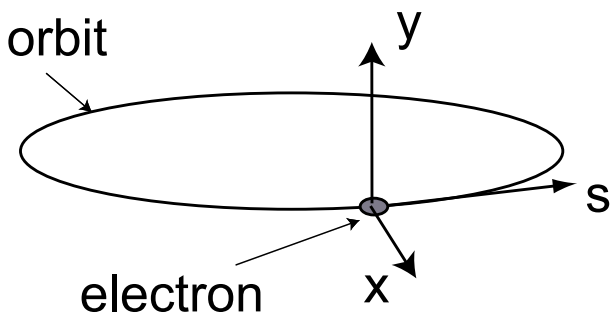

Figure 2.3: *Coordinate system in the storage ring.*

While being bent the electrons emit synchrotron radiation and loose energy. The total amount of energy lost by an electron in one turn is given by [4]:

$$U_0 = \frac{C_\gamma\, E_0^4}{\rho_0}, \tag{2.2}$$

with $C_\gamma = \dfrac{4\pi\, r}{3\ (m_e c^2)^3} \simeq 8.858\, 10^{-5} [mGeV^{-3}]$, r the classical electron radius and m_e the electron rest mass.
Due to the energy variation ($\epsilon = E - E_0$) the electrons have a different period ($T_0 + \delta T_0$) and as a consequence they undergo an orbit length variation ($L + \delta L$). This can be expressed as follows [4] :

$$\frac{\delta T_0}{T_0} = \frac{\delta L}{L} = \alpha_c \frac{\epsilon}{E_0}. \tag{2.3}$$

where α_c is the momentum compaction factor, given by

$$\alpha_c = \frac{1}{\rho_0 L} \int_L \eta_x\,(s)\, ds \tag{2.4}$$

with $\eta_x\,(s)$ the dispersion function of the lattice [4], which gives the horizontal displacement of the particle as a function of the energy at the coordinate s. The values defined here can be seen for Super ACO and ELETTRA in table (2.1).

2.2.1 Electron beam energy spread

Electromagnetic radiation is a quantum process and the radiated electromagnetic field can be quantified. Each time a quantum is emitted the energy of the electron makes a small discontinuous jump. The discontinuous change in energy from the quantum emission perturbs the electron trajectory. The cumulative effect of many such perturbations leads to a "noise" in the energy oscillation, which contributes on average to increase the standard deviation of the electron energy distribution, the energy spread. To evaluate the energy spread one may consider that the electrons in the ring emit randomly and the number of photons emitted by electrons is a value distributed with a Poisson distribution. The average relative energy spread, also called the natural relative energy spread, $\sigma_{\epsilon,0}$, taking into account only the 'noise' from the quantum emission, is given by the mean of the number of quanta emitted in one energy damping time τ_s [4], which is:

$$\sigma_{\epsilon,0} \approx \sqrt{E_0 u_c}, \tag{2.5}$$

with u_c the critical photon energy. It is defined as the energy at which the radiated power in a bending magnet is divided in two equal parts:

$$u_c = \frac{3}{4\pi}\frac{h\,c\,\gamma^3}{\rho_0}. \tag{2.6}$$

Here γ is the Lorentz factor of the electrons. The energy spread is approximately the geometric mean between the nominal energy and the critical photon energy.
A more accurate expression, taking into account the geometrical properties of the guiding magnetic field, can be obtained using the following formula [4]:

$$\sigma^2_{\epsilon,0} = \frac{C_q < G^3 > \gamma^2}{J_\epsilon < G^2 >}. \tag{2.7}$$

$C_q = \dfrac{55}{32\sqrt{3}}\dfrac{\hbar}{m_e c} \approx 8.84\,10^{-13}[m]$ is a quantum constant. This expression is more difficult to evaluate since it requires to perform the integrations:

$$< G^n >= \oint G\,(s)^n \frac{ds}{L}, \tag{2.8}$$

where $G\,(s) = 1/R\,(s)$ is called the curvature function, R being the radius of the trajectory at the coordinate s, and is defined by the guiding magnetic field of the lattice along the orbit path; the energy partition number $J_\epsilon = 2 + D$, where D is a small number compared to 1 and is defined also by the lattice.
For the Super ACO lattice for example the energy spread is given by the approximated expression:

$$\sigma_{\epsilon,0} = \frac{C_q \gamma^2}{\rho_0 + \alpha_c\, R}, \tag{2.9}$$

with R the average radius of the ring.
The energy spread of Super ACO and ELETTRA storage rings are given in table (2.1).

2.2.2 Longitudinal synchrotron motion

Previously we have seen that the electron energy oscillates due to synchrotron radiation and the energy recovery from the RF cavity. The energy oscillation is described by a differential equation, which will be given below.
The synchronous electron has a constant phase with respect to the RF field and receives an energy $U(t)$ equal to the energy loss in one turn U_0:

$$U_0 = e\hat{V}_{RF}\, sin\,(\varphi_s)\,, \tag{2.10}$$

where φ_s is the synchronous phase, and $\hat{V_{RF}}$ is the RF cavity voltage. The energy variation during one turn is:

$$\Delta\epsilon = e\hat{V}_{RF} sin\,(2\pi\nu_{RF}\tau + \varphi_s) - U\,(\epsilon), \tag{2.11}$$

with ν_{RF} the RF field frequency, τ the relative position of the electron with respect to the synchronous electron, and $U(\epsilon)$ the energy loss of the particle in one turn. For small energy variation is it possible to linearize this expression as follows:

$$\Delta\epsilon \approx e\hat{V}_{RF}\sin(\varphi_s) + e\hat{V}_{RF}2\pi\nu_{RF}\,\cos(\varphi_s)\,\tau - \left(U_0 + \epsilon\frac{dU}{dE}\right). \tag{2.12}$$

This expression can be simplified and written as a differential equation:

$$\frac{d\epsilon}{dt} = \frac{2\pi e\hat{V}_{RF}\cos(\varphi_s)}{T_0}\tau - \frac{1}{T_0}\frac{dU}{dE}\epsilon. \tag{2.13}$$

This equation can be coupled with a differential equation for the electron position which is derived from equation 2.3

$$\frac{d\tau}{dt} = -\frac{\alpha_c}{E_0}\epsilon. \tag{2.14}$$

The coupled equations can be simplified by differentiating the equation (2.14) and replacing the right hand side of equation 2.13:

$$\frac{d^2\tau}{dt^2} - \frac{1}{T_0}\frac{dU}{dE}\frac{d\tau}{dt} + \frac{eV\,2\pi\nu_{RF}\,\cos(\varphi_s)\,\alpha_c}{E_0\,T_0}\,\tau = 0. \tag{2.15}$$

This equation is a second-order differential equation, of which the solution is a damped oscillating function:

$$\tau\,(t) = Ae^{-2\alpha_s t}\cos(\Omega_s\,t + \varphi), \tag{2.16}$$

where $\Omega_s^2 = \dfrac{eV\,2\pi\nu_{RF}\,\cos(\varphi_s)\,\alpha_c}{E_0\,T_0}$ is the square of the radial synchrotron frequency, and $\alpha_s = \dfrac{1}{2T_0}\dfrac{dU}{dE}$. The synchrotron damping time is $\tau_s = \dfrac{1}{\alpha_s} \approx \dfrac{E_0 T_0}{U_0}$.
The electrons oscillate incoherently in position and energy around the synchronous electron with the oscillation frequency $\nu_s = \dfrac{\Omega_s}{2\pi}$. Their oscillations are damped with the characteristic time τ_s, and excited by the quantum emission. The electrons are not static in the bunch, and the electron bunch is characterized by a Gaussian distribution

in position and momentum given by the average amplitude oscillations. The standard deviation of the distribution is the r.m.s bunch length and is derived from equation 2.3 [4]:

$$\sigma_{\tau,0} = \frac{\alpha_c}{\Omega_s}\,\sigma_{\epsilon,0}\,, \tag{2.17}$$

where $\sigma_{\tau,0}$ accounts for the natural bunch length (σ_τ being the bunch length), and $\sigma_{\epsilon,0}$ for the natural relative energy spread (σ_ϵ being the relative energy spread).
The RF system is also characterized by its energy acceptance, ϵ_{RF}, which is defined as the maximum energy deviation that an electron can have without being lost. For an RF system consisting of only one RF cavity, an analytical expression of the energy acceptance can be derived from relation 2.11 [4]:

$$\epsilon_{RF} = \sqrt{\frac{2\,U_0\,E_0}{\pi\alpha_c k_h}\left(\sqrt{q^2-1} - \arccos\left(\frac{1}{q}\right)\right)}, \tag{2.18}$$

with $k_h = \nu_{RF}T_0$, the ratio between the RF frequency and the electron frequency revolution in the ring, and with q defined as $q = \dfrac{e\,V_{RF}}{U_0}$.

2.2.3 Transverse betatron motion

The movement of the electrons in the transverse plane is essentially due to the magnetic focussing from the quadrupole and dipole magnets of the lattice. The dispersion function, $\eta_x\,(s)$, describes the radial difference x between an electron of relative energy ϵ and the synchronous electron:

$$x = \eta_x\,(s)\,\frac{\epsilon}{E_0}. \tag{2.19}$$

The equations governing the transverse motion are [4]:

$$\begin{aligned} x" + K_x x &= \frac{1}{\rho_0\,(s)}\frac{\epsilon}{E_0} \\ y" + K_y y &= 0. \end{aligned} \tag{2.20}$$

The homogeneous equation describes the betatron motion in the transverse plane. The functions K_i $(i = x, y)$ are periodic functions depending on the magnetic focusing properties of the lattice. The homogeneous solutions of equation 2.20 are the typical pseudo-harmonic oscillator solutions given by:

$$\begin{aligned} x(s) &= \sqrt{\epsilon_x\beta_x}\cos(\phi_x(s) + \phi_{0x}) \\ y(s) &= \sqrt{\epsilon_y\beta_y}\cos(\phi_y(s) + \phi_{0y}). \end{aligned} \tag{2.21}$$

The quantity ϵ_i $(i = x, y)$ is a constant and is called the emittance. Its meaning will be given later. The functions β_i are the betatron functions, they are uniquely defined by the focusing properties of the magnetic lattice. The betatron phase $\phi_i(s)$ is defined by the following relation [4]:

$$\phi_i(s) = \int_0^s \frac{ds'}{\beta_i(s')}, \tag{2.22}$$

and ϕ_{0i} is the initial betatron phase.
The motion of the particles in phase space (i, i') is bounded by an ellipse, of which the area is the transverse emittance of the beam. The transverse emittance can be calculated with the maximum transverse deviation $(x_{max}(s), y_{max}(s))$ multiplied by the maximum divergence $(x'_{max}(s) = \frac{dx}{ds}|_{max}$, $y'_{max}(s) = \frac{dy}{ds}|_{max})$,

$$\epsilon_i = i_{max} i'_{max} \,. \tag{2.23}$$

The total transverse emittance, defined as $\epsilon_{tot} = \sqrt{\epsilon_x^2 + \epsilon_y^2}$, is a fundamental parameter for a storage ring, which characterizes the transverse quality of the electron beam and as a consequence the quality of the synchrotron radiation source. The emittance is also an important parameter, especially for short wavelength operation.
As for the longitudinal motion, the transverse motion of the electrons in the ring is an oscillating motion around the synchronous electron. The standard deviation of the oscillation amplitude distribution represents the beam transverse size. It is given by the following relation, considering that the focussing effect is not correlated with the synchrotron radiation effect so that the two effects contribute quadratically to the beam transverse size:

$$\begin{aligned} \sigma_x &= \sqrt{\epsilon_x \beta_x + \eta_x^2 \sigma_\epsilon^2} \\ \sigma_y &= \sqrt{\epsilon_y \beta_y}. \end{aligned} \tag{2.24}$$

2.2.4 Electron beam life time

Interactions of the electrons with each other or with the environment can contribute to deflect them out of their orbit so that they are lost for the bunch. As a result the lifetime of the beam is limited. Mainly three fundamental interactions may contribute to the beam lifetime [5] and have to be considered:

- the scattering on the residual gas of the vacuum chamber: the electrons scatter on molecules of the residual gas in the vacuum chamber. The interactions between relativistic electrons and residual gas molecules consist of two main mechanisms: Rutherford scattering (elastic collision) and Bremsstrahlung scattering (inelastic collision). In storage rings, due to the high energy of electron, the main contribution to the lifetime is the elastic scattering. In order to lower the probability of this interaction, an ultra high vacuum (10^{-11} mbar) is necessary.

- quantum lifetime: quantum radiation can give a too large oscillation amplitude to the electrons so that they hit with the wall of the vacuum chamber. In particular, considering the electron phase space distribution as Gaussian, the far tail of the distribution will be truncated by the longitudinal and transverse acceptance of the storage ring. The quantum lifetime is expressed by:

$$\tau_{quantum} = \tau_s \, (2\xi)^{-1} \, e^{\xi}, \tag{2.25}$$

where $\xi = \dfrac{A^2}{2\sigma^2}$ and A is the transverse acceptance or the energy acceptance of the RF cavity, and σ is respectively the root mean square (r.m.s) transverse emit-

tance or the energy spread, for the transverse and longitudinal cases respectively. Generally, in electron storage rings the quantum lifetime is considered infinite.

- intra-beam scattering, the so-called Touschek effect [6]: Electrons scattering on each other in the bunch can induce a larger energy deviation than the energy acceptance of the RF system, causing the loss of the scattered electrons. The Touschek lifetime, considering a bunch of N_e electrons with the dimensions $\sigma_{x,z,s}$ at the energy E_0 is given by:

$$\tau_T = \frac{8\pi\sigma_x\sigma_z\sigma_s\gamma^2\epsilon_{RF}^3}{N_e c r_e^2 D(\zeta)} \tag{2.26}$$

with

$$\begin{aligned} D(\zeta) &= \sqrt{\zeta}\left(-\frac{3}{2}e^{-\zeta} + \frac{\zeta}{2}\int_\zeta^\infty du\frac{\ln(u)e^{-u}}{u} + \frac{1}{2}(3\zeta - \zeta\ln\zeta 2)\int_\zeta^\infty du\frac{e^{-u}}{u}\right) \\ \zeta &= \left(\frac{\epsilon_{RF}\beta_x}{\gamma\sigma_x}\right)^2, \end{aligned} \tag{2.27}$$

where D is a universal function, and r_e the classical radius of the electron. The Touschek lifetime is an important factor for electron storage rings because it is inversely proportional to the electron density. Therefore it is a limiting factor to the current that can be stored in the ring.

In summary for electron storage rings the Touschek lifetime is the main contribution to the beam lifetime. It is dependent on the square of the electron energy, so that storage rings operating at ultra-relativistic energy (GeV) have nowadays a beam lifetime of few tens of hours. An FEL interacting with the beam induces energy spreading and bunch lengthening, so that it increases also the beam lifetime, as will be explained later.

2.2.5 Static electrons distributions and wake fields

The general behavior of the electrons stored in a ring has been described in the previous subsections. We have seen that the electrons oscillate in the transverse and longitudinal planes, the oscillations are damped but the quantum nature of the synchrotron radiation leads to an excitation of the oscillations. The standard deviations of the transverse and longitudinal oscillation distributions give the dimensions of the bunches circulating in the ring. The distributions are Gaussian since we considered statistical effects due to the quantum energy fluctuations. An important effect, which perturbs the electron dynamics, is the interaction of electrons with the electromagnetic field generated by the moving relativistic electrons and reflected by the wall of the vacuum chamber. This field can interact with the same electron bunch that has generated it or with the next one. This electromagnetic field is called the wakefield and is the source of instabilities to the electron beam. The instabilities can be damped and the beam will be perturbed, or it is not damped and the beam will be lost. A damageable instability to the beam, in the longitudinal plane, is the microwave instability, which is due to the wakefield in the micrometer wavelength range. The effect of the microwave

instability will be discussed in chapter 3. When the instability is damped, the perturbation due to the wakefield modifies the electron bunch characteristics. The wakefield introduces a distortion of the static Gaussian distribution in the longitudinal plane, which results in an increase of the bunch length. The bunch lengthening due to the distortion is given by the solutions of the Haissinski equation [7], which describes the static electron bunch longitudinal distribution (chapter 3).
The bunch lengthening for example contributes to reduce the level of the laser gain, and then to change the laser dynamics.

Table 2.1: *ELETTRA and Super-ACO parameters for FEL operation.*

		ELETTRA	Super ACO
Nominal energy (GeV)	E_0	1	0.8
Number of electron bunches		4	2
Period (ring) (ns)	T_0	864	240
Magnetic radius of curvature (m)	ρ_0	5.56	1.5
Momentum compaction factor	α_c	0.00161	0.0148
Energy radiated in one turn [keV]	U_0	16	21
Critical energy [eV]	u_c	400	670
Synchrotron damping time (ms)	τ_s	65	8.5
Natural r.m.s energy spread (10^{-4})	$\sigma_{\epsilon,0}$	3.97	5.45
Natural r.m.s bunch length (ps)	σ_τ	6.28	86
Synchrotron frequency (kHz)	f_s	16.1	14.5
Period (optical cavity) (ns)	T_c	216	120
Small signal gain	g_0	0.35	0.025
Cavity loss	η	0.06	0.005-0.01
Undulator period number	N_u	20	10
Dispersive section number	N_d	80	100
Undulator strength (max.)	K	5.85	5.75
Laser wavelength (nm)	λ_{Las}	189	300

2.3 The FEL basics

In this section the principle of the free electron laser mechanism is described. First, by investigating the electron trajectory in an undulator, the spontaneous emission of the laser, which is the synchrotron radiation, is calculated. In addition, it is possible to calculate the energy exchange between one electron and a propagating plane wave in the undulator, leading to the evaluation of the amplification of the laser. Finally after evaluating the gain of the laser, and the effect of the laser on the electron during the interaction, we are able to build up a simple analytical model of the free electron laser dynamics, the FEL pendulum equation.

2.3.1 Electron trajectory in an undulator

An undulator is a device in which a permanent periodic magnetic field is created. Two kinds of undulators can be considered: the helical and the planar undulator. An

electron traversing a helical undulator undergoes an helical path, and in a planar undulator, the movement is a sinusoidal motion in one plane.
The magnetic field in a planar undulator, considering a perfect sinusoidal in the interaction region, is expressed as:

$$\vec{B} = B_u \cos(k_u z)\,\hat{y}, \tag{2.28}$$

with $\lambda_u = \frac{2\pi}{k_u}$ the undulator period. The coordinate system here is the cartesian coordinate frame $(\hat{x}, \hat{y}, \hat{z})$, describing the horizontal, vertical, and longitudinal axis respectively (the longitudinal axis being the undulator axis). The Lorentz force exerted on the electron leads to the motion:

$$\frac{d\gamma m_e \vec{\beta}}{dt} = e\vec{\beta} \times \vec{B}, \tag{2.29}$$

with $\vec{\beta} = \frac{\vec{v_e}}{c}$ the speed of the electron divided by the speed of light.
In the approximation of an ultra-relativistic electron, $\beta_z \approx 1$, so that one can write:

$$\frac{d\vec{\beta}}{dt} = \begin{pmatrix} \frac{eB_u}{m_e\gamma}\beta_z \cos(k_u ct) \\ 0 \\ -\frac{eB_u}{m_e\gamma}\beta_x \cos(k_u ct) \end{pmatrix}. \tag{2.30}$$

This equation is immediately integrable, assuming $\beta_z \approx 1$ and $\beta_x \ll 1$, and $\beta_x^2 + \beta_z^2 = 1 - \frac{1}{\gamma^2}$:

$$\vec{\beta} = \begin{pmatrix} \frac{K}{\gamma}\sin(k_u ct) \\ 0 \\ \sqrt{1 - \frac{1}{\gamma^2} - \frac{K^2}{\gamma^2}\sin^2(k_u ct)} \end{pmatrix}, \tag{2.31}$$

with $K = \dfrac{e\lambda_u B_u}{2\pi m_e c}$ defined as the undulator strength parameter. Equation 2.31 can be integrated to find the motion of an electron traversing a planar undulator[†]:

$$\vec{X} = \begin{pmatrix} \frac{K\lambda_u}{2\pi\gamma}\cos(k_u ct) \\ 0 \\ \left(1 - \frac{1}{2\gamma^2} - \frac{K^2}{4\gamma^2}\right)ct + \frac{K^2\lambda_u}{16\pi\gamma^2}\sin(2k_u ct) \end{pmatrix}. \tag{2.32}$$

The motion is in the horizontal plane with a sinusoidal motion with the radial frequency $\omega = \dfrac{2\pi c}{\lambda_u}$ in the horizontal direction and 2ω in the longitudinal direction.
In the case of the helical undulator the motion is the same in the two perpendicular

[†]the integration of β_z can be done by considering the series development of $\sqrt{1-x}$ around x=0

planes. One finds the trajectory:

$$\vec{X} = \begin{pmatrix} \frac{K\lambda_u}{2\pi\gamma}\cos\left(k_u ct\right) \\ \frac{K\lambda_u}{2\pi\gamma}\sin\left(k_u ct\right) \\ \left(1 - \frac{1}{2\gamma^2} - \frac{K^2}{2\gamma^2}\right) ct \end{pmatrix}. \tag{2.33}$$

The trajectory of electrons and their velocities during the traversing of the undulator will be used in the coming subsection to calculate the synchrotron radiation in an undulator.

2.3.2 Spontaneous emission

When traversing an undulator, relativistic electrons radiate. This radiation, called synchrotron radiation, has the same nature as the Bremsstrahlung [8]. This radiation is the spontaneous emission of the free electron laser.
The wavelength of the radiation emitted can be calculated by means of the Doppler effect: the electron can be seen in the rest frame as an oscillating dipole in the transverse plane and moving in the longitudinal direction (parallel to the undulator axis) at the average speed $< \beta_z >$. The undulator magnetic field can be seen in the electron rest frame as a virtual electromagnetic field with the wavelength $\frac{\lambda_u < \beta_z >}{\gamma}$. In the laboratory frame, for an observation point at an angle θ from the undulator axis the emitted wavelength is:

$$\lambda_r = \frac{\lambda_u}{2\gamma^2}\left(1 + \frac{K^2}{2} + \gamma^2\theta^2\right), \tag{2.34}$$

where θ is the angle an observer (of the emitted light from the particles) has with the propagation axis. The radiation for highly relativistic electrons is confined in a narrow cone with angular aperture $\frac{1}{\gamma}$. The spectral power density per unit solid angle can be calculated from the Liénard-Wiechert [8] equation using the following expression:

$$I_{sp} = \frac{d^2\, I}{d\omega d\Omega} = \frac{e^2\omega^2}{4\pi^2 c}\left|\int_{-\infty}^{\infty} dt\, \hat{n} \times \left(\hat{n} \times \vec{\beta}\right) e^{i\omega\left(t - \frac{\hat{n}.\vec{r}(t)}{c}\right)}\right|^2 \tag{2.35}$$

In the case of a planar undulator with N_u magnetic periods, a period length λ_u and a strength K, and using the velocity expression 2.31 and the retarded time $t - \frac{\hat{n}.\vec{r}(t)}{c} = t - \frac{z(t)}{c}$ one finds the expression at infinity in the longitudinal direction [9]-[10]:

$$I_{sp.}\left(\lambda\right) = \frac{d^2\, I}{d\omega d\Omega}|_{\theta=0} = \frac{e^2}{4\pi^2 c}\left(\frac{K N_u \lambda_u}{\gamma}\right)^2 \sum_{p=0}^{\infty} \frac{A_{2p+1}^2}{\lambda^2} sinc^2\left(\delta_{2p+1}\right), \tag{2.36}$$

where

$$\begin{aligned} A_n &= J_{\frac{n+1}{2}}(\xi_n) - J_{\frac{n-1}{2}}(\xi_n) \\ \xi_n &= \frac{nK^2}{4+2K^2} \\ \delta_n &= \pi N_u \left(n - \frac{\lambda_r}{\lambda}\right) \end{aligned} \tag{2.37}$$

and the function $sinc(x) = \dfrac{\sin(x)}{x}$ is the sinus cardinal function.
In a planar undulator the power spectrum on axis of the spontaneous emission is composed of an infinite sum of sinus cardinal squared centered at the odd harmonics of the resonant wavelength λ_r (defined in (1.1)). The harmonic content in the spectrum depends on the undulator strength. For small values, $K \leq 1$ the spectrum is essentially composed of the fundamental walvelength. The radiation is coherent. For $K \geq 1$ the spectrum is composed of the first odd harmonic, with a higher harmonic content with higher values of K. The radiation is still coherent. In the case of $K \gg 1$ there are many more harmonics in the spectrum and the undulator is called a wiggler. The radiation is no longer coherent.
The polarization of the emitted radiation is essentially given by the undulator: linear for a planar undulator and circular for a helical one.

2.3.3 Amplified emission

The amplification is the main process of the laser, and the gain is the most important parameter of the system. The interaction, taking place in the undulator between the light and the electrons traversing the undulator, leads to an energy exchange to the detriment of the kinetic energy of the electrons. The electron energy is modulated during the interaction, and the energy loss or gain provides micro-bunching of the electrons at the resonant wavelength. When the electrons are micro-bunched, they emit coherently at the resonant wavelength.
The energy exchange, studied by Madey in 1971 [11] can be calculated using the approximations that the electromagnetic field is a plane wave with a small amplitude and the gain is small. The electron trajectories depend on the electromagnetic field intensity along the undulator. The expression of the energy exchange is:

$$\delta\gamma = -e \int_{L_{int}} dt E_w(t)\, v_\perp(t) \ , \tag{2.38}$$

with E_w the electric field amplitude, $v_\perp = \beta_\perp c$ the speed of the electron in the perpendicular plane to the wave propagation. It is not possible to express analytically the transverse speed of electrons $v_\perp$ as function of time along the interaction length L_{int}, but it can be done using a perturbation approach. The coupling between the wave and the electrons has to be considered. The wave perturbs the transverse trajectory of the electrons. One can make a development in a power series of the plane wave amplitude E_w of the speed of the electrons:

$$v_\perp = v_{\perp,0} + v_{\perp,1}(E_w) + v_{\perp,2}(E_w^2) + ... \tag{2.39}$$

and one can consider the energy exchange between one electron and the plane wave, at each order of the series expansion. In first order, taking the expression of the horizontal speed of the electrons traversing the planar undulator calculated in (2.30), the energy exchange is

$$\delta\gamma_1 = -\frac{e\,K\,E_w}{\gamma}\int_{L_{int}} dt \sin(k_u ct)\sin(\omega t - kc < \beta_z > t + \Phi), \tag{2.40}$$

with $< \beta_z >$ the average longitudinal speed of the electron and Φ its relative phase with respect to the plane wave. The plane wave has a frequency $\nu = \frac{\omega}{2\pi}$ and k is its wave number. The integral above is non-zero only for the condition $\omega = (k_u + k)\,c$ which corresponds to the resonance condition (2.34). An electron will gain or loose energy depending on its phase Φ. Considering the electrons being distributed randomly, the average energy exchange in first order is zero: $< \delta\gamma_1 >_e \equiv 0$.
The energy "shift", $< \delta\gamma_1 >_e$, may be zero, the energy "spread" in first order, $< \delta\gamma_1^2 >_e$, is non-zero, as enounced by Madey in a first theorem [11], and it can be evaluated as:

$$< (\delta\gamma_1)^2 >_e = \frac{2\pi^2}{m_e^2 c\omega^2} E_w^2 I_{sp.}. \tag{2.41}$$

The average energy exchange between a plane wave and an electron bunch in an undulator, can be expressed as the second Madey theorem [11], which is given by:

$$< \delta\gamma_2 >_e = \frac{\partial}{2\,\partial\gamma} < (\delta\gamma_1)^2 > \equiv < \delta\gamma >_e , \tag{2.42}$$

where $<>_e$ means the average over all the electrons. The energy exchange, at the second order $< \delta\gamma_2 >_e$, between a plane wave and an electron bunch in an undulator is proportional to the derivative of the spontaneous emission. This is valid only in the small signal gain regime. In the high gain regime ($G \gg 0.3$) higher order terms must be taken into account. In the case of an undulator, the small signal gain, given by $\frac{\Delta(E_w^2)}{E_w^2} = \frac{<\delta\gamma>_e}{E_w^2}$, can be expressed as [12]:

$$G(\delta_1) = \frac{4 r_e \pi^{\frac{5}{4}} N_e}{\sigma_x\sigma_y\sigma_z\gamma^3}\lambda_u^2 N_u^3 K^2 F_J(\xi)\, F_f \frac{\partial}{\partial\delta_1}\left(sinc(\delta_1)^2\right), \tag{2.43}$$

where N_e is the number of electrons, δ_1 is defined in 2.37

$$F_J(\xi) = \begin{cases} 1 & \text{helical undulator,} \\ (J_1(\xi) - J_0(\xi))^2 & \text{planar undulator.} \end{cases} \tag{2.44}$$

and $J_n(\xi)$ is the Bessel function of the order n with the argument $\xi = \dfrac{K^2}{4 + 2K^2}$. The filling factor, F_f, takes into account the transverse overlapping between the laser pulse and the electrons as

$$F_f = \begin{cases} 1 & \text{if } \Sigma_e > \Sigma_L\ , \\ \dfrac{\Sigma_e}{\Sigma_L} & \text{otherwise.} \end{cases} \tag{2.45}$$

Here Σ_e and Σ_L are respectively the electron beam and laser transverse sections. One notes that the gain is proportional to the square of the undulator length $L_u = N_u\lambda_u$,

to the electron bunch density, and inversely proportional to the cube of the electron energy[‡]. The laser wavelength positions itself to maximum gain. It corresponds to the wavelength given by the spectral detuning $\delta_1 \approx 1.303$ which maximizes $\frac{\partial}{\partial \delta_1}\left(sinc(\delta_1)^2\right)$.

2.3.4 The optical klystron

The optical klystron is a combination of two undulators separated by a drift or a dispersive section [13]. The electron energy is modulated in the first undulator, which is called the modulator. The dispersive section transforms the energy modulation in spatial modulation at the undulator resonant wavelength. Therefore the dispersive section enhances the micro-bunching of the electrons. The micro-bunched electrons radiate coherently in the second undulator, which is called the radiator. The purpose of the device is to enhance the gain compared with an undulator of the same length. This is particulary interesting in storage rings where the straight sections of the free electron laser are short (limiting the number of periods and hence the small signal gain). However, optical klystrons are still preferred in SRFELs for the gain they provide even for long straight sections, like for example 12 m for the proposed FEL for SOLEIL (France), and 25 m for the proposed optical klystron of the future DUKE FEL (USA). The free electron lasers at Super ACO and at Elettra have respectively a planar and helical undulator in their optical cavity. The same approach as in the previous section can be done to calculate the spontaneous emission of the laser and then to calculate the gain. The integral (2.35) can be split in 3 parts to evaluate the power spectrum

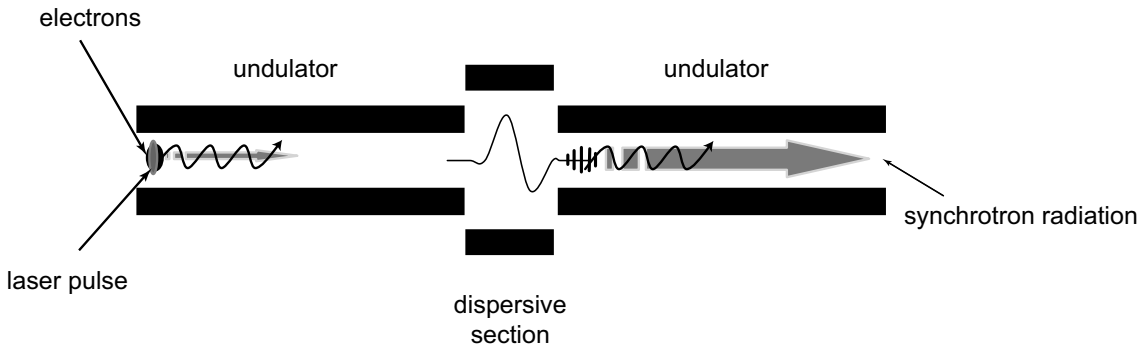

Figure 2.4: *Optical klystron scheme: in the first undulator, called the 'modulator', the electron energy is modulated. The dispersive section transforms the modulated energy in spatial modulation, enhancing the micro-bunching of the electrons at the resonant wavelength. In the second undulator, called the 'radiator', the electrons micro-bunched radiate coherently.*

radiated. The first integral is the contribution from the first undulator, the second one represents the drift-space or dispersive section and is negligible: the dispersive section is much shorter than the undulator sections and the electron motion is out of the resonance condition. The third integral is the contribution from the second undulator.

[‡]the Lorentz factor is evaluated from the energy as: $\gamma = 1 + \frac{E_0}{m_e c^2} \simeq 1 + \frac{E_0[MeV]}{0.511}$

As the contribution of the dispersive section is small compared to the one from the undulators, the power spectrum in an optical klystron can be written as [14]:

$$I_{sp.OK} = 2\, I_{sp.Und}\,(1 + \cos(\alpha_d)), \tag{2.46}$$

where $I_{sp.Und}$ is the spontaneous emission in the first undulator.
The quantity $\alpha_d = 2\pi\,(N_u + N_d)\,\dfrac{\lambda_r \gamma_r^2}{\lambda \gamma^2}$ is the phase difference between the waves radiated in the two undulators, induced by the dispersive section. Here γ_r is the resonant energy, and N_d is a dimensionless parameter representing the advance of an observed photon at the wavelength λ, in terms of number of optical periods, with respect to an electron with the energy γ. The term $N_u + N_d$ gives the interference order of the power spectrum. By considering a distribution of electrons and taking the average power spectrum radiated one obtains:

$$I_{sp.OK} = 2 I_{sp.Und}\,(1 + f\cos(\alpha_m))\,, \tag{2.47}$$

where α_m is the average phase given by the energy distribution. The factor f is called the modulation factor, which is mainly dependent on the energy spread (σ_ϵ) of the electron bunch and is given by

$$f \cong f_0 e^{-8\pi^2 (N_u + N_d)^2 \sigma_\epsilon^2}, \tag{2.48}$$

with f_0 a constant near 1 taking into account the effects of the finite transverse dimensions. Figure (2.5) presents a spectrum from the optical klystron. The modulation rate in the spectrum can be measured as

$$f = \frac{I_{max} - I_{min}}{I_{max} + I_{min}}, \tag{2.49}$$

where I_{max} and I_{min} are the maxima and minima of the spectrum fringes.
The power spectrum from an optical klystron can be used to measure the beam energy spread. By changing the magnetic field of the dispersive section, one changes N_d, so that a logarithmic plot of the f values from the different spectra as function of $(N_u + N_d)^2$ gives f_0 and the energy spread. The power spectrum can be used to measure the beam energy spread.

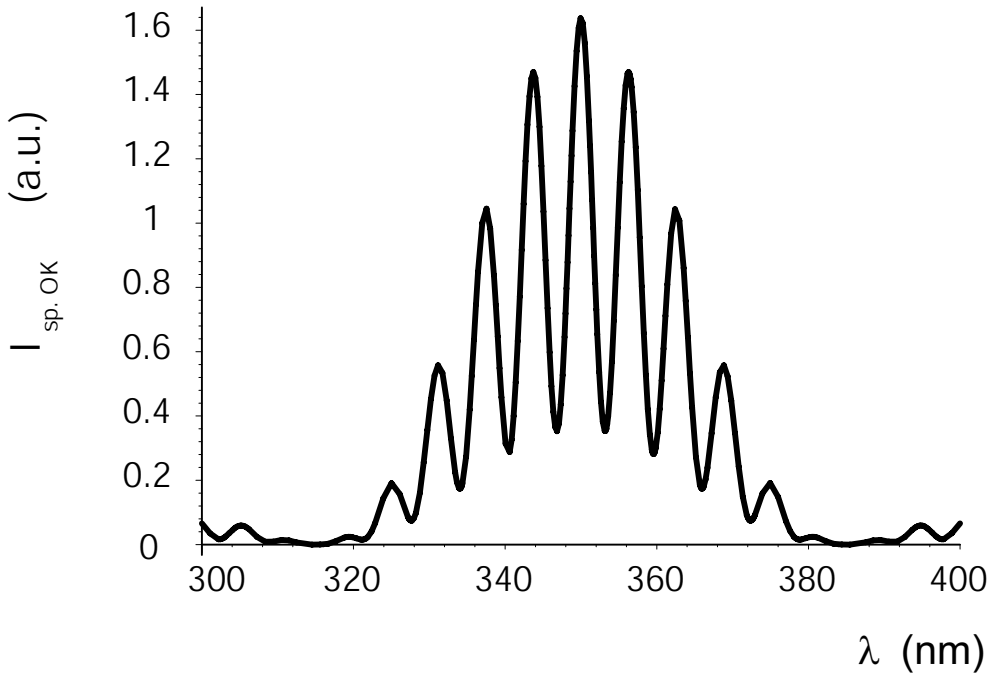

Figure 2.5: *Power spectrum of the spontaneous emission from the optical klystron at Super ACO. The resonance wavelength is* $\lambda_r = 350$ *nm, a fit of the spectrum gives* $f \approx 0.64$ *and* $N_d \approx 100$.

The small signal gain can be calculated as before, using the Madey theorems, to find the expression [15]:

$$G = \frac{4 r_e \pi^{\frac{5}{4}} N_e}{\sigma_x \sigma_y \sigma_z} \left(K\, N_u\, \lambda_u\right)^2 F_J\left(\frac{N_u + N_d)\, f}{\gamma^3} F_f sinc(\delta_1) \sin(2\pi(N_u + N_d)\frac{\lambda_r}{\lambda}\right), \qquad (2.50)$$

where σ_i $(i = x, y, z)$ the r.m.s dimensions[§] of the electron bunch (given in m). Using the expression (2.50) and the figure (2.6) one observes that the laser may grow on one of the fringes from both sides of the resonant wavelength. It is also observed at Super ACO and at ELETTRA that the laser may develop on several wavelengths, jumping from one fringe to another. The laser grows on the wavelength with the higher gain and in general it is nearer to λ_r than in the case of the undulator.
The enhancement of the gain is understood by the enhancement of the maximum value of the derivative of the spontaneous emission, due to the interference fringes.

[§]the bunch length may be also given in s, then we use the notation σ_τ

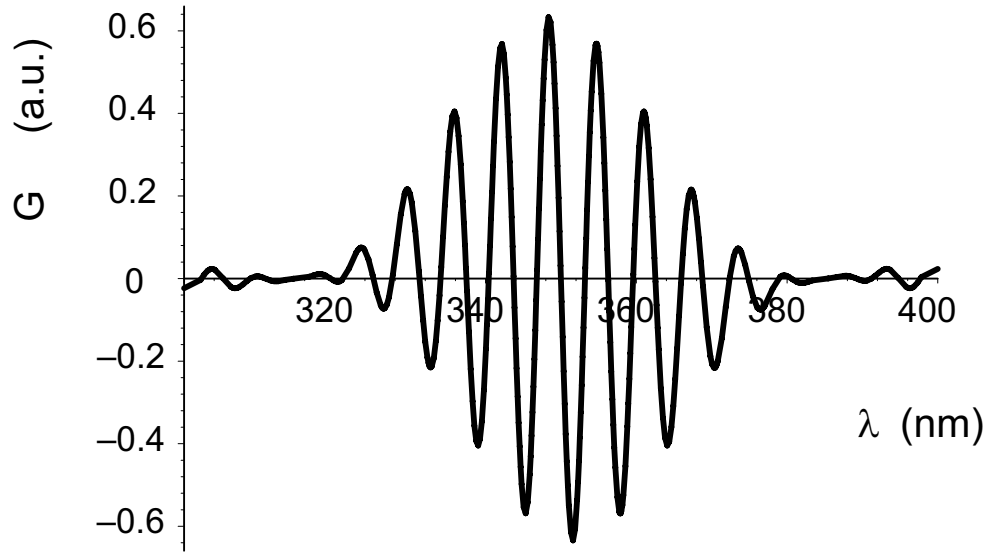

Figure 2.6: *Gain with an optical klystron using expression 2.50 with the parameters f, N_u and N_d of Super ACO used in figure (2.5).*

2.3.5 Laser - electron dynamics

The dynamics of the system laser - electron bunch may be described at first with a simple 0-dimensional model. The coupled system renders account of the dynamics with two quantities: the laser intra-cavity power and the beam energy spread. The evolution of the system is given by the following differential equations:

$$\begin{aligned} \frac{\partial}{\partial t} I &= \frac{1}{T_0} I \left(\frac{g_0 e^{-\mu_\epsilon^2 \left(1+\sigma^2\right)}}{\sqrt{(1+\sigma^2)}} - \eta \right) \\ \frac{\partial}{\partial t} \sigma^2 &= -\frac{2}{\tau_s} \left(\sigma^2 - I\right), \end{aligned} \tag{2.51}$$

where the dimensionless intra-cavity power is given by $I = I_{Las}/I_{sat}$, I_{Las} being the laser intra-cavity peak power, and $I_{sat} = 690\,(\frac{\gamma}{N_u})^4(\frac{1}{K\lambda_u F_J\,(\xi)})^2$ [MW/cm^2] is the quantity defined by Colson [16]. This quantity is defined for an undulator, and can be used as such taking the number of periods of an equivalent undulator. The relative energy spread is given by $\sigma_\epsilon = \sigma_{\epsilon,0}\sqrt{1+\sigma^2}$.

The gain can be written using the expression (2.50) as $G \equiv g_0 \dfrac{e^{-\mu_\epsilon^2\left(1+\sigma^2\right)}}{\sqrt{1+\sigma^2}}$, with g_0 the small signal gain, which can be evaluated with expression (2.50) using the electron bunch characteristics at the start up of the laser. The quantities T_0 and τ_s are respectively the period of the laser pulse in the cavity and the synchrotron damping time (see expression (2.16))

The quantity $\mu_\epsilon = \begin{cases} \frac{2}{\sqrt{2}}\pi N_u \sigma_{\epsilon_0} & \text{(undulator)} \\ \frac{4}{\sqrt{2}}\pi (N_u + N_d)\,\sigma_{\epsilon_0} & \text{(optical klystron)} \end{cases}$ accounts for the electron energy inhomogeneous broadening parameter. The total cavity loss is given by η. The quantities of the different parameters for Super ACO and for ELETTRA can be found

in table (2.1). A graph of the evolution of such a system is shown is figure (2.7).
This simple model illustrates the saturation of the laser [17], which comes from the fact that the gain decreases with the laser induced energy spread of the electron beam. The coupled equations are non-linear and a topological approach [18] can be used to analyze the behavior of the system. A plot of the phase space (I, σ^2), shown in figure (2.8), presents a singular point, which is a stable focal point (attractor). The system, starting from any positive point (σ^2 and I are physical quantities and are defined positive) will converge to this attractor. The system is then a stable system, and can be represented as a damped oscillator [19].

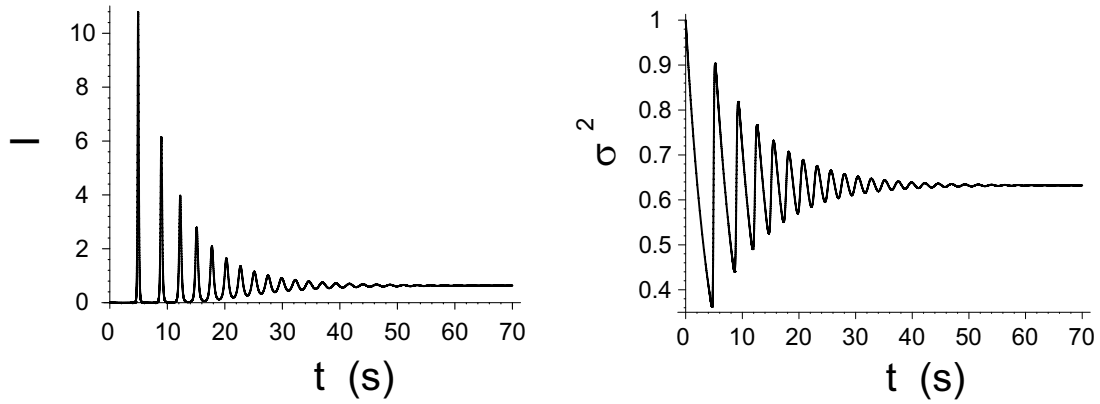

(a) (b)

Figure 2.7: *Intra-cavity laser power, I, and induced relative energy spread, σ, vs. time, calculated from the 0-D model given by the expression (2.51). Here the initial values are taken from the Super ACO case: $I(0) = 0.01$, $\sigma^2(0) = 1$, $g_0 = 2.1\%$, $\eta = 1\%$ and $\mu_\epsilon = 0.551$.*

The phase plane (I, σ^2) contains two singularities, the first one is (0,0), which corresponds to the system laser off, or a lower gain (g_0) than the cavity loss (η). The other point is given by:

$$I_{sing} = \quad \sigma^2_{sing} = \quad -1 + \left(\frac{g_0}{\eta} e^{-\frac{1}{2} W\left(2\frac{g_0^2}{\eta^2}\mu_\epsilon^2\right)} \right)^2 . \tag{2.52}$$

Using the properties of the function W, know as Lambert W function [20]-[21]-[22], one proves that the exponential term is positive, for all real $\mu > 0$, $g_0 > \eta > 0$ (so that (I_{sing},σ^2_{sing}) belongs to the first quadrant ($I > 0, \sigma^2 > 0$). In addition, a more detailed study shows that this singular point is always a focal point so that, once the initial conditions are fixed, the system converges at an infinite time to the focal point.
From this simple topological analysis, it is possible to give the order of magnitude of the laser power at saturation, and the induced energy spread. Taking Super ACO (see table (2.1)) as an example, one finds the dimensionless intensity at saturation: $I(\infty) \approx 1$, which corresponds to the intensity $I_{real} \approx 5$ MW on a waist area at 350 nm. The corresponding relative energy spread is $\sigma_\epsilon \approx 7.6\,10^{-4}$.

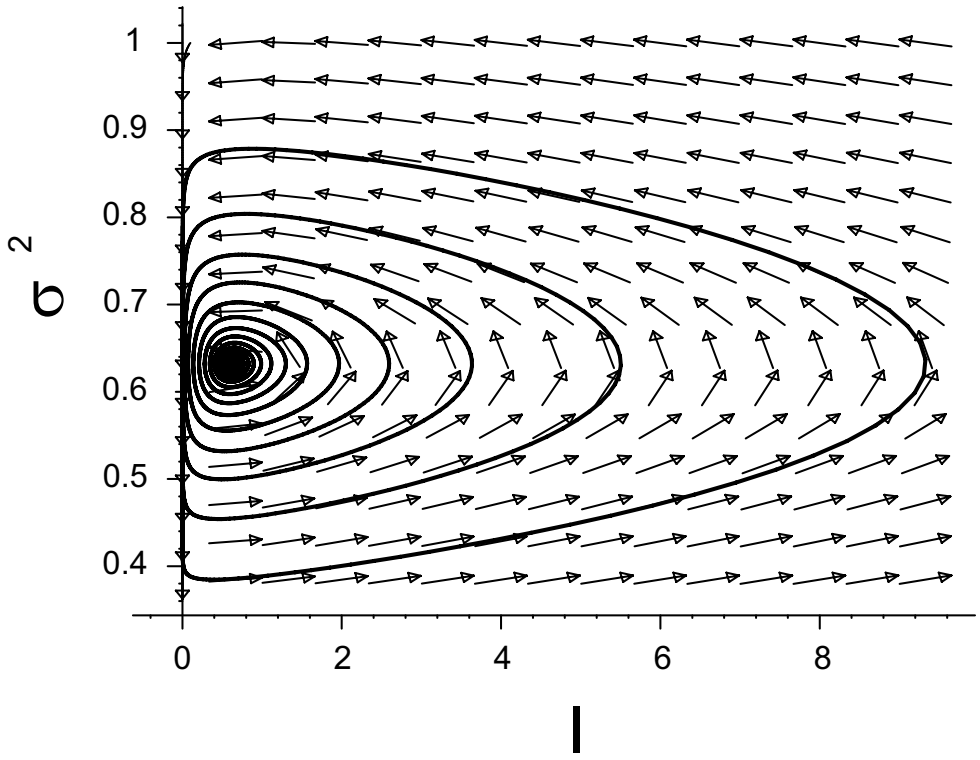

Figure 2.8: *Phase space plot (I, σ^2) showing the trajectory of the SRFEL system. The arrows represents the tangent to the vector ($\dot{I}$, $\dot{\sigma}^2$), and the constants are the same as in figure (2.7).*

2.4 CONCLUSION

In this chapter the basics of the storage ring free electron laser have been presented. The main features of the electron dynamics in a storage ring are described, neglecting the transverse motion and the instabilities which occur on the electron beam, by the dynamics of the electron bunch energy spread. The gain has been calculated with the Madey's theorem, under the small signal gain assumption, using the spontaneous emission (the power spectrum radiated in an undulator / optical klystron). From the expression of the gain, a 0-dimensional model has been presented, showing the saturation process in an SRFEL. The analytical study of the system gives the order of magnitude of the intra-cavity power as well as the laser induced energy spread.
In the next chapter, a more complex model of the SRFEL is presented. It includes the microwave instability effects on the electron beam, and on the SRFEL system. The model gives the laser pulse characteristics in the longitudinal plane (the propagation axis), pulse duration (consequently spectral width), power, etc. Moreover it shows the energy spreading, as well as the bunch lengthening. In addition, the model takes into account an important parameter of the system, the longitudinal detuning, defined as the delay per pass between the laser pulse and the electron bunch.

References

[1] D. A. G. Deacon, L. R. Elias, J. M. J. Madey, G. J. Ramian, H. A. Schwettman, and T. I. Smith. First operation of a free-electron laser. *Physical Review Letters*, 38:892, April 1977.

[2] M. Billardon, J. M. Ortega, P. Elleaume, C. Bazin, M. Bergher, M. Velghe, Y. Petroff, D. A. G. Deacon, K. E. Robinson, and J. M. J. Madey. First operation of a storage-ring free-electron laser. *Physical Review Letters*, 51:1652–1655, October 1983.

[3] E. Koch, G. V. Marr, D. E. Moncton, G. S. Brown, S. Ebashi, Koch M., and E. Rubenstein. *Handbook on synchrotron radiation*, volume 2. North-Holland, Amsterdam (the Netherlands), Koch, e edition, 1983.

[4] M. Sands. *The physics of electron storage ring, an introduction*, volume 121. SLAC report, November 1970.

[5] C. J. Bocchetta. *Lifetime and beam emission in storage ring*. CERN Accelerator School, April 1990.

[6] C. Bernardini, G. F. Corazza, G. di Giugno, G. Ghigo, J. Haissinski, P. Marin, R. Querzoli, and B. Touschek. Lifetime and Beam Size in a Storage Ring . *Physical Review Letters*, 10:407–409, May 1963.

[7] J. Haissinski. *Nuovo Cimento B*, 18:72, 1973.

[8] J. D. Jackson. *Classical electrodynamics*. Wiley & Son, 3^{rd} edition, 1998.

[9] P. Elleaume. *Free electron laser undulators, electron trajectories and spontaneous emission*, volume 6 of *Laser Handbook*, chapter 4, page 91. elsevier Science, North Holland, Colson, w.b. and Pelligrini, c. and Renieri, a. edition, 1990.

[10] G. Dattoli, Renieri A., and A. Torre. *Lectures on the free electron laser and related topics*. World Scientific, 1^{st} edition, 1993.

[11] J. M. J. Madey. Stimulated emission of bremmstrahlung in a periodinc magnetic field. *Jounal of Applied Physics*, 42(5):1906, 1971.

[12] G. Dattoli, A. Torre, L. Giannessi, and S. Depanfilis. *An introduction to the theory of free electron lasers* , volume 90-3 of *CAS*, chapter 3. CERN Accelerator School and Daresbury Laboratory, 1990.

[13] N. A. Vinokurov and A. N. Skrinsky. *Preprint 77-59*. Nuclear Physics Institute of Novossibirsk, 1977.

[14] P. Elleaume. The Optical klystron. *J. de Phys. (Paris)*, 44(C1):353, 1983.

[15] M. E. Couprie. *Laser à électron libres sur anneau de stockage*. PhD thesis, Université Paris Sud, Orsay (france), May 1989.

[16] W. B. Colson. *Free electron laser undulators, electron trajectories and spontaneous emission*, volume 6 of *Laser Handbook*, chapter 5, page 115. elsevier Science, North Holland, Colson, w.b. and Pelligrini, c. and Renieri, a. edition, 1990.

[17] M. Billardon, D. Garzella, and M. E. Couprie. Saturation mechanism for a storage-ring free-electron laser. *Physical Review Letters*, 69:2368–2371, October 1992.

[18] R. H. Enns. *Nonlinear physics with Maple for scientists and engineers*. Birkhaüser, R. H. Enns and G. C. Mc Guire edition, 2000.

[19] P. Elleaume. Macrotemporal structure of storage ring free electron lasers. *J. de Phys. (Paris)*, 45:997, 1984.

[20] R. M. Corless, G. H. Gonnet, D. E. G. Hare, and D. J. Jeffrey. Lambert's W Function in Maple. *Maple Technical Newsletter*, 9:12, 1993.

[21] R. M. Corless, G. H. Gonnet, D. E. G. Hare, D. J. Jeffrey, and D.E. Knuth. On the Lambert W Function. *Advances in Computational Mathematics*, 5:329, 1996.

[22] R. M. Corless, D. J. Jeffrey, and D.E. Knuth. A Sequence of Series for the Lambert W Function. In *Proceedings ISSAC '97, Maui*, page 197, 1997.

Chapter 3

Dynamics of the SRFEL: theoretical and numerical aspects

3.1 Electron beam dynamics

The evolution of the phase space distribution of the electron beam in a storage ring is fully described with a differential equation called the Fokker-Planck equation [1]. The solution of this equation is the phase-space electron bunch distribution vs. time. This equation can be coupled with a 3-dimensional differential equation for the free electron laser evolution to predict accurately the behavior of the coupled system relativistic electron bunch - laser pulse. Solving this differential equations system with sufficient accuracy require a large CPU time. Here we will try to simplify the problem by adopting an heuristic approach, which saves CPU time and brings to light the physical phenomena. To solve our problem we will first assume that when the laser starts, the bunch phase space distribution is stationary, and is described by the static solution of the Fokker-Planck equation. We assume then the phase-space distribution can be decoupled in position and energy distributions. This is an important assumption which leads to the fact that the shape of the longitudinal distribution does not depend on the energy distribution.
Relativistic electrons circulating in a ring emit an electric field, which is reflected by the vacuum chamber and called the wakefield. An electron bunch may interact with its own wakefield or the next coming bunch may interact with that wakefield. The Haissinski equation [2], given by the static solution of the Fokker-Planck equation, describes the bunch static longitudinal distribution taking into account the effect of the wakefield. In the first subsection, we solve the Haissinski equation for specific wakefields. This gives an overview of the longitudinal bunch distribution when the laser starts.
The wakefield is also a source of instabilities for the electrons. The most common longitudinal instability in storage rings is the microwave instability (the instability due to the wakefield in the micrometer wavelength range). In a second subsection we will present and discuss a simple model of the beam dynamics including the microwave instability effects.
Finally in the second part of the chapter we will present a 1-dimensional differential equation, derived from the propagation equations, accounting for the laser electric field evolution. Coupled with the two differential equations accounting for the elec-

tron bunch energy spread and the microwave instability, the resulting system is a 1-dimensional dynamical model of the storage ring free electron laser. Finally, we will present and discuss some preliminary simulation results compared with the Super ACO FEL.

3.1.1 Haissinski equation

The time evolution of the longitudinal phase-space distribution of the particles in a storage ring, $\psi(\epsilon, \xi)$, is given by the Fokker-Planck equation as:

$$\begin{aligned}\frac{\partial}{\partial t}\psi = & -\frac{\epsilon}{\sigma_{\epsilon,0}}\frac{\partial}{\partial \xi}\psi - \frac{\alpha_c\, b}{\omega_s}\frac{\partial}{\partial \epsilon}(\epsilon\psi) + \left(\xi - \frac{e^2\, N_e S}{\omega_s \sigma_{\epsilon,0}\, T_0\, E_0}\int_{\xi}^{\infty} d\xi' \rho\left(\xi'\right) W_w\left(\xi' - \xi\right)\right)\sigma_{\epsilon,0}\frac{\partial}{\partial \epsilon}\psi \\ & + \frac{\alpha_c\, D}{\omega_s}\frac{\partial^2}{\partial \epsilon^2}\psi,\end{aligned} \tag{3.1}$$

with ϵ the relative energy to the electron nominal energy E_0, ξ the normalized longitudinal position, which is linked to the position z of the electron with respect to the synchronous particle by

$$\xi = \frac{\omega_s}{\alpha_c c \sigma_{\epsilon,0}} z, \tag{3.2}$$

with ω_s the synchrotron frequency, α_c the momentum compaction factor, c the speed of light, and $\sigma_{\epsilon,0}$ the natural energy spread of the beam. The period of the electrons on the ring is T_0, the number of electrons in the ring is N_e, and e is the elementary charge. The damping coefficient due to synchrotron radiation is b, and the diffusion coefficient is D, which accounts for the quantum excitation due to photon emission. In equation (3.1) the expression $V(\xi) = S\int_{\xi}^{\infty} d\xi' \rho(\xi') W_w(\xi - \xi')$ represents the wake potential, and S a constant depending on the nature of the wakefield, which we will specify later on. The wake function $W_w(\xi)$ is the inverse Fourier transform of the storage ring impedance.
The Haissinski equation [2] is given by the static solution of the Fokker-Planck equation, assuming that the diffusion coefficient is $D = b\,\sigma_{\epsilon,0}^2$ and that the solution can be written as

$$\psi(\epsilon, \xi) = e^{-\frac{\epsilon^2}{2\sigma_{\epsilon,0}^2}} \rho(\xi), \tag{3.3}$$

where ρ represents the beam distribution as a function of the variable ξ. The form of the Haissinski equation depends on the wakefield, which is given by the Fourier transform of the storage ring impedance [3]. The Haissinski equation can be expressed as:

$$\rho(\xi) = A\, e^{-\frac{\xi^2}{2} - S\int_{\xi}^{\infty} d\xi' \int_{\xi'}^{\infty} d\xi" \rho(\xi") W_w(\xi' - \xi")}. \tag{3.4}$$

A storage ring may be described in terms of an LCR circuit, where the impedance of such a circuit is associated with the wakefield. By definition, the impedance of a storage ring is the Fourier transform of the wakefield. The nature of the wake is

then associated with the resistive, inductive or capacitive character of the associated impedance. In general a good approximation of the impedance of modern rings is a resistive-inductive impedance. The effect of a capacitive impedance are negligible [4]. We will present here analytical solutions for the purely resistive wake, equation recognized as a Riccati's equation, and for the purely inductive impedance. Out of an original work, I recently found the solution for the latter case [5].

3.1.2 Purely resistive case

Cavities, like RF cavities for example, tend to be resistive objects [4]. Then the wake function is given by the Dirac functional and the wake potential associated with such objects is:

$$V(\xi) = S_R \int_{\xi}^{\infty} d\xi' \rho(\xi') \delta(\xi - \xi'), \tag{3.5}$$

where S_R is the dimensionless parameter accounting for the resistance, and $\delta(\xi)$ the Dirac functional.

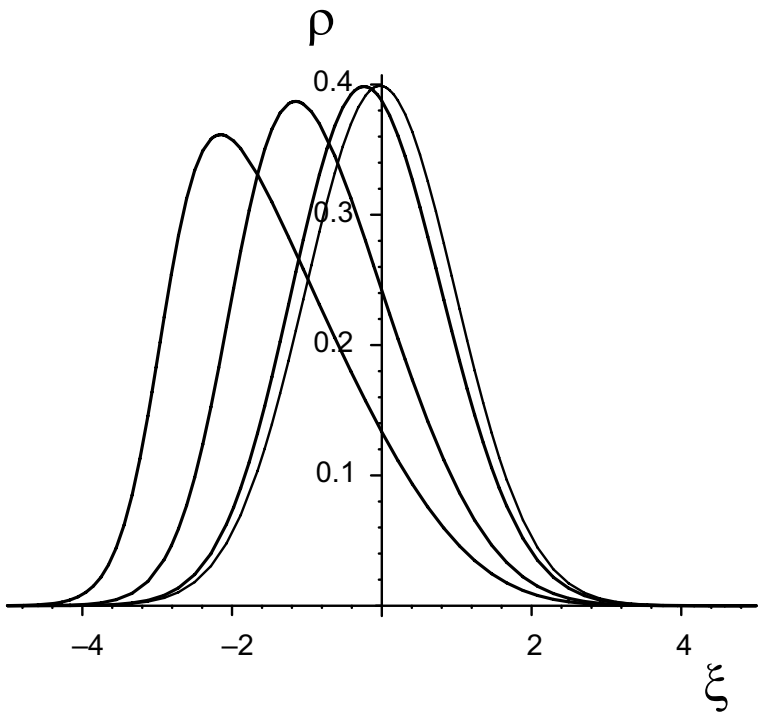

Figure 3.1: *Bunch distribution, $\rho(\xi)$, solution of the Haissinski equation for a purely resistive wake. The different values from the smallest distortion to the biggest are $S_R = 0.059, 0.59, 2.97$ and 5.95, which corresponds, with $R = 411\,\Omega$, to bunch average current of $I = 0.5, 5, 25$ and 50 mA respectively.*

Using (3.5), equation (3.4) may be re-written as a differential equation as:

$$\rho' = -(\xi + S_R\,\rho)\,\rho, \tag{3.6}$$

where the $'$ refers to the derivative with respect to ξ. This equation, as mentioned, is a Riccati's equation and has an analytical solution, which is:

$$\rho(\xi) = \sqrt{\frac{2}{\pi}} \frac{1}{S_R} \frac{e^{-\frac{\xi^2}{2}}}{\mathrm{erf}(\frac{\xi}{\sqrt{2}}) + \coth(\frac{S_R}{2})}, \tag{3.7}$$

with $S_R = \dfrac{R\,Q}{T_0\ (E_0/e)\ \alpha_c\, \sigma_{\epsilon,0}}$, where R is the resistance, and Q is the total charge of the bunch.

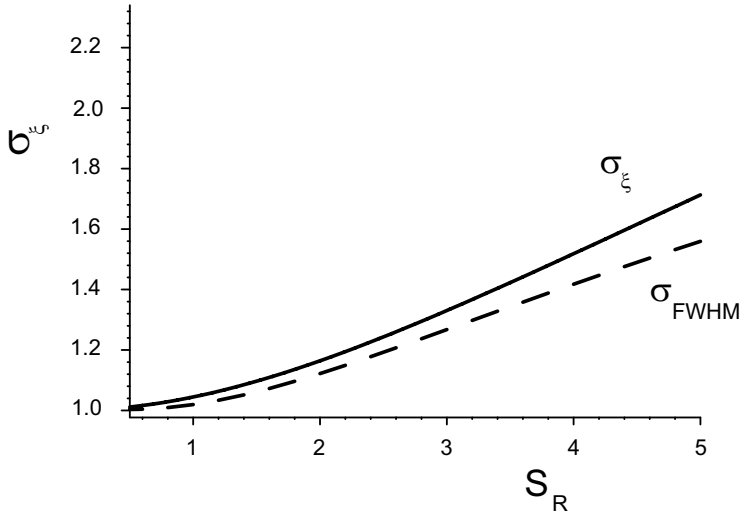

Figure 3.2: *r.m.s bunch length as function of S_R and the FWHM value divided by 2.35, σ_{FWHM}, of the solution of the Haissinski equation for a purely resistive wake.*

The r.m.s bunch length, σ_ξ, and the value calculated with the FWHM value $\sigma_{FWHM} = \Delta\xi_{FWHM}/2.355$ of the solution of the Haissinski equation for a purely resistive wake, are comparable in the range of current considered here. Figure (3.2) shows the bunch length and σ_{FWHM}. The bunch lengthening is negligible only for small values of S_R, but for high values the purely resistive wake induces a bunch lengthening referred as the potential well distortion [6].

Another effect of a resistive wake is to distort the bunch longitudinal distribution as can be observed in figure (3.1). This results in a displacement of the bunch centroid towards the head of the bunch, as can be observed in figure (3.3).

3.1.3 Purely inductive case

The case of the purely inductive impedance* has been observed in storage rings like the SLC damping rings [4] and at KEK [7].

Approximated solutions of the Haissinski equation have been extensively investigated numerically [4]-[8]-[9]. We note that an analytical solution of this equation exists. This solution is given by a particular expression of the so-called Lambert W function [10], which appears frequently in applied mathematics and has important application in

*The subsections from 3.1.3 to 3.1.5 concerning the Haissinski solution in purely inductive wake is published in the present form in [5]

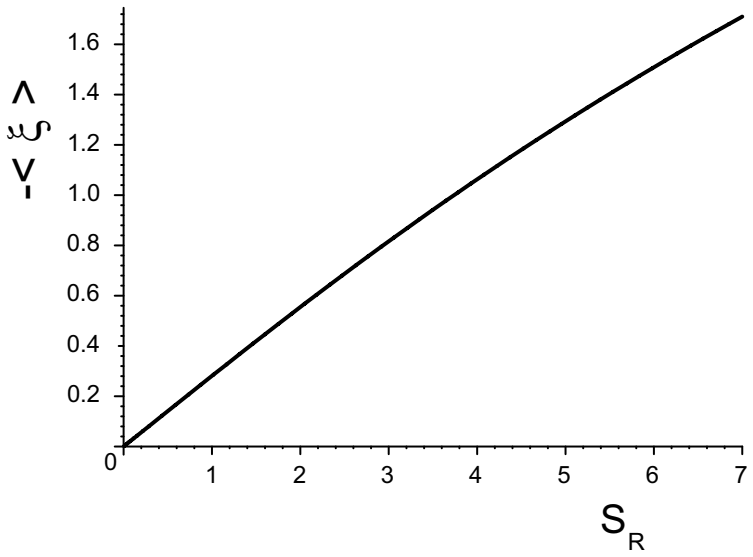

Figure 3.3: *Bunch centroid as function of S_R, of the solution of the Haissinski equation for a purely resistive wake.*

many other fields [11]-[12]. In this subsection we present the Lambert W function and analyze the nature of the analytical solution of the Haissinski equation in the case of a purely inductive impedance.
The wake potential in the purely inductive case is:

$$V(\xi) = S \int_{\xi'}^{\infty} d\xi' \rho(\xi') \delta'(\xi - \xi') \tag{3.8}$$

where δ' is the derivative of the Dirac functional, and S the parameter accounting for the inductance of the ring. Then the Haissinski equation in that case can be written in the form

$$\rho' = -\frac{\xi}{1 - S\rho}\rho, \tag{3.9}$$

The parameter S is specified in terms of the inductance of the wake field L, the revolution period T_0, the nominal energy of the particles E_0, the number of particles N, and also the synchrotron frequency, the natural energy spread, $\sigma_{\epsilon,0}$, and the elementary charge e, as

$$|S| = \frac{e^2 L N \omega_s}{\alpha_c^2 \sigma_{\epsilon,0}^2 T_0 E_0}. \tag{3.10}$$

Equation (3.9) can be rewritten in the following more convenient form

$$\ln(\rho) - S\rho = -\frac{\xi^2}{2} + \ln(A), \tag{3.11}$$

where A is the normalization constant defined by

$$\ln A = \ln\left(\rho\left(0\right)\right) - S\rho\left(0\right). \tag{3.12}$$

Equations of the type (3.9) above have a natural analytical solution in terms of the function known as the Lambert W function [10] . This function appears in many branches of pure and applied mathematics, may be a useful tool for the solution of many dynamical problems [11]-[12] and is not as widely known as it should be.
The Lambert W function, $W(z)$, is implicitly defined as the root of the following equation

$$W(z)\exp(W(z)) = z, \tag{3.13}$$

and explicitly by the series expansion

$$W(z) = \sum_{n=0}^{\infty} \frac{(-n)^{n-1}}{n!} z^n, \tag{3.14}$$

converging for $|z| < \frac{1}{e}$. In the forthcoming sections other expansions of W, holding in a wider range, will be exploited.

3.1.4 The Haissinski equation for an inductive wake and singularities

It is well known and evident that if S is negative, equation (3.9) has no singularity and there is always a unique continuous solution [8].
In the case of positive S the solution exists, but the presence of a singularity point limits the validity of the solution to a restricted range of S-values, which will be specified in the following.
According to equations (3.13) and (3.14) the solution of equation (3.9) can be written as an infinite sum of Gaussians, namely

$$\rho = -\frac{W(-AS\exp(-\frac{\xi^2}{2}))}{S} = \frac{1}{S}\sum_{n=1}^{\infty} \frac{n^{n-1}}{n!}(AS)^n \exp(-n\frac{\xi^2}{2}). \tag{3.15}$$

The argument of the Lambert W function has to be real and greater than $-\dfrac{1}{e}$ to define a singled valued function as a real physical distribution, which is not assured by the multivalued function Lambert W defined for any complex argument.
The convergence of the above series depends on the real value of AS. According to the indications of the previous section we find that the validity of the solution does not extend to all the values of the constants A and S, but holds for

$$AS \leq \frac{1}{e}. \tag{3.16}$$

The upper limit, associated with a branch point of the Lambert W function, clarifies the role of the singularity.
We would like to mention that a recent analysis of the problem demonstrated the singularity was linked to the *Boussard* threshold for the onset of the microwave instability. The singularity defines a point where the distribution is not normalizable, i.e. not a physical distribution, and defines a point where an instability arises.
We can now exploit equation (3.15) to specify the normalization of the distribution ρ,

and the role of A and S.
It is evident that from equation(3.15) the normalized distribution is given by the value A solving for a given S

$$S = \int_{-\infty}^{\infty} W(-SA\exp(-\frac{\xi^2}{2}))d\xi = \sqrt{2\pi}\sum_{n=1}^{\infty}\frac{n^{\frac{2n-3}{2}}}{n!}(AS)^n. \tag{3.17}$$

The r.h.s of equation (3.17) is a series converging with the same range imposed by (3.16).
By taking for AS the upper limit of convergence and by using the Stirling approximation

$$n! \simeq \sqrt{2\pi n}n^n e^{-n}, \tag{3.18}$$

we find the maximum value of S

$$S^* \simeq \sum_{n=1}^{\infty}\frac{1}{n^2} = \frac{\pi^2}{6}. \tag{3.19}$$

This is a rough approximation and the exact computation (given by the computing algebra software Maple) yields

$$S^* \simeq 1.550608..., \tag{3.20}$$

which is very close to the value given in [13], and more accurate than the previous value given in the literature [6].
It is important to emphasize that the distribution (3.15) exhibits an r.m.s value σ_ξ below 1. In physical terms, this means that an electron bunch experiencing a purely inductive wake with $S > 0$, due to e.g. a negative momentum compaction factor, may have a length lower than the natural value, provided by[†] $\sigma_b = \frac{c\alpha_c}{\omega_s}\sigma_{\epsilon,0}$.
The behavior of σ_ξ as function of AS is given in figure (3.4) and the limiting value, calculating with the Stirling approximation, but very close to the exact value, is

$$\sigma_\xi^* = \sqrt{\frac{6}{\pi^2}\sum_{n=1}^{\infty}n^{-3}} \simeq 0.854846.... \tag{3.21}$$

The results obtained so far, apart from providing an analytical solution for equation (3.9) have clarified the nature of the singularity associated with the limits of validity of the Taylor expansion of the Lambert W function and the range of S values ($S < S^*$) for which equation (3.9) admits a normalizable solution.
Before concluding this subsection let us note that the series expansion of the solution (3.15) can be extended to negative values of S too, provided that $SA < \frac{1}{e}$. An idea of the behavior of the solution, for $AS \to \frac{1}{e}$ and for $AS \to \frac{-1}{e}$, is given is figure (3.5). As it is evident for positive (AS) values the distribution is clearly similar to the Gaussian with an r.m.s slightly larger than the natural value. On the contrary for negative (AS) values the shape is significantly different from a Gaussian.

[†]Here we use the term $\sigma_b = c\sigma_\tau$ given in chapter 2

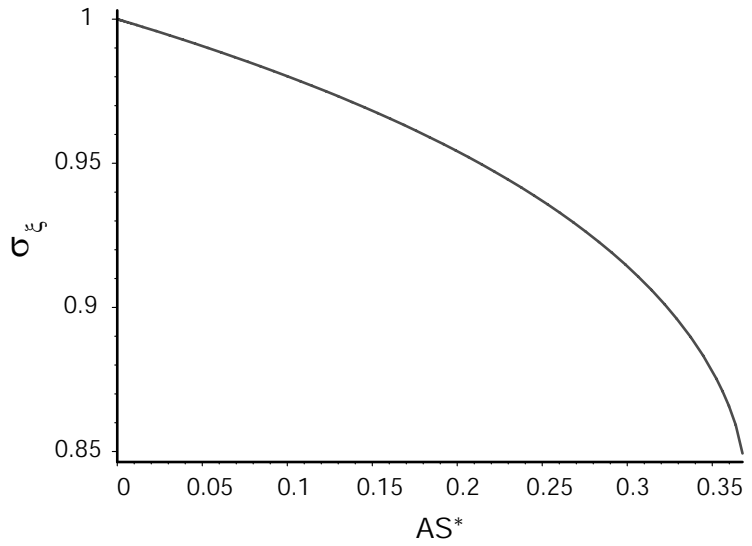

Figure 3.4: *The bunch length, σ_ξ, as function of AS^*.*

The possibility of obtaining a valid solution for a positive AS in a larger interval will be discussed in the following concluding section.

3.1.5 Positive momentum compaction factor: $S < 0$

In the previous subsection we have explored the solution of the Haissinski equation for a purely inductive wake using the Taylor expansion of the Lambert W function which has a limited convergence radius. Now we will see how a different expansion, admitting a larger radius of convergence, can be exploited to get a non trivial and useful form of solution valid for negative S-values. To this aim we note that, for the present problem, a natural alternative to the Taylor expansion, is provided by [12]

$$\begin{aligned} W(\exp(z)) = \quad & 1+\frac{1}{2}(z-1)+\frac{1}{16}(z-1)^2-\frac{1}{192}(z-1)^3 \\ & -\frac{1}{3072}(z-1)^4+\frac{13}{61440}(z-1)^5+O((z-1)^6), \end{aligned} \tag{3.22}$$

whose radius of convergence is $\sqrt{4+\pi^2}$.
According to the previous relation we can write the solution of (3.9) in the form ($\Lambda = -S$)

$$\begin{aligned} W(A\Lambda\exp(-\frac{\xi^2}{2})) = \quad & 1+\frac{1}{2}(-\xi^2/2+\ln\frac{A\Lambda}{e})+\frac{1}{16}(-\xi^2/2+\ln\frac{A\Lambda}{e})^2 \\ & -\frac{1}{192}(-\xi^2/2+\ln\frac{A\Lambda}{e})^3-\frac{1}{3072}(-\xi^2/2+\ln\frac{A\Lambda}{e})^4 \\ & +\frac{13}{61440}(-\xi^2/2+\ln\frac{A\Lambda}{e})^5+O((-\xi^2/2+\ln\frac{A\Lambda}{e})^6). \end{aligned} \tag{3.23}$$

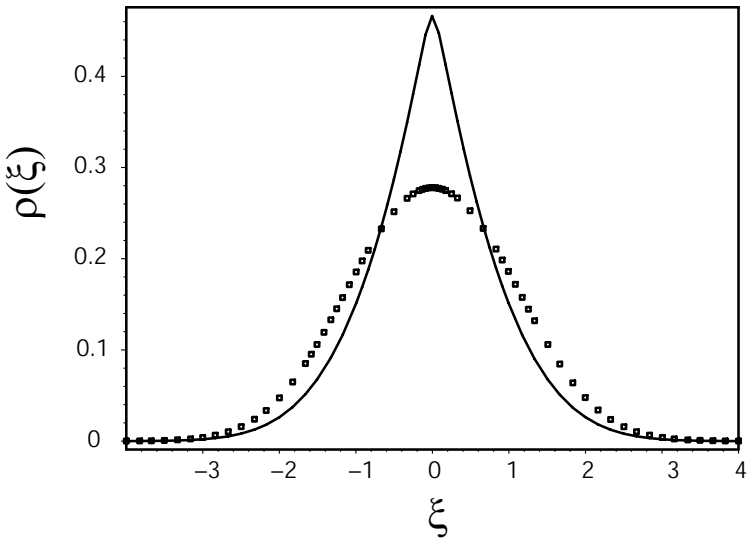

Figure 3.5: *The bunch distribution in the case* $AS \simeq \frac{1}{e}$ *(squares) and in the case* $AS \simeq -\frac{1}{e}$ *(line).*

The above solution shows that the charge distribution, in the case of a perfect inductor is symmetric about $\xi = 0$ and tends to a parabolic shape for $A\Lambda \gg 1$.
A comparison between analytical and numerical solution is offered by figure (3.6) and the agreement is more than satisfactory.
As a further comment we remark that the series converges for $A\Lambda \leq 41.4$, which is a good range for the specific problem we are considering.
It is also worth noting that it can be easily verified that the normalization constant can be directly inferred and read ($\chi = A\Lambda$)

$$\tilde{N} = \int_{-\infty}^{\infty} \rho\left(\xi\right) d\xi \simeq 3.1\chi^{\frac{1}{3}}, \tag{3.24}$$

while the second order normalized momentum can be written as

$$\sigma_{\xi}^{2} = \frac{1}{\tilde{N}} \int_{-\infty}^{\infty} \xi^{2} \rho(\xi) d\xi \simeq 1.058(\chi + 5)^{\frac{1}{6}}. \tag{3.25}$$

Therefore for large χ, and thus for large current, the r.m.s value of the distribution scales roughly as $\tilde{N}^{\frac{1}{4}}$.
In conclusion it is also interesting to mention the possibility of exploiting an asymptotic solution of the Haissinski equation valid for large χ values, namely [12]

$$\begin{aligned} W(z(\xi,\chi)) \approx \quad & \ln z(\xi,\chi) - \ln\left(\ln\left(z(\xi,\chi)\right)\right) + \\ & \sum_{n=1}^{\infty} \frac{(-1)^{n}}{\ln\left(z(\xi,\chi)\right)^{n}} \sum_{m=1}^{\infty} \frac{(-1)^{m} n! \ln\left(\ln\left(z(\xi,\chi)\right)\right)^{m}}{(n-m+1)!m!} \end{aligned} \tag{3.26}$$

with $z(\xi,\chi) = \chi \exp(-\frac{\xi^{2}}{2})$
The above expression can be used as bench-marking of the numerical solutions for values above the convergence radius of the expansion (3.23).

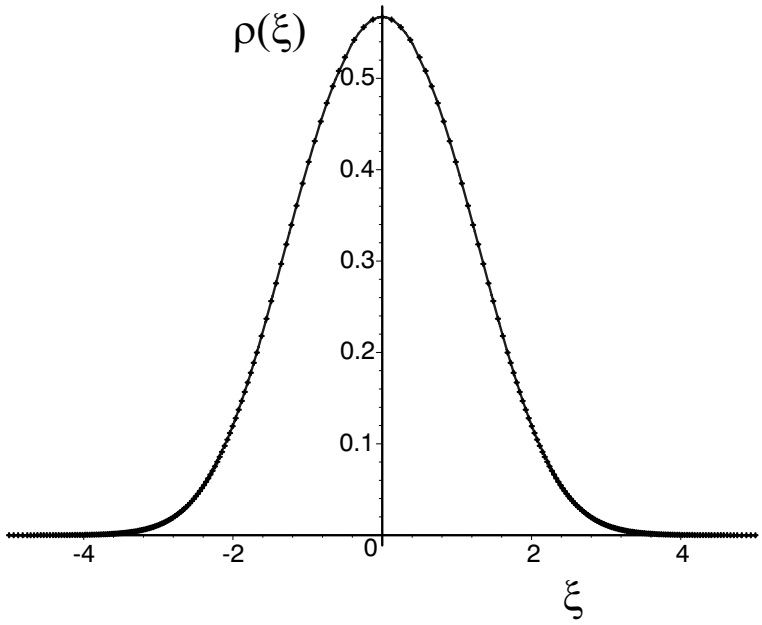

Figure 3.6: *Comparison between analytical (line) and numerical (points) solution* $\rho(\xi)$ *of the Haissinski equation, for* $S = -1$ *and* $A = 1$*. The maximum error is less than* 10^{-6}.

We must however underline that the series (3.26) being an asymptotic expansion, can not be viewed as a real distribution since we cannot define a normalization factor, although the series is convergent.

3.1.6 Electron dynamics and microwave instability

The microwave instability (MI) can seriously limit the performances of the new generation of storage rings. It manifests itself as an increase of energy spread with a consequent anomalous bunch lengthening. For example a bunch lengthening by more than a factor 2 is observed at Super ACO, and the consequent gain reduction for an SRFEL is then more than a factor 4.
The common approach for the study of this instability [6] is based on the study of the Vlasov equation, which describes the time evolution of the single bunch distribution function in the phase space. This function is considered as a superposition of a stationary distribution plus a time-dependent perturbation, represented by a sum of coherent modes of oscillation. The problem is linearized with respect to the perturbation, and a set of integral eigenvalue equations for the phase-space structure of the oscillation modes is finally derived. The different techniques used to find the solution [14] generally require hard computational efforts, and are not free from convergence problems. The threshold of the instability depends on the wake fields and on the current. Above the threshold the linear theory can not explain the time evolution of the distribution function. The increase of the bunch dimensions may provide the conditions for a new equilibrium configuration. In some cases, however, the equilibrium is never reached, the energy spread oscillates in time with a pattern similar to relaxation-type oscillations,

as shown in figure (3.7(a)). Such a behavior is generally referred to as the saw-tooth instability [6]-[15]-[16].

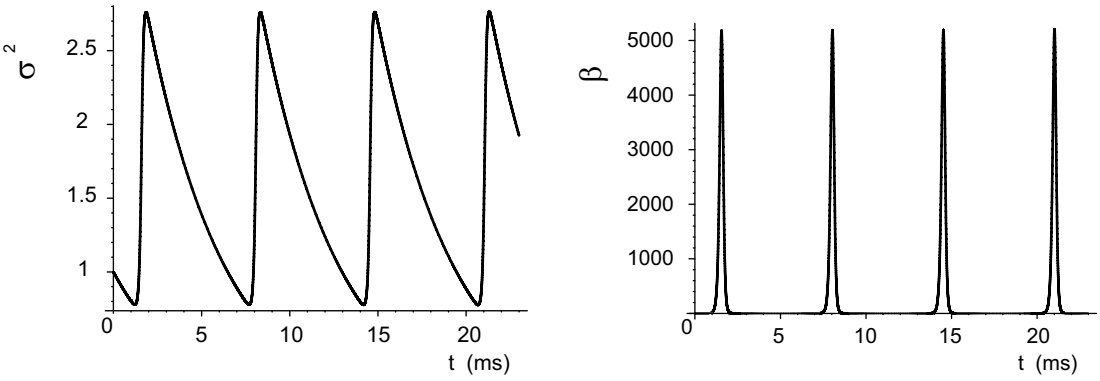

(a) (b)

Figure 3.7: *Saw-tooth instability: evolution of the relative energy spread 3.7(a) and the microwave instability growth rate 3.7(b) vs. time, using the solution of the expressions (3.27) and (3.28), with* $\tau_s = 9$ *ms,* $A = 6 \cdot 10^4\ s^{-1}$ *and* $B = 3 \cdot 10^4 s^{-1}$.

The problem has been treated in [15] obtaining an equation for the oscillation amplitude of a given eigenmode, under the hypothesis that only that mode dominates the dynamics of the microwave instability, that the instability develops on a time scale much larger than the period of eigenmode oscillations, and that it saturates at a level where the amplitude of the eigenmode oscillations is relatively small. With these assumptions, the evaluation of the non-linear equation in a real case is not easy. The simple model given here depends on two dimensionless parameters, describing the onset and the growth of the instability, and its relaxation.
The instability, introduced above, derived from the energy exchange between the electrons and the radiation reflected by the vacuum chamber and stored in the ring. The wavelength of the radiation is in the micrometer wavelength range. The energy exchange, as for the free electron laser, leads to energy spreading, and as a consequence to bunch lengthening. The bunch dynamics is then determined by the relative energy spread, σ_ϵ, and the bunch length is then assumed to be proportional to σ_ϵ. Transverse bunch perturbations are also neglected. This is modelled by coupling the differential equations for the energy spread and for MI growth in the bunch. These coupled equations are [16]-[17]:

$$\frac{\partial \sigma^2}{\partial t} = \beta \sigma^2 - \frac{2}{\tau_s}\sigma^2 \,, \tag{3.27}$$

$$\frac{\partial \beta}{\partial t} = \beta \left[A \left(1+\sigma^2\right)^{-\frac{1}{4}} - B \left(1+\sigma^2\right)^{\frac{1}{2}} \right] . \tag{3.28}$$

The variable β represents the MI growth rate. The energy spread increases due to the instability growth in the bunch; it is damped due to synchrotron radiation emitted by the electrons in the ring with the characteristic time τ_s, called synchrotron damping time.
The instability excitation parameter is:

$$A = \frac{\omega_c}{2\pi}\sqrt{\frac{(2\pi)^{\frac{1}{2}} I_0 \nu_s \left|\frac{Z_n}{n}\right|}{\frac{E_0}{e}\sigma_{\epsilon,0}}},$$

and is evaluated with ω_c, the bunch cut off frequency, the average current I_0, the synchrotron tune ν_s, the electron nominal energy E_0 and $\sigma_{\epsilon,0}$ and the ring normalized longitudinal impedance $\left|\frac{Z_n}{n}\right|$. For a purely inductive impedance, L, $\left|\frac{Z_n}{n}\right| = L\frac{2\pi}{T_0}$, and for a purely resistive impedance, R, $\left|\frac{Z_n}{n}\right| = \frac{R}{Z_0}$, with $Z_0 = 377\,\Omega$ the vacuum impedance.
The *Landau* instability damping parameter [16]-[18] is:
$B = \omega_c \alpha_c \sigma_{\epsilon,0}$,
and is determined by the momentum compaction factor α_c, $\sigma_{\epsilon,0}$ and ω_c.

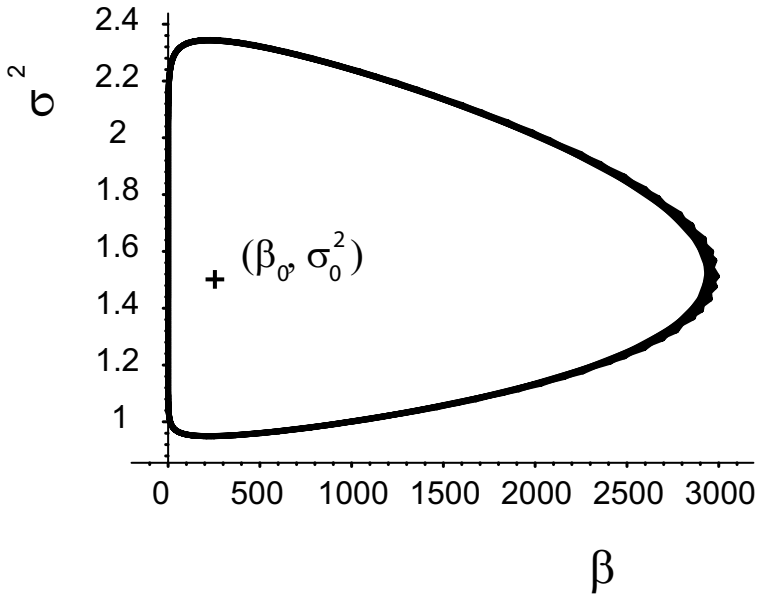

Figure 3.8: *Phase plane evolution of the system given by the expressions (3.27) and (3.28). The trajectory converges to the closed loop trajectory around the singularity (β_0,σ_0^2).*

The behavior of the system can be seen in figure (3.7). The typical behavior is a periodical motion. The energy spread increases due to the MI growth in the bunch, following by a bunch lenghtening. The increase of energy spread then participate to the damping of the MI. When σ^2 is large enough, the MI is damped and the bunch relaxes towards its natural energy spread value. When σ^2 is lower than the threshold value, $\sigma_{th}^2 = \left(\frac{A}{B}\right)^{\frac{4}{3}} - 1$ (Boussard criterion [19]), the MI starts again.
This cycle can be seen with the same analysis perfomed in chapter 2 on the 0-dimensional model. This time the singularity ($\sigma_0^2 = \sigma_{th}^2$, $\beta_0 = \frac{2}{\tau_s}$) is a vortice, so that the phase plane trajectory is a closed loop curve at infinite time, as can be seen in figure (3.8).

3.2 1-DIMENSIONAL MODEL OF THE LASER DYNAMICS

We implemented a 1-dimensional model in a numerical code. The model focuses on the longitudinal axis, neglecting the transverse effects, and on the main physical

parameters that lead the longitudinal dynamics. This code, although quite simple, gives a direct insight in the evolution of the optical wave electric field. By coupling the laser evolution with the dynamics of macroscopic electron bunch quantities, it simulates the interplay between the laser pulse, the electron bunch and the main instability, which affects the beam, the microwave instability (MI) [17]-[18]-[20]. Furthermore the numerical values of the dimensionless parameters, as appearing in the semi-analytical model and as used in the code, are derived from the real parameters that characterize a SRFEL, thus allowing to compare the numerical results with experimental ones. We took the Super-ACO FEL as an example.

3.2.1 Introduction

Describing the SRFEL dynamics and the interplay between the laser pulse and the electron bunch is done by coupling the equations accounting for the laser pulse intra-cavity evolution and the evolution of parameters of the stored electron bunch. The first equation in this model is the differential equation of the dimensionless intra-cavity complex amplitude of the laser electric field, $a(z,t)$, where t is the time and z is the longitudinal coordinate along the optical cavity axis. The origin of the z-axis is taken at the center of the cavity; distances are normalized with respect to the electron bunch length, σ_b. The length σ_b is dependent on the current I_0 in the ring. Radial symmetry is assumed, hence transverse effects are not taken into account. At each point on the z-axis the differential equation for the complex amplitude is evaluated, providing the laser pulse longitudinal distribution and its evolution. A moment method is used to analyze the laser pulse longitudinal distribution: the first order moment gives the centroïd of the pulse, and the second order moment the pulse length. The dimensionless intra-cavity energy density is $\langle|a(z,t)|^2\rangle = \int_{-\infty}^{\infty}|a(z,t)|^2 dz$.
The differential equations for the complex amplitude contain four terms accounting for the cavity tuning, the gain, the total cavity loss and the spontaneous emission. The gain here is evaluated for an undulator containing N_u periods of length λ_u. The case for an optical klystron is dicussed in the next subsection, providing the fact that the model presented here can be applied to SRFEL operating with an optical klystron. The resonant wavelength emitted in the undulator is $\lambda_r = \frac{\lambda_u}{2\gamma^2}\left(1+\frac{K^2}{2}\right)$, where $K = [0.94 cm^{-1}T^{-1}]\lambda_u B$ is the magnetic undulator strength, and B is the r.m.s amplitude of the magnetic field.
The intra-cavity peak power is linked to $\langle|a(z,t)|^2\rangle$ by the expression: $P[MWcm^{-2}] = \langle|a(z,t)|^2\rangle\, I_s\, \omega_0$, where $I_s[MWcm^{-2}] = 690[MW](\frac{\gamma}{N_u})^4((\lambda_u[cm]K f_b(\xi))^2)^{-1}$, and $f_b(\xi)$ is the difference between the first kind Bessel functions of the orders 0 and 1 with the argument $\xi = \frac{K^2}{4+2K^2}$, and ω_0 is the beamwaist.
The equation for the complex amplitude laser electric field is [21]:

$$\begin{aligned}\frac{\partial a(z,t)}{\partial t} &= \frac{1}{T_c}\left[a(z-4\delta L,t)-a(z,t)\right] \\ &-i\frac{2\pi g_0}{T_c\Delta^3\left(1+\sigma^2\right)^{\frac{1}{2}}}\int_0^{\Delta} dyya(z+y,t)\,e^{-i\frac{\nu y}{\Delta}-\frac{(\pi\mu_\epsilon y)^2\left(1+\sigma^2\right)}{2\Delta^2}}\int_{z+y}^{z+\Delta} dz_1 e^{-\frac{z_1^2}{2(1+\sigma^2)}} \\ &-\frac{1}{T_c}(\eta a(z,t)+S_r(z)). \end{aligned} \tag{3.29}$$

The first term of the right hand side of the equation represents the cavity tuning, with T_c the pulse period in the cavity and $4\delta L = \theta g_0 \Delta$ the longitudinal tuning term; θ is a real number; g_0 is the maximum gain; $\Delta = N_u\dfrac{\lambda_r}{\sigma_b}$ is the slippage length, normalized to the initial bunch length, σ_b [‡]. The second term, the double integral, evaluates the gain of the complex amplitude over the normalized slippage length Δ. Furthermore $\sigma^2 = \left(\dfrac{\sigma_\epsilon}{\sigma_{\epsilon,0}}\right)^2 - 1$ is the increase of relative energy spread with $\sigma_{\epsilon,0}$ the natural relative energy spread at zero current and no laser. $\nu = 2\pi N_u\dfrac{\lambda-\lambda_r}{\lambda_r}$ is the spectral detuning parameter defining the laser wavelength λ, $\mu_\epsilon = 4N_u\sigma_{\epsilon,0}$ is the inhomogeneous broadening parameter. Finally η is the total cavity losses and the spontaneous emission is given by a Gaussian function, $S_r(z)$, homothetic to the bunch distribution, e.g. a Gaussian distribution with its maximum $S_r(0) \ll 1$.
Equation (3.29) can be coupled with the equations, presented in the previous subsection, which describe the energy spread and the microwave instability evolution. These equation can be writen as:

$$\begin{aligned}\frac{\partial\sigma^2}{\partial t} &= \beta\sigma^2 - \frac{2}{\tau_s}\left(\sigma^2 - \left\langle|a(z,t)|^2\right\rangle\right), \\ \frac{\partial\beta}{\partial t} &= \beta\left[A\left(1+\sigma^2\right)^{-\frac{1}{4}} - B\left(1+\sigma^2\right)^{\frac{1}{2}}\right].\end{aligned} \tag{3.30}$$

The coupling between the laser and the electron bunch energy spread is provided here by the intra-cavity dimensionless laser power, which induces energy spread to the bunch, lowering in the same time the laser gain.

3.2.2 Undulator vs. optical klystron model

The dynamics[§] of a storage ring free electron laser (SRFEL) may depend on whether there is an undulator or an optical klystron in the optical cavity of the laser. In order to investigate this difference, a model of the gain for the case of an optical klystron

[‡]we use the term $\sigma_b = c\sigma_\tau$ for the bunch length expressed in meter.

[§]The subsections from 3.2.2 to 3.2.4 have been accepted for publication in Nucl. Intr. & Methods A under the title "Undulator vs. optical klystron induced dynamics of a storage ring free electron laser".

has been developed based on the work presented in [22] : we reviewed and corrected the analysis (in this subsection) and implemented the new expression of the gain in our 1-dimensional numerical code [23]. Previously this code was used, with the gain expression for an undulator equivalent to the optical klystron (descibed in the previous subsection). The results were in good agreement with experimental measurements, in particular for the Super ACO free electron laser [23].
One may expect differences between this approach, i.e. evaluating the gain from the optical klystron and the previous approach with an equivalent undulator. To establish the magnitude of these differences, we simulated the case of Super ACO, with the new expression for the optical klystron gain, and compared it with our previous results using an equivalent undulator.
The gain for a free electron laser, along the propagation axis, can be derived from the propagation equation for the case of an undulator [21] and for the case of an optical klystron [22]. An optical klystron consists of two undulators of N_u periods each, separated by a dispersive section. The equation describing the gain for the optical klystron, at a given position z on the longitudinal axis, is given by the convolution of the laser pulse and the electron bunch along the slippage length:

$$\begin{aligned} G(\sigma,\nu) &= -i\frac{2\pi\, g_0}{\Delta^3\,(1+\sigma^2)}\int_0^{\Delta} dy\, y\, a(z+y,t)\, Q(\nu\frac{y}{\Delta},\delta) \\ & \quad e^{-\frac{(\pi\mu_\delta y)^2\,(1+\sigma^2)}{2\,\Delta^2}} \int_{z+y}^{z+\Delta} dz'\, f_e(z')\,, \end{aligned} \tag{3.31}$$

where $\sigma_\epsilon = \sigma_{\epsilon,0}\sqrt{1+\sigma^2}$ is the induced energy spread, $\nu = 2\,\pi\,N_u\frac{\lambda-\lambda_r}{\lambda_r}$ is the spectral detuning, λ the laser wavelength and λ_r the undulator resonant wavelength, and g_0 is the small signal gain associated with one undulator; the gain, $G(\sigma,\delta)$ is evaluated at a certain position z on the longitudinal axis (the optical cavity axis), which is normalized to the initial bunch length (σ_b). It takes into account the intra-cavity complex electric field amplitude of the laser, $a(z,t)$ as function of z and of the time t, as for a position z this amplitude evolves after successive interactions between the laser pulse and the electron bunch. The quantity $\Delta = N_u\,\lambda$ accounts for the slippage length in one undulator, normalized to σ_b, $\delta = \frac{N_d}{N_u}$ characterizes the dispersive section, with N_d the delay between photons and electrons in terms of resonant wavelength in the dispersive section, $\mu_\delta = 8\,\pi\,N_u\,\sigma_{\epsilon,0}\,(1+\delta)$ is the electrons energy inhomogeneous broadening. The electron bunch distribution, f_e, at the first order taking the distribution from the solutions of the Haissinski equation, is a Gaussian with an r.m.s value proportional to the energy spread. Finally $Q(\nu,\delta)$ is a complex function, resulting from the interaction in the first undulator and in the second undulator following the dispersive section:

$$Q(\nu,\delta) = 8(1+\frac{\delta}{2})^3 e^{2\,i\,\nu\,(1+\frac{\delta}{2})} + \delta^3\, e^{2\,i\,\nu} + 2(e^{i\nu} - (1+\delta)^3\, e^{i\nu(1+\delta)}). \tag{3.32}$$

The code we implemented uses the expression (3.31) for the complex gain. It integrates three differential equations which are:

$$\begin{aligned} T_c\frac{\partial}{\partial t}a(z,t) &= (a(z-\delta L,t)-a(z,t))+G(\sigma,\nu)-\eta\, a(z,t)+S_r(z)\,, \\ \frac{\partial}{\partial t}\sigma^2 &= \beta\sigma^2-\frac{2}{\tau_s}(\sigma^2-\langle|a(z,t)|^2\rangle)\,, \\ \frac{\partial\beta}{\partial t} &= \beta\left[A\left(1+\sigma^2\right)^{-\frac{1}{4}}-B\left(1+\sigma^2\right)^{\frac{1}{2}}\right]. \end{aligned} \tag{3.33}$$

We note that when the dispersive section number $N_d = 0$, the gain expression reduces to the expression (3.29) for an undulator of $2\,N_u$ periods. This expression has been used at first in our code. In order to approximate the gain function of the equivalent undulator, we equal g_0 to the small signal gain of the optical klystron [24], and we equal the inhomogeneous broadening parameter to the one given by the optical klystron. We also evaluate the gain of the equivalent undulator over the same slippage length as in the optical klystron, $\Delta = (N_u + N_d)\,\lambda$.

3.2.3 The gain function

The expression (3.31) for the gain depends on two important parameters, the spectral detuning, ν, and the induced energy spread. Figure (3.9) presents the real and imaginary part of the complex function G, in the case of an optical klystron and in the undulator case, as function of the spectral detuning. The parameters are the following: $\sigma = 0$, $z = 0$ (center of the bunch, which coincides with the center of the pulse), Gaussian distribution for the electron bunch and the laser pulse with the same length as the bunch. The initial gain g_0 has been set to 1 for the case of the optical klystron and is set to the equivalent optical klystron gain for the undulator case. Due to the fringe pattern of the optical klystron gain function vs. ν, the maximum value of the gain will be obtained for a different ν value, giving a slightly different laser wavelength. But the spectral dependency of the gain does not influence the dynamics.

The energy spread dependency of the gain is the main parameter for the laser dynamics. The energy spread reduces the gain. As the laser intra-cavity power induces energy spread, this is the main process leading to saturation. Consequently the gain as function of the energy spread has to be properly modelled for the case of the optical klystron. Figure (3.10) presents the maximum gain curves still at $z = 0$ as function of the energy spread, for several values of the dispersive section number δ, for the optical klystron case and the equivalent undulator. The first remark is that the gain function is not really different in the two cases. The difference starts to be visible for large values of δ, but the slope of the curve is similar and its general shape remains the same.

Figure (3.11) presents the modulus of the complex gain function vs. σ for $\delta = 10$ and $\delta = 30$, and in the undulator and optical klystron cases. Here we have normalized the gain to g_0. The difference between the equivalent undulator and the optical klystron gain functions may appear large, but in fact this difference has to be normalized to the maximum gain value at the start-up of the laser. Figure (3.12) shows the difference between the optical klystron and equivalent undulator gain functions normalized to $G(0,\delta)$. The maximum difference is only 8 % for σ values where the gain is three time less than the start up gain. This difference does not modify the laser dynamics and can be considered negligible. This explains our results in agreement with experiments

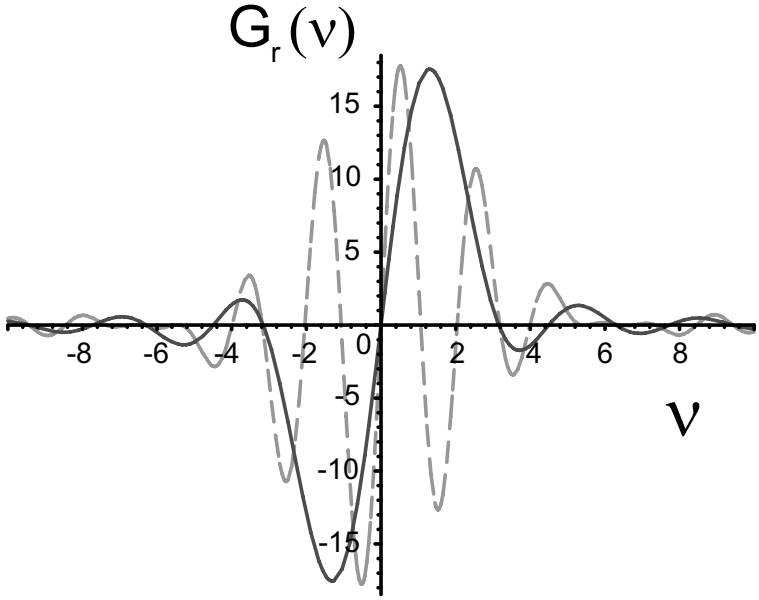

(a) Real Part of $G(0, \nu)$

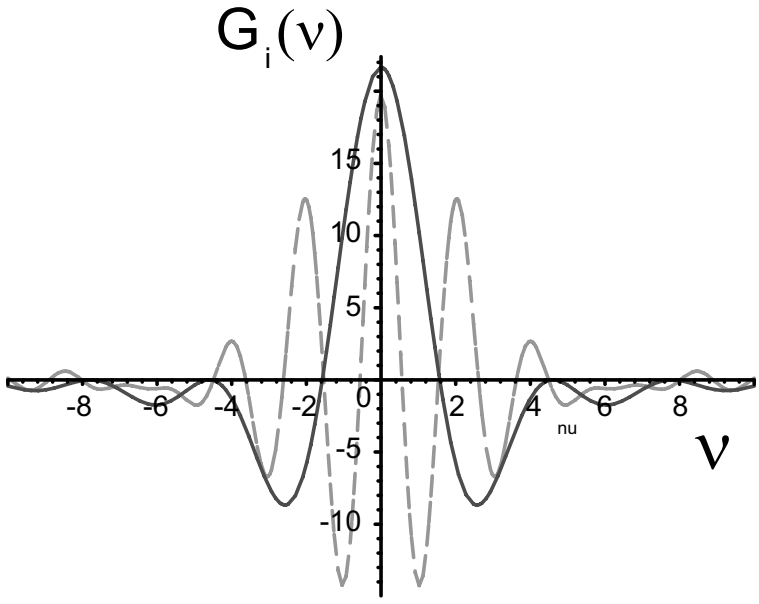

(b) Imaginary part of $G(0, \nu)$

Figure 3.9: *Real and Imaginary part of the gain as function of the spectral detuning ν in the undulator (solid line) and in the optical klystron (dash line) cases.* $g_0 = 1$, $\sigma_{\epsilon,0} = 5.4\,10^{-4}$, $\Delta = 0.001$, $\delta = 5$, $z = 0$.

using an equivalent undulator in our code. In the case of Super ACO, where $\delta \approx 10$, the equivalent undulator gain appears to be a reasonable approximation.

As a further remark the gain function vs. the dispersive section number δ has a maximum value for a finite value of δ, which is expected: as δ increases, the slippage length increases too, and for an infinite δ the laser pulse does not interact any more with the electron bunch in the second undulator of the optical klystron. This is illustrated

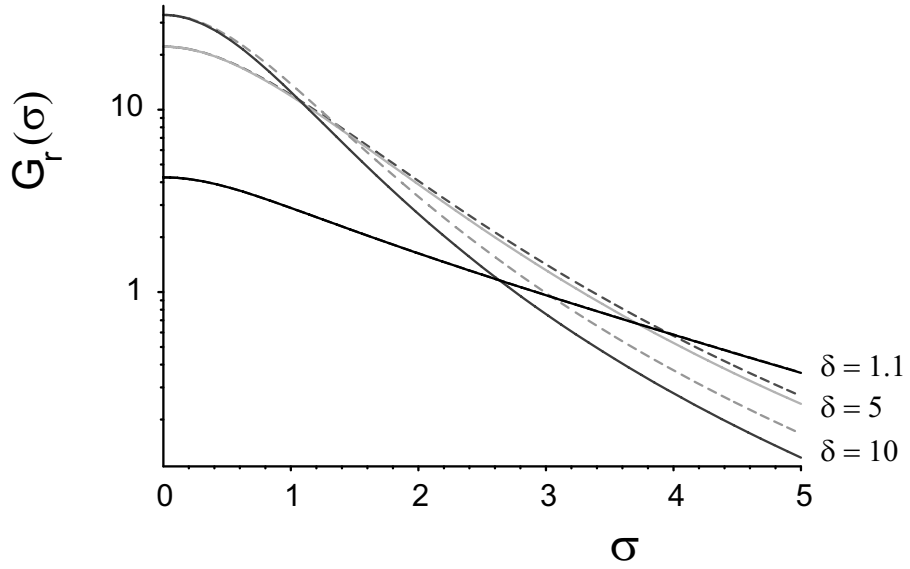

(a) Real Part of $G(\sigma, \nu)$

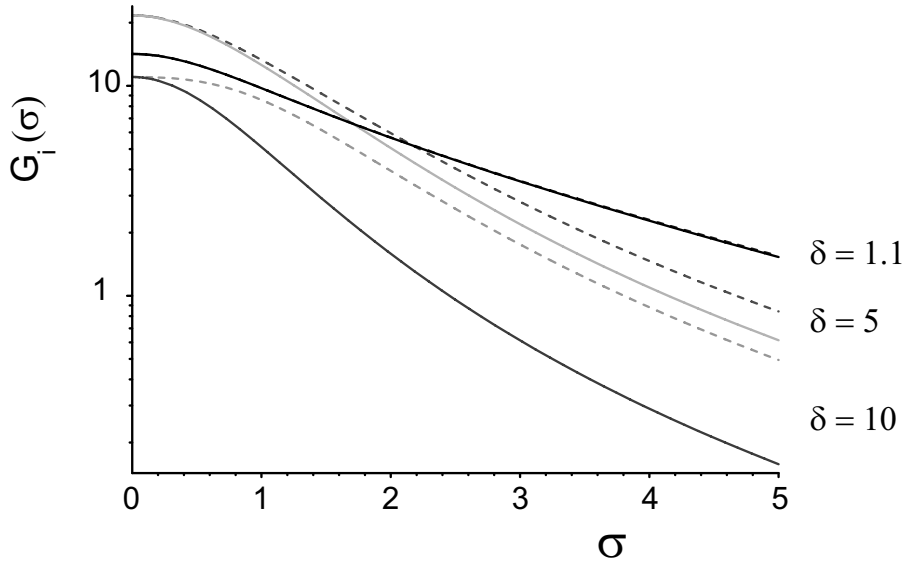

(b) Imaginary part of $G(\sigma, \nu)$

Figure 3.10: *Real and Imaginary part of the gain as function of the induced energy spread σ in the undulator (solid line) and in the optical klystron (dash line) cases. $g_0 = 1$, $\sigma_{\epsilon,0} = 5.4\,10^{-4}$, $\Delta = 0.001$, $z = 0$, $\nu = 0.15$, 1.3 for the optical klystron and the equivalent undulator respectively.*

in figure (3.13) which presents the maximum gain vs. δ for $z = 0$, $\epsilon = 0$ and $g_0 = 1$. It shows that the dispersive section number has to be optimized for a given optical klystron in order to maximize the gain.

3.2.4 Numerical results: undulator vs. optical klystron

In this section we compare the numerical results from our code based on the model described by (3.33), with our previous code, where the gain is evaluated using the

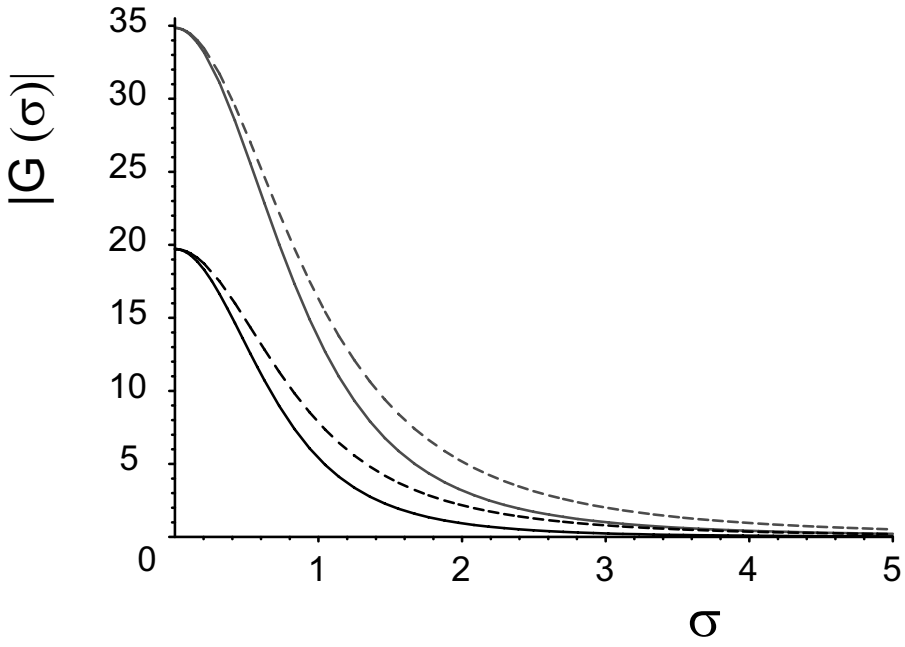

Figure 3.11: *Modulus of the $G(\sigma, \nu)$, for $\delta = 30$ (lower curve) and $\delta = 10$ (upper curve) in the optical klystron (dash) and undulator (line) cases.*

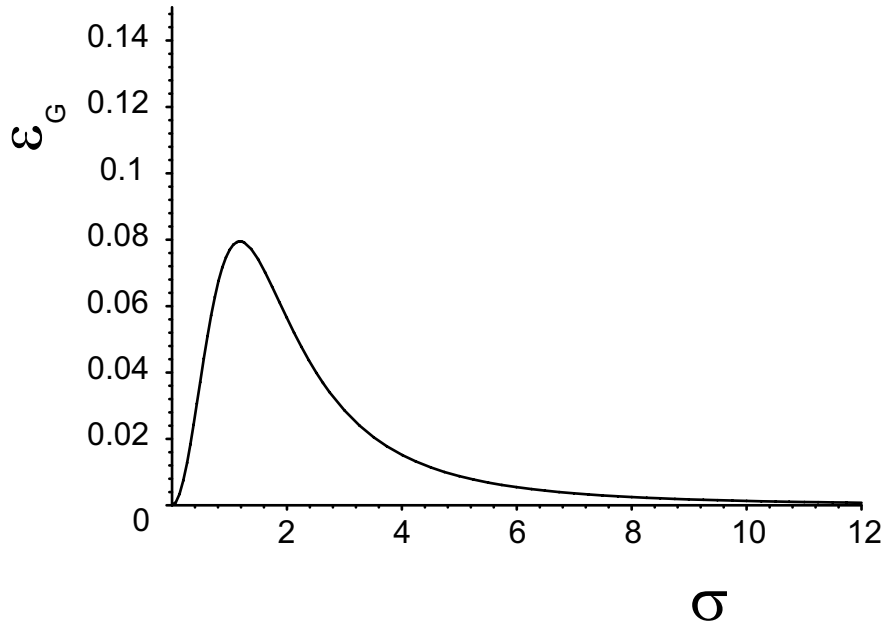

Figure 3.12: *Difference of the modulus of the gain functions for the equivalent undulator and optical klystron cases normalized to $|G(0, \nu)|$ for $\delta = 10$.*

equivalent undulator expression. We choose the case of Super ACO as an example. The initial gain in the two codes is 4 %: for the optical klystron we set g_0 so that $G_{0,OK} = 0.85\, g_0(1 + 0.932\delta) = 4\,\%$ [25], and in the equivalent undulator case $g_0 = 4\,\%$. We also need to set the inhomogeneous broadening parameters equal: in the optical klystron $\mu_\delta = 8\pi N_u(1 + \delta)$, and in the equivalent undulator $\mu_\epsilon = \mu_\delta$. The gain in the

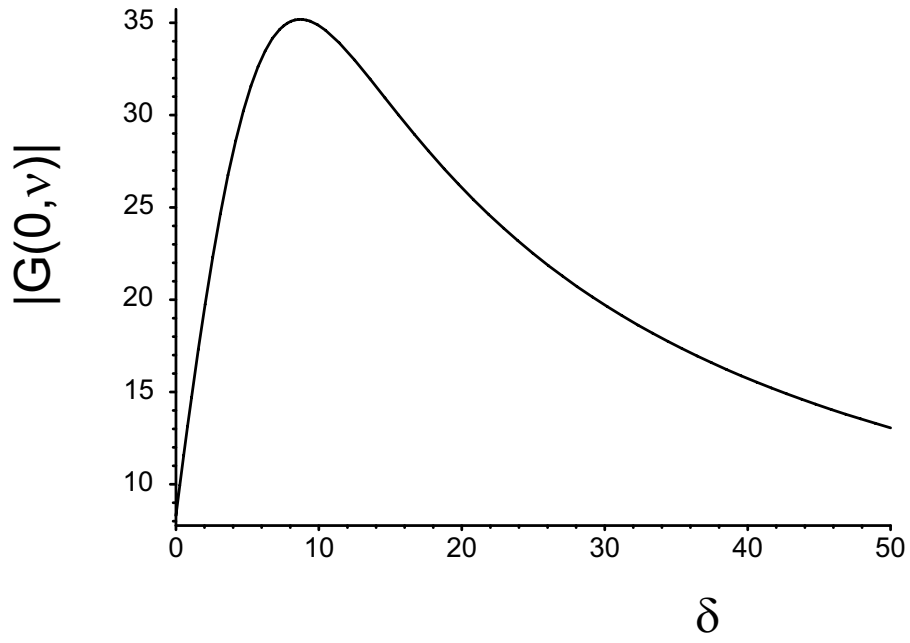

Figure 3.13: *Modulus of the $G(0,\nu)$ versus δ, at $z = 0$, $\nu = 0.15$, and using the parameters from the table (3.1).*

equivalent undulator is evaluated over the optical klystron slippage $\Delta = (N_u + N_d)\lambda$. Figure (3.14) shows the laser dimensionless intra-cavity power and the induced reltive energy spread from simulations taking the optical klystron of Super ACO and the equivalent undulator cases. We take the initial parameters of Super ACO, which are given in table (3.1), changing only the synchrotron damping time[¶] $\tau_s = 1$ ms (instead of 9 ms). The damping time is an important parameter of the ring and may modify the dynamics under detuning conditions, i.e. $\delta L \neq 0$. For comparison with experimental data from a given SRFEL it is then necessary to use the proper damping time.

First we set $\delta L = 0$. The comparison between the model using the optical klystron and the equivalent undulator are in relatively good agreement. It shows that the modelling gain for the SRFEL dynamics depends on the two requirements that we have described above, e.g. the gain at start up and the energy spread dependency.

We also compared the behavior of the laser under longitudinal detuning condition. The detuning is the delay per pass between the laser and the electron bunch. The detuning, δ_{RF}, is given in frequency deviation from the RF frequency value for which the laser pulse and the electron bunch have no delay. The result is summarized in figure (3.15), which presents the dimensionless power at saturation vs. detuning. The bars represent the amplitude of the laser intensity at equilibrium: for small bars close to the mean intensity value, the laser is cw, and for large bars, far from the mean values, the laser is pulsed. The curve exhibits 5 zones [26] where the laser operates in a cw mode or is pulsed. These zones are characteristic for SRFEL. In zones called 1 and 5 the laser is cw, as well as in the perfect tuning zone 3. In zones 2 and 4, the laser is pulsed. These different time structures for the laser beam have been observed experimentally

[¶]A smaller damping time is used here to shorten the CPU time. This does not change the main results.

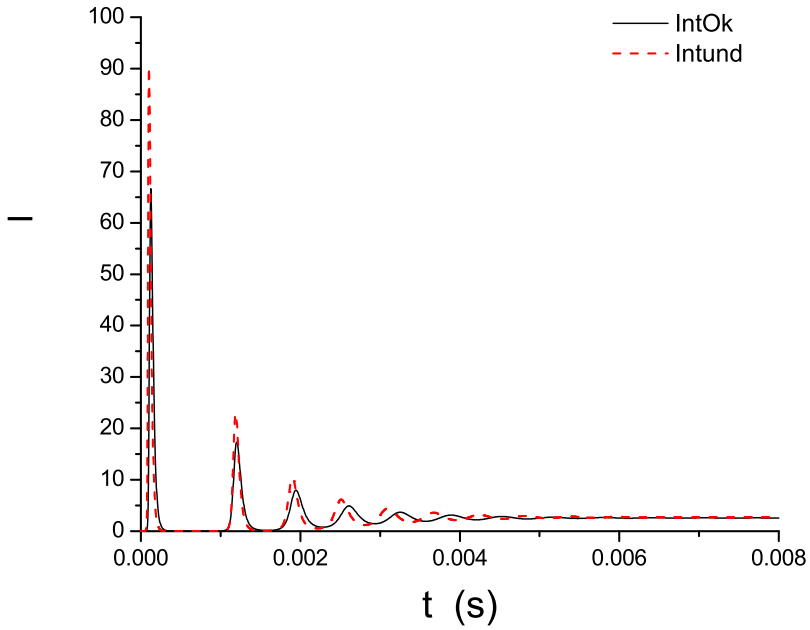

(a) dimensionless intra-cavity Power vs. time

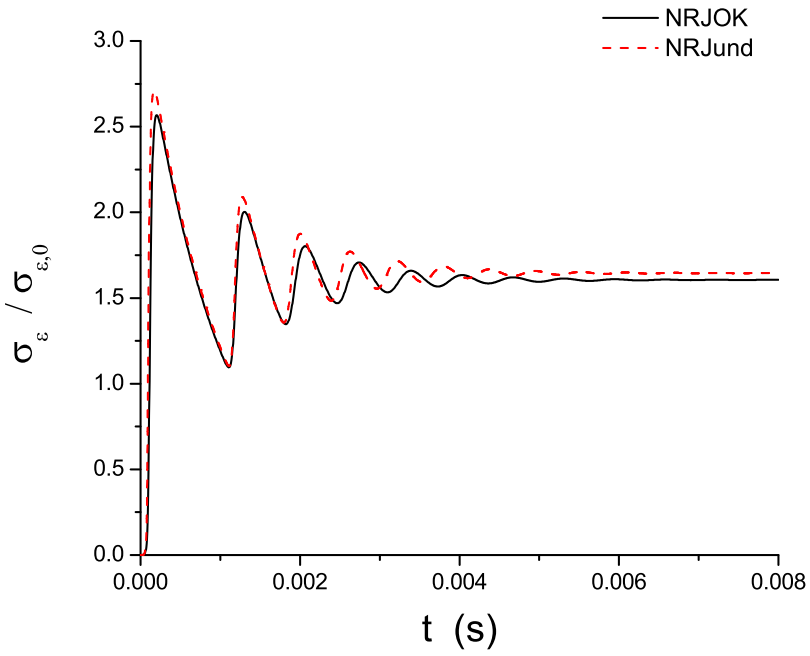

(b) Induced relative energy spread vs. time

Figure 3.14: *Comparison between the storage ring free electron laser dynamics with an optical klystron (line) and an equivalent undulator (dash). The initial parameters are in table (3.1).*

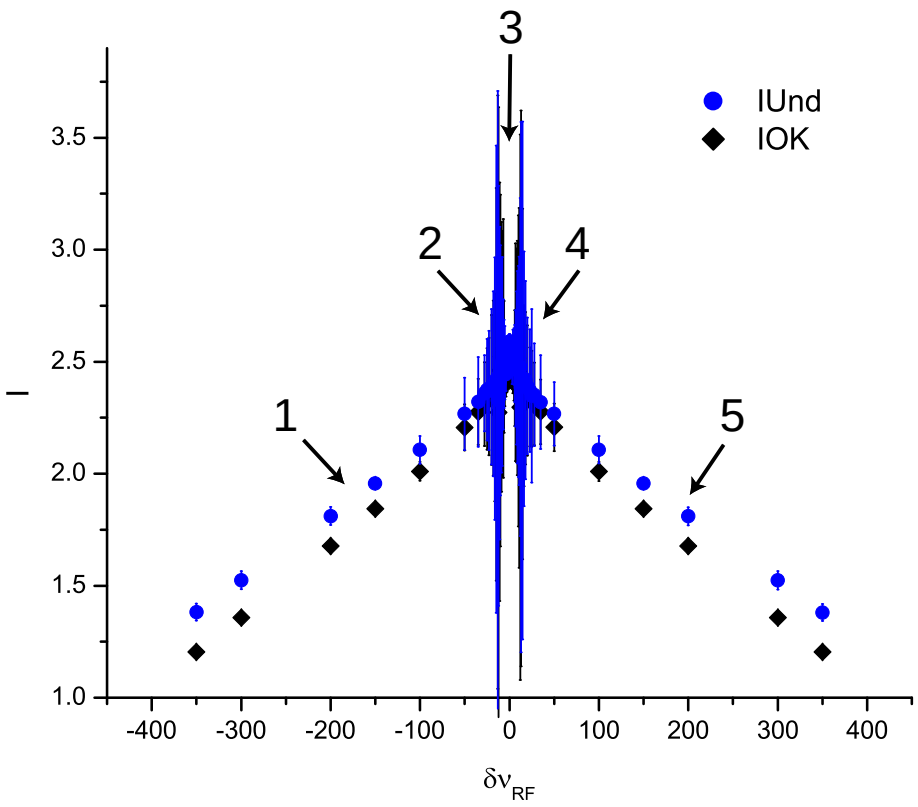

Figure 3.15: *Detuning curve in the undulator (full circle) and in the optical klystron (full diamond) cases, taking the initial values given in table (3.1). The bars represent the amplitude of the variation of the laser intensity at equilibrium: for small bars close to the mean intensity value, the laser is cw, and for large bars, far from the mean values, the laser is pulsed.*

[26]-[27]-[28]-[29]. Figure (3.16) presents the central part of the detuning curves. We find a general agreement between the two cases in the different zones where the laser is cw or pulsed. The difference appears for large detuning, with a larger detuning curve total width with the undulator than with the optical klystron, but the difference is less than 10 %.

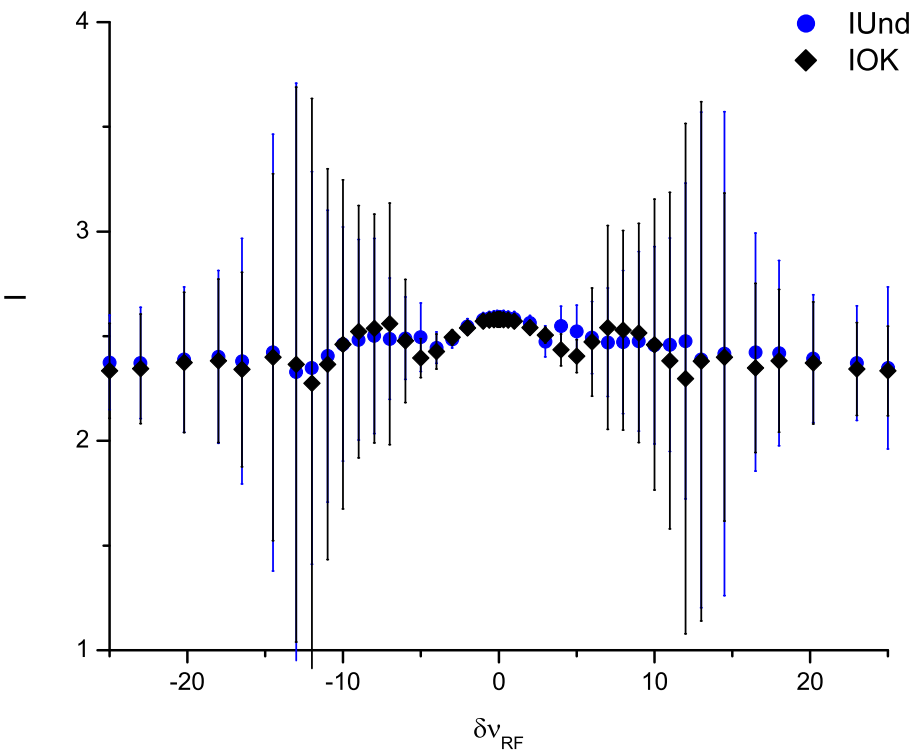

Figure 3.16: *Zoom on the central part of the detuning curve shown in figure (3.15), showing a good agreement between the two detuning curves.*

Table 3.1: *Simulation parameters.*

Small signal gain	g_0	4 %
Cavity loss	η	1 %
Total current	I (mA)	30
Bunch length	σ_b (ps)	120
frequency cut	$\omega_c = 1/\sigma_b$ (Hz)	$8.33 \cdot 10^9$
Natural energy spread	$\sigma_{\epsilon,0}$	$5.4\,10^{-4}$
Laser wavelength	λ (nm)	350
Undulator periods	N_u	10
Dispersive section number	N_d	100
Excitation MI parameter	A (s^{-1})	$4.4\,10^4$
Damping MI parameter	B (s^{-1})	$1.6\,10^4$
Normalized impedance	$\frac{Z_n}{n}$ (Ω)	4
Cavity length	L_c (m)	18
Synchrotron damping time	τ_s (ms)	1
Spectral tuning	ν	1.3 (Und.) - 0.15 (OK)
Longitudinal detuning	δL (m)	0

3.2.5 Numerical results: general behavior of the system

The numerical code given in (3.33), using the gain expression for the undulator equivalent to the optical klystron, is applied to the case of Super ACO. The numerical

results will be compared with experiments and from this typical example we try to give the general behavior of an SRFEL.
An SRFEL is a laser, so we expect the laser to start from the spontaneous emission and after a transient regime to reach saturation. In our model the start up, with the building up of the main transverse mode in not taken into acccount. We assume that the main mode is TEM_{00} and develops on a central wavelength given by $\lambda_{Las} = \lambda_r \frac{2\pi N_u - \nu}{2\pi N_u}$. We made these assumption on the basis of experiments and we do not discuss the start up of the laser. We adopt the standard procedure, assuming a minimum power at start up in the cavity.
The saturation of the laser is determined by the gain, the cavity loss, the inhomogeneous broadening and the induced energy spread, but also by the microwave instability.
To start with a simple picture of the dynamics, one can study at first a simpler system than (3.30) by replacing the first equation by the first equation for the laser intra-cavity power given in (2.51). This system is re-written here:

$$\begin{aligned}
\frac{\partial}{\partial t} I &= \frac{1}{T_0} I \left(\frac{g_0 e^{-\mu_\epsilon^2 \left(1+\sigma^2\right)}}{\sqrt{(1+\sigma^2)}} - \eta \right), \\
\frac{\partial}{\partial t} \sigma^2 &= \beta \sigma^2 - \frac{2}{\tau_s} \left(\sigma^2 - I \right), \\
\frac{\partial \beta}{\partial t} &= \beta \left[A \left(1+\sigma^2\right)^{-\frac{1}{4}} - B \left(1+\sigma^2\right)^{\frac{1}{2}} \right].
\end{aligned} \tag{3.34}$$

It has 3 singularities:

$$\left(I_{sing},\, \sigma^2_{sing},\, \beta_{sing}\right) = \begin{cases} (0,\, 0,\, 0) \\ (I_{sing},\, \sigma^2_{sing} = I_{sing},\, 0) \\ (0,\, \left(\frac{A}{B}\right)^{\frac{4}{3}} - 1,\, \frac{2}{\tau_s}) \end{cases} \tag{3.35}$$

with $I_{sing} = -1 + \left(\frac{g_0}{\eta} e^{-\frac{1}{2} W\left(2 \frac{g_0^2}{\eta^2} \mu_\epsilon^2\right)} \right)^2$.
Apart from the first singularity where there is no laser, no induced energy spread and no MI, the system exhibits two other singularities, which are an attractor and a vortice (second and third singularity respectively), as we have seen previously. Therefore the system will evolve towards the attractor or the vortice, depending on initial conditions. Moreover, it is clear that the laser is in competition with the MI: when the system evolves towards the attractor, the MI is damped with $\beta = 0$. When the system evolves towards the vortice, the laser is switched off ($I = 0$). This behavior is found also in the 1-dimensional system given by (3.30), and is illustrated with simulations for the Super ACO case, compared with measurements.
Figures (3.17), (3.18) and (3.19) illustrate the two situations. They present the results from two simulations for the case of Super ACO. Figure (3.17) presents the laser dimensionless power vs. time, in the case (a), the current $I = 100$ mA, $g_0 = 3\%$ and the microwave instability strength has been calculated using a normalized impedance $\frac{Z_n}{n} = 4\,\Omega$. The laser starts, but the microwave instability is too strong, starts and switches off the laser, as it can be seen in figures (3.17) and (3.18) showing the intra-cavity dimensionless power and the microwave instability growth vs. time respectively.

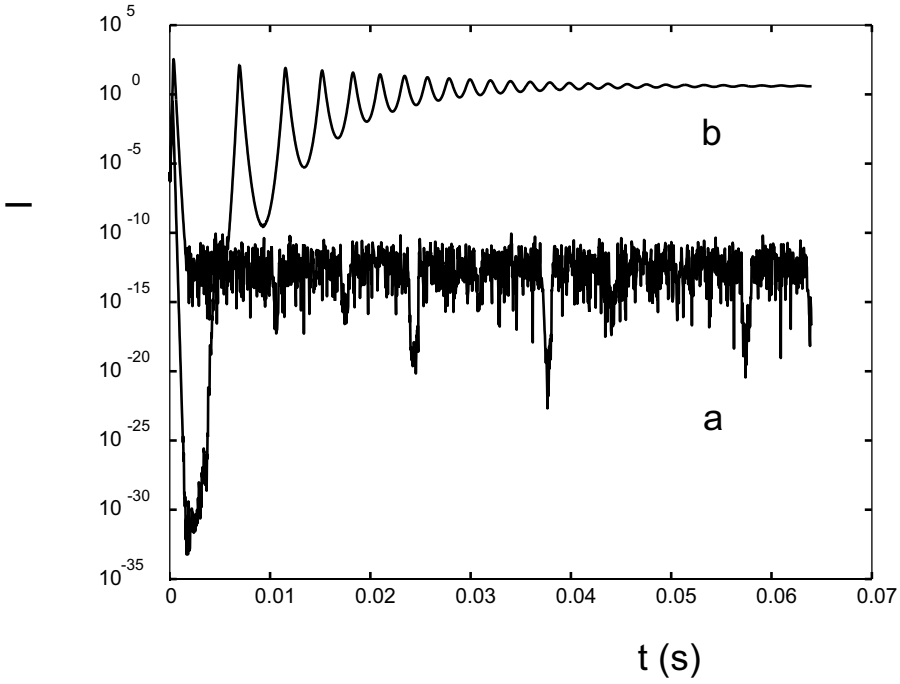

Figure 3.17: *Simulation: Laser dimensionless intra-cavity power for the case of Super ACO and the current $I = 100$ mA (a) and $I = 60$ mA (b) (see table (3.2)).*

The induced relative energy spread is then oscillating in the characteristic sawtooth regime of the microwave instability[16] as illustrated in figure (3.19).

In the case (b) $I = 60$ mA and $g_0 = 2.5\%$, the gain is smaller but the microwave instability strength is also smaller. The laser starts, reaching saturation, and the laser induced relative energy spread is high enough to switch the microwave instability off and prevents it to start again, as shown by the figures (3.17),(3.18) and (3.19). The laser characteristics in that simulation are close to the non perturbed case, i.e. simulations without MI. But the r.m.s pulse duration $\sigma_{Las} = 20$ ps, in agreement with the measurements, is longer than in the ideal numerical case without instability, $\sigma_{Las} = 7$ ps. This latter value is close to the theoretical value given by the so-called Super modes model [30], $\sigma_{Las,th} = \sqrt{\Delta}\,\sigma_b/c \approx 3$ ps. Measurements with feedback system to maintain the laser at perfect tuning showed the laser pulse duration can be shorter than 10 ps at Super ACO [31]. The Super modes model shows that the shorter pulse duration is found for a very fine detuning region around the perfect tuning, which has been observed at the DUKE FEL [32].

Considering a cavity length $L_c = 18$ m, and a beamwaist $w_0 = 350$ μm, the intra-cavity peak power obained from the simulations is $P = 5$ MW. Compared with the power measured at Super ACO, $P_{meas.} \approx 3$ MW (50 mW extracted and 20 ps pulse duration, and 10^{-4} of transmission), the simulation results give a quantitative agreement with measurements.

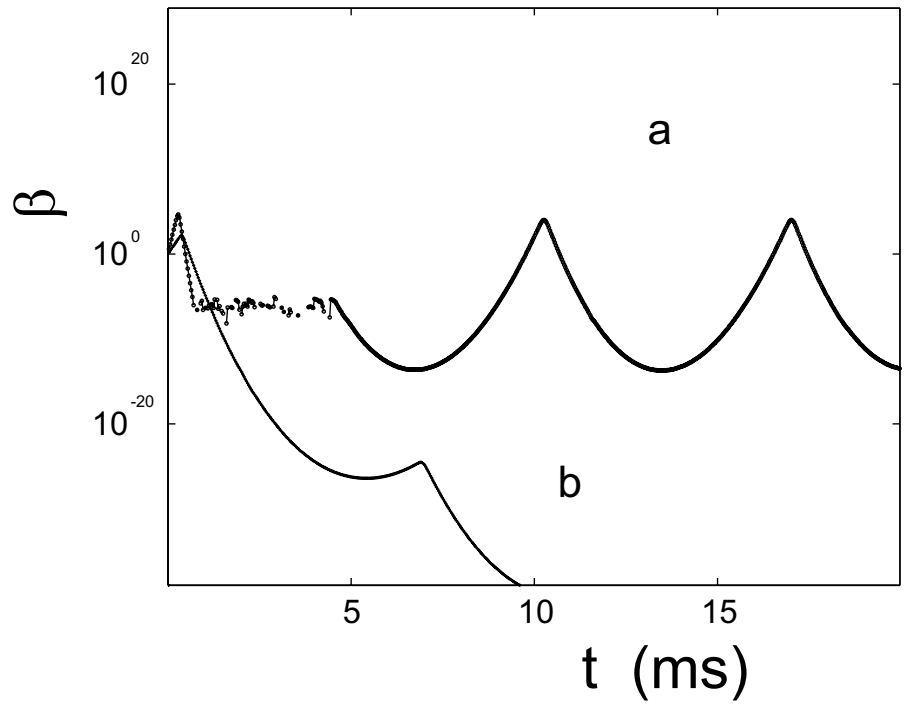

Figure 3.18: *Microwave instability growth β vs. time for the same initial parameters as in fig 3.17. In the case (a) the instability starts and switches the laser off. In the case (b) the laser starts and the instability is damped.*

3.3 Conclusion

In this chapter, we have presented some of the effects of the wakefield on the electron bunch. In the static regime, the wakefield distorts the electron bunch longitudinal distribution. In the purely resistive wake, the distribution is tilted towards the head of the bunch, inducing displacement of the bunch centroid, and a bunch lengthening. This effect may be then harmful to the laser gain. In the purely inductive wake, the distribution tends to a quadratic shape for positive momentum compaction factor, inducing also bunch lengthening; and an inverse quadratic shape for negative momentum compaction factor, which tends to reduce the bunch length. Negative momentum compaction factor operations might then be interesting for the laser, until the current is below the microwave instability threshold.
A simple model of the microwave instability has been presented. This model describes the onset, the growth and the relaxation of the instability, describing a limit-cycle characteristic of the sawtooth instability regime.
Using the simple equations, a 1-dimensional model of the storage ring free electron laser has been presented. The model is implemented in a numerical code, and the results from the code are in relatively good agreement with measurements from the Super ACO FEL: the laser characteristics and the laser induced energy spread from the code are in agreement with the measurements. In addition the competition between the laser and the beam microwave instability is described. The parameters A and B, that lead the instability dynamics, can be used to determine the threshold of the laser - instability competition.

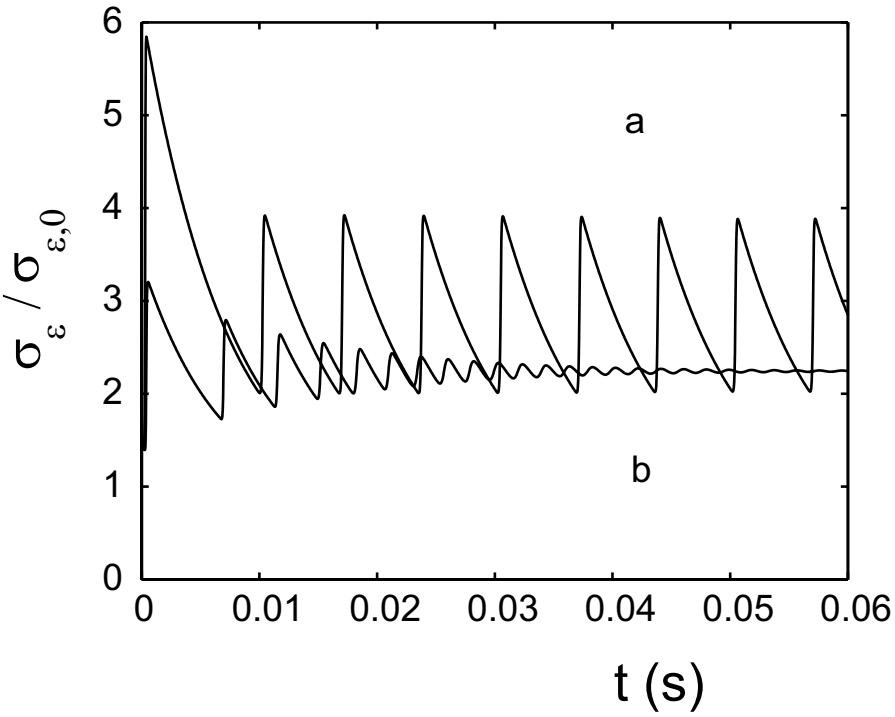

Figure 3.19: *Relative energy spread vs. time for the same initial parameters as in fig 3.17. In the case (a) the instability starts and induces a sawtooth regime. In the case (b) the laser starts and the energy spread reaches a new equilibrium depending on the intra-cavity power.*

Table 3.2: *Simulation parameters for Super ACO FEL.*

		(a)	(b)
Total current	I_0 (mA)	100	60
Small signal gain	g_0 %	3.0	2.5
Cavity loss	η %	1	
Bunch length	σ_b (ps)	120	100
Natural energy spread	$\sigma_{\epsilon,0}$	$5.4\,10^{-4}$	
Laser wavelength	λ (nm)	350	
Undulator periods	N_u	10	
Dispersive section number	N_d	100	
Excitation MI parameter	A (s^{-1})	$4.4\,10^4$	$5.7\,10^4$
Damping MI parameter	B (s^{-1})	$1.6\,10^4$	
Normalized impedance	$\frac{Z_n}{n}$ (Ω)	4	
Cavity length	L_c (m)	18	
Synchrotron damping time	τ_s (ms)	9	
Spectral tuning	ν	1.3	
Longitudinal detuning	δL	0	

References

[1] G. Dattoli and L. Mezi. The storage-ring FOKKER-PLANCK equation: inclusion of the free electron laser amplifier contributions. *Nuclear Instruments and Methods in Physics Research A*, 436:415, November 1999.

[2] J. Haissinski. *Nuovo Cimento B*, 18:72, 1973.

[3] A. Hofmann. *Beam instabilities*, volume 95-06 of *CAS: 5th Advanced Accelerator Physics Course*, chapter 14. CERN Accelerator School, 1995.

[4] K. Bane. Bunch lengthening in the SLC damping ring. SLAC-PUB Report 5177, SLAC, 1990.

[5] C.A. Thomas, J.I.M. Botman, R. Bartolini, G. Dattoli, L. Mezi, and M. Migliorati. An analytical solution for the Haissinski equation with purely inductive wake fields. *Europhysics Letters*, 60(1):66, October 2002.

[6] A. W. Chao. *Physics of collective beam instabilities in high energy accelerators.* Wiley-Interscience, 1993.

[7] E. S. Kim and K. Hirata. KEK Report 95-5, KEK, 1995.

[8] Y. Shobuda and K. Hirata. Longitudinal instability for a purely inductive wake function. *Phys. Rev. E*, 60:2414, August 1999.

[9] F. Ciocci, G. Dattoli, A. Torre, and A. Renieri. *Insertion devices for synchrotron radiation and free electron laser*, volume 6 of *Synchrotron Radiation Techniques and Applications.* World Scientific, June 2000.

[10] R. M. Corless, G. H. Gonnet, D. E. G. Hare, and D. J. Jeffrey. Lambert's W Function in Maple. *Maple Technical Newsletter*, 9:12, 1993.

[11] S. R. Valluri, D. J. Jeffrey, and R. M. Corless. Some applications of the Lambert W function to physics. *Canadian J. Physics*, 78:823, 2000.

[12] R. M. Corless, G. H. Gonnet, D. E. G. Hare, D. J. Jeffrey, and D.E. Knuth. On the Lambert W Function. *Advances in Computational Mathematics*, 5:329, 1996.

[13] Y. Shobuda and K. Hirata. The existence of a static solution for the Haissinski equation with purely inductive wake force. In *Proc. Particle Acc. Conf.*, volume 62, page 165, 1999.

[14] K. Oide and K. Yokoya. KEK Report 90-10, National Lab. for High Energy Physics, Tsukuba, Japan, 1990. unpublished.

[15] G. V. Stupakov, B. N. Breizman, and M. S. Pekker. Nonlinear dynamics of microwave instability in accelerators. *Phys. Rev. E*, 55:5976–5984, May 1997.

[16] M. Migliorati, L. Palumbo, G. Dattoli, and L. Mezi. Saw-tooth instability in storage rings: simulations and dynamical model. *Nuclear Instruments and Methods in Physics Research A*, 437:134, November 1999.

[17] G. Dattoli, A. Renieri, and G. Voykov. Storage-ring free-electron-laser amplifiers and the microwave instability. *Physical Review E*, 55:2056, February 1997.

[18] R. Bartolini, G. Dattoli, L. Mezi, A. Renieri, M. Migliorati, M. E. Couprie, G. de Ninno, and R. Roux. Suppression of the Sawtooth Instability in a Storage Ring by Free-Electron Laser: An Example of Nonlinear Stabilization by Noise. *Physical Review Letters*, 87:134801, September 2001.

[19] D. Boussard. internal report 75-2, CERN, 1975.

[20] G. Dattoli, L. Mezi, M. Migliorati, and L. Palumbo. Storage ring free-electron laser and microwave-type instabilities. *Nuovo Cimento B Serie*, 115:639, June 2000.

[21] G. Dattoli, T. Hermsen, A. Renieri, A. Torre, and J. C. Gallardo. Lethargy of laser oscillations and supermodes in free-electron lasers. *Physical Review A*, 37:4326, June 1988.

[22] G. Dattoli, L. Mezi, and L. Bucci. Pulse propagation and optical-klystron free-electron-laser devices. *Physical Review E*, 61:7052–7056, June 2000.

[23] C. A. Thomas, J. I. M. Botman, G. D. Ninno, M. E. Couprie, L. Mezi, and G. Dattoli. SRFEL dynamics investigated with a 1-D numerical code. *Nuclear Instruments and Methods in Physics Research A*, 483:181–185, May 2002.

[24] P. Elleaume. The Optical klystron. *J. de Phys. (Paris)*, 44(C1):353, 1983.

[25] G. Dattoli and P.L. Ottaviani. Gain parametrization formulas in FEL optical klystron configuration. *IEEE Journal Quantum Electronics*, 35:27, January 1999.

[26] M. E. Couprie, V. Litvinienko, D. Garzella, A. Delboulbé, M. Velghe, and M. Billardon. Dynamical study of the Super-ACO free electron laser with the dissector. *Nuclear Instruments and Methods in Physics Research A*, 331:37, July 1993.

[27] H. Hama, J. Yamazaki, T. Kinoshita, K. Kimura, and G. Isoyama. Observation of micro-macro temporal structure and saturation mechanism on the UVSOR free electron laser. *Nuclear Instruments and Methods in Physics Research A*, 358:365–368, February 1995.

[28] V. N. Litvinenko, S. H. Park, I. V. Pinayev, and Y. Wu. Time structure of the OK-4/Duke storage ring FEL. *Nuclear Instruments and Methods in Physics Research A*, 475:240–246, December 2001.

[29] G. De Ninno, M. Danailov, B. Diviacco, M. Marsi, and M. Trovó. Laser-electron beam dynamics of the european free electron laser at ELETTRA. In *Proc. of EPAC 2002, (Paris)*, page 799, June 2002.

[30] G. Dattoli and A. Renieri. Storage ring operation of the free-electron laser - The oscillator. *Nuovo Cimento B*, 59:1, September 1980.

[31] Roux R. *Dynamique et condition de stabilité du laser à électron libres de Super-ACO. Fonctionnement avec une cavité simple ou double.* PhD thesis, Université Paris Sud, Orsay (France), January 1999.

[32] V. N. Litvinenko, S. H. Park, I. V. Pinayev, Y. Wu, A. Lumpkin, and B. Yang. Fourier limited micro-pulses in the OK-4/Duke storage ring FEL. *Nuclear Instruments and Methods in Physics Research A*, 475:234–239, December 2001.

Chapter 4

Dynamics of the SRFEL: experimental aspects

C. A. Thomas*†, J.I.M. Botman
Applied Physics Department, Technische Universiteit Eindhoven, The Netherlands
C. Bruni, G. Orlandi, D. Garzella, G. De Ninno‡, R. Roux§, D. Nutarelli¶, M. E. Couprie
LURE, Université Paris Sud, France
and
DSM/DRECAM/SPAM, CEA de Saclay, Gif sur Yvette, France

4.1 Introduction

Free Electron Lasers (FELs) are coherent tunable and powerful sources, covering the wavelength range from *IR* to *VUV*. Their principle lies in the interaction of light with a relativistic electron beam that travels through the permanent sinusoidal magnetic field from an undulator [1]. While traversing the undulator the electrons bend and emit synchrotron radiation: the spontaneous emission of the FEL. The interaction, at each passage, of a light pulse with an electron bunch leads to laser gain to the detriment of the electron kinetic energy. In a storage ring free electron laser, the electrons* are re-circulated and interact, at each passage in the laser optical cavity, with the light pulse. The interaction leads to the amplification of the light pulse, inducing energy spread to the electron beam. The degradation of the energy spread of the re-circulated electron beam is a peculiarity of the storage ring free electron laser [2]. As the gain depends on the energy spread, the enhancement of energy spread of the electron beam is responsible for the storage ring free electron laser saturation.
The first FEL operation was demonstrated in the *IR* on a linear accelerator in 1977 [3].

*This chapter has been submitted as a paper in the present form to Physical Review E under the title: "Storage Ring Free Electron Laser dynamics in presence of an auxiliary harmonic Radio Frequency cavity". There is some overlap with chapters 3 and 5.

†also at *LURE*

‡at the present address: *Sincrotrone Trieste, Italy*

§at the present address: *LAL, Université Paris Sud, France*

¶at the present address: *Laboratoire Aimé Cotton, Université Paris Sud, France*

*We often use the term electrons even for the positron storage ring.

In 1983 the first lasing on a storage ring was obtained at Anneau de Collision d'Orsay (collision ring ACO), in the visible wavelength range [4]. Nowadays, storage ring free electron lasers (SRFEL) in rings like Super-ACO [5], ELETTRA [6], DELTA [7], DUKE [8], UVSOR [9], NIJI-IV [10] are operating on a regular basis in the *UV* and *VUV* range. Those *UV*-*VUV* SRFELs provide a unique tool for performing time-resolved and/or frequency resolved experiments [11]. Furthermore, the natural synchronization of the FEL pulse with the synchrotron radiation extends the possibilities of the laser to two-color experiments using the complementary features of UV tunable FELs and the broad-band spectral range of synchrotron radiation sources [12]. Nevertheless, stringent requirements on the laser stability are needed in order to perform these experiments properly. The laser dynamics is coupled with the electron beam dynamics, consequently a stable laser requires a stable beam.
An auxiliary RF cavity in the ring, operating at a higher harmonic of the first one, is normally used to lengthen the bunch and reduce or damp longitudinal instabilities [13]. At Super-ACO, like previously at VEPP 3 [14] and UVSOR [15], the harmonic cavity is functioning in the bunch shortening mode during FEL operation, in order to enhance the laser gain, which allows to extract more power for user applications. But when this cavity is used, this may also induce instabilities in the beam due to an enhancement of the intensity of the wakefield generated by the electron beam and reflected by its environment. Therefore, the dynamics of the laser will be modified and consequently the laser characteristics will be different.
For the design and optimization of SRFELs, 3-dimensional numerical codes have been developed [16]-[17]-[18]. But still instabilities such as the microwave instability [19] and coherent synchrotron oscillations [20], and the interplay between the beam instability and the FEL needed to be taken into account in order to understand the dynamics of SRFELs and possibly to control it. We developed a 1-dimensional numerical code [21] to investigate the dynamics of the SRFEL in the presence of the microwave instability. The code has provided qualitative as well as quantitative results in comparison with measurements performed at the Super ACO and ELETTRA FELs [22]. The code showed the competition between the FEL and the instabilities. From that competition several situations may arise: first the laser damps all the instabilities and the laser becomes relatively stable; second, the instabilities switch the FEL off and perturb the beam; finally the FEL may co-exist with the beam instabilities, providing a less stable FEL with longitudinal jitter and intensity fluctuations, as well as a perturbed electron beam.
In this chapter, we present the beam dynamics induced by the auxiliary RF cavity at Super-ACO. Subsequently we describe the longitudinal bunch characteristics as a function of the harmonic cavity parameters, the various instabilities observed and their sources. Then we analyze the properties and the dynamics of the FEL. Finally we discuss the interplay between the laser and the beam.

4.2 Characterization of the beam

The 5^{th} harmonic cavity used for bunch length shortening induces various effects which are different from the situation in which this cavity is not present. In particular, various instabilities show up, which can not immediately be explained by theoretical

models that are successful for the case in which the harmonic cavity is absent. In this section we first briefly describe the measurement equipment at Super ACO used for the determination of bunch length and energy spread. Then, we present measurements as a function of beam current and of harmonic cavity voltage. We ascribe observed phenomena and instabilities to effects such as the microwave instability and the potential well distortion. This section only describes the bunch characteristics when the FEL is off. The combined features of the FEL and electron beam in the storage ring are the subject of the subsequent section.

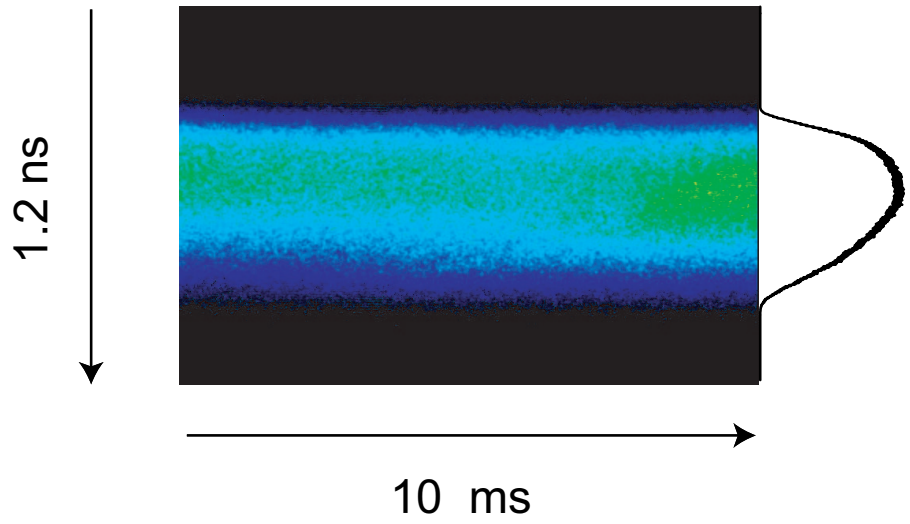

Figure 4.1: *Image of the bunch longitudinal distribution obtained with Hamamatsu DSSC at the total current $I = 41$ mA. The moment method, applied on the distribution shown on the right side of the image, give the following values: the bunch length $\sigma_\tau = 140 \pm 5$ (ps), the kurtosis is $Kurt = -0.84$ and the skewness is $Skew = -0.16$. The kurtosis is a measure of how outlier-prone a distribution is from the normal distribution. The skewness is a measure of the asymmetry of the distribution around its mean value. One observes on the profile an asymmetry with negative skewness and a flatness compared to a Gaussian distribution (negative kurtosis).*

4.2.1 Measurement apparatus for the study of the longitudinal beam dynamics

The longitudinal beam parameters are measured at Super-ACO respectively with a double sweep streak camera DSSC (Hamamatsu) for describing the longitudinal bunch distribution and a CCD camera for the bunch energy distribution. The DSSC is illuminated with the synchrotron radiation from a bending magnet (SA5), where the synchrotron light pulse has the longitudinal profile of the electron bunches. A cut of a DSSC image [23] (fig. (4.1)), taken at a given beam current, along the fast sweep (vertical) gives the longitudinal bunch distribution, and the time evolution of the longitudinal distribution can be followed along the slow time scale (horizontal). The moments of the distribution provide further information: on each image one can extract the values vs. time of the bunch centroid (moment of first order), the r.m.s bunch

length (moment of second order), and the skewness and kurtosis (moment of 3^{rd} and 4^{th} order respectively).
The energy distribution and its second order moment, the energy spread (σ_ϵ), is obtained from the measurement, on a CCD image, of the horizontal beam dimension in a dispersive section of the ring [24]. The following relation is used:

$$\sigma_x^2 = \epsilon_x \beta_x + (\eta_x \sigma_\epsilon)^2, \tag{4.1}$$

where σ_x is the r.m.s horizontal beam size, ϵ_x, β_x and η_x are respectively the horizontal beam emittance, the beta function and the dispersion function at the measurement point. We note that we always use a Gaussian fit for extracting the values of the energy spread. The parameters of the Super ACO FEL can be seen in table (4.1).

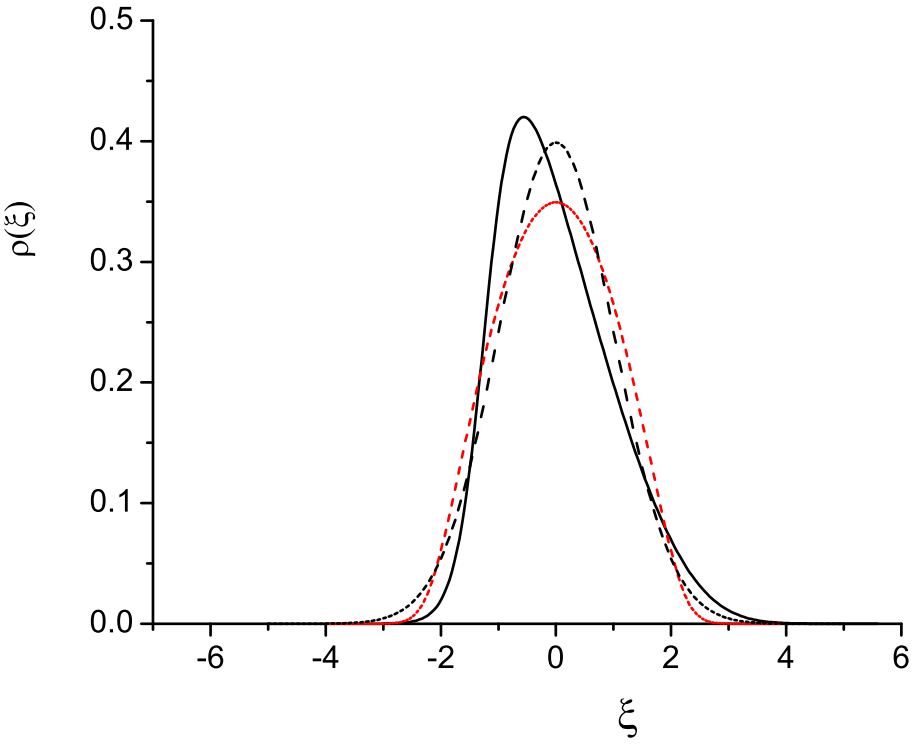

Figure 4.2: *Bunch longitudinal distribution, $\rho(\xi)$, from the Haissinski equation, in the pure resistive (line) and inductive cases (small dash), compared to the Gaussian distribution (dash). The skewness is 0, -0.5, 0 and the kurtosis is 0, 0.05, -0.68 for the Gaussian, the resistive and the inductive case respectively.*

4.2.2 Longitudinal beam properties

From a theoretical point of view, the bunch longitudinal phase space distribution (using as axes the longitudinal position and energy deviation with respect to a reference particle) results from several contributions [25]-[26]-[27]. The natural distribution is Gaussian in energy and position, with a correlation between the r.m.s values of the energy and position distributions. The natural electron bunch energy spread (r.m.s value of the energy distribution), due to quantum excitation radiation, induces a minimum bunch length (r.m.s value of the longitudinal bunch distribution), which depends

on the storage ring characteristics. Increasing the current induces collective effects in the bunch. These collective effects result from the wakefield generated by the relativistic electrons, and reflected by the vacuum chamber. The wakefield interacts with the electrons of the same bunch or with the next coming electron bunch, leading to a perturbation of the electron bunch. The perturbation may be damped and may displace the bunch equilibrium. It may result in a distortion of the longitudinal distribution and in bunch lengthening compared to the natural bunch length. If the perturbation is not damped, the phase space distribution is not static, and may not be Gaussian. The result is an increase of the average r.m.s values of the energy distribution as well as the longitudinal distribution.

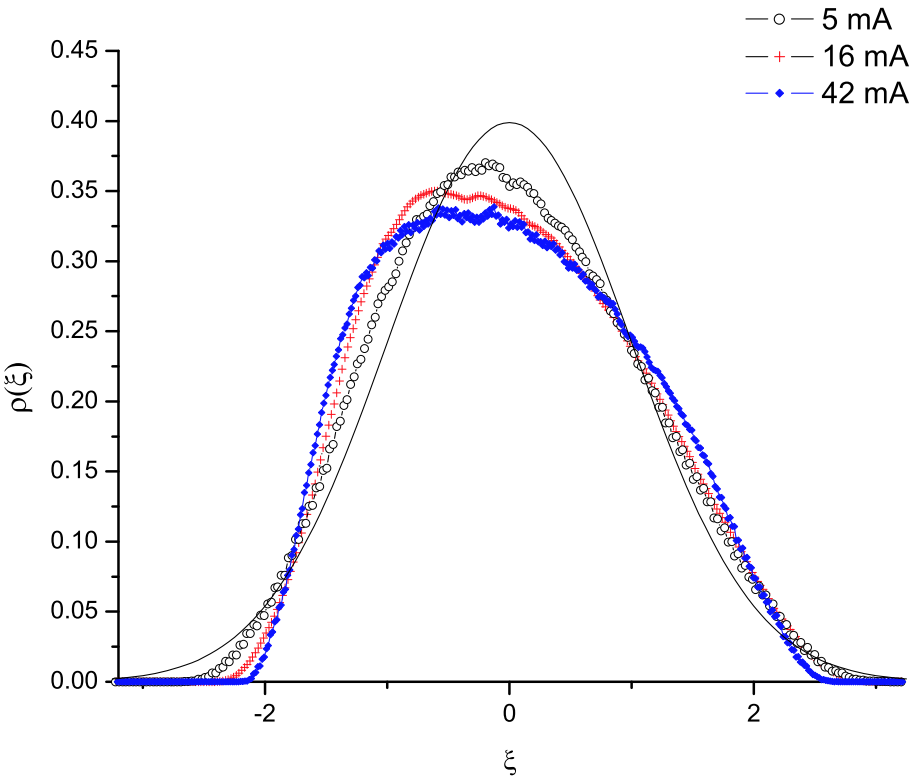

Figure 4.3: *Bunch longitudinal distribution of Super ACO, $\rho(\xi)$, measured with the DSSC camera, for several values of the current at $V_{hRF} = 0$ kV, and compared to the Gaussian distribution (line). The longitudinal coordinate, ξ, is centered, so that the first order moment of the distribution is at $\xi = 0$, and reduced, so that the second order moment is equal to 1. The skewness of the distribution is -0.23, -0.15, -0.18 and the kurtosis is -0.68, -0.55, -0.85, for I=5, 16, 42 mA respectively.*

In the case of the static bunch, the longitudinal phase space distribution is described by a Gaussian energy distribution, e.g. as observed on the CCD camera images, and the longitudinal distribution is given by the Haissinski equation [26]. From this equation, and taking into account the impedance of the ring, the solution is generally not Gaussian, but reduces to a Gaussian distribution in the low current region [26]-[27]. For some particular impedance cases, such as purely resistive and purely inductive wakes, analytical solutions exist [27]-[28]. Generally the impedance of a storage ring

has an inductive and/or a resistive nature [27]-[28]-[29]-[30]. The resulting distribution is tilted towards the head of the bunch, due to the resistive part of the impedance, and the distribution shape is blown up due to the inductive part. The distribution in the latter case can be described with the Lambert W function, $W(z)$, as [28]:

$$\begin{aligned} W(A\Lambda \exp(-\frac{\xi^2}{2})) = \quad & 1 + \frac{1}{2}(-\xi^2/2 + \ln\frac{A\Lambda}{e}) \\ & + \frac{1}{16}(-\xi^2/2 + \ln\frac{A\Lambda}{e})^2 \\ & - \frac{1}{192}(-\xi^2/2 + \ln\frac{A\Lambda}{e})^3 \\ & - \frac{1}{3072}(-\xi^2/2 + \ln\frac{A\Lambda}{e})^4 \\ & + \frac{13}{61440}(-\xi^2/2 + \ln\frac{A\Lambda}{e})^5 \\ & + O((-\xi^2/2 + \ln\frac{A\Lambda}{e})^6). \end{aligned} \tag{4.2}$$

(4.3)

where A is a normalization factor and Λ is a dimensionless positive number given by the storage ring parameters and the inductive impedance (see chapter 3).
An example of these two distributions compared to the Gaussian distribution is given in figure (4.2), where the solution of the Haissinski equation has been plotted for typical situations as e.g. occurring at Super ACO. Here we give the longitudinal distribution in the longitudinal reduced coordinate ξ (i.e. the r.m.s value of the distribution is equal to 1), with respect to the center of the bunch.
In the passive cavity case ($V_{hRF} = 0$ kV, where V_{hRF} is the voltage of the harmonic cavity and with h the harmonic number) of Super ACO (figure 4.3) the measured distribution combines the effect from the resistive and inductive impedance. Indeed, the distribution at low current is observed to be Gaussian. For increasing currents, the distortion becomes more pronounced both regarding the tilting effect and regarding the 'parabolic' like shape given by the expression (4.2).
For increasing harmonic cavity voltage, the distortion becomes also more pronounced. This can be observed in figure (4.4), which shows the distribution for several currents at $V_{hRF} = 90$ kV. These effects show the complex nature of the wake induced by the auxiliary cavity.
The r.m.s values of the longitudinal and energy distributions are respectively the bunch length and the energy spread. Figure (4.5) presents the bunch length and the energy spread as function of the total current. We observe, apart from the near current, two characteristic zones: the high current zone, where collective effects manifest themselves with the bunch length increasing proportionally to the energy spread, and an intermediate current zone from low current to an anti-threshold current, I_s where the behavior of the beam is different from that at high current operation.
At near zero current, the collective effects are negligible which is shown by the measurements of the energy spread and bunch length at near zero current. The values of energy spread and bunch length correspond to the natural ones [25]: $\sigma_{\epsilon,0} = 5.4\,10^{-4}$ and the bunch length depends on the voltages of the RF cavities, V_{RF} and V_{hRF}, the momentum compaction factor, α_c, and the natural energy spread:

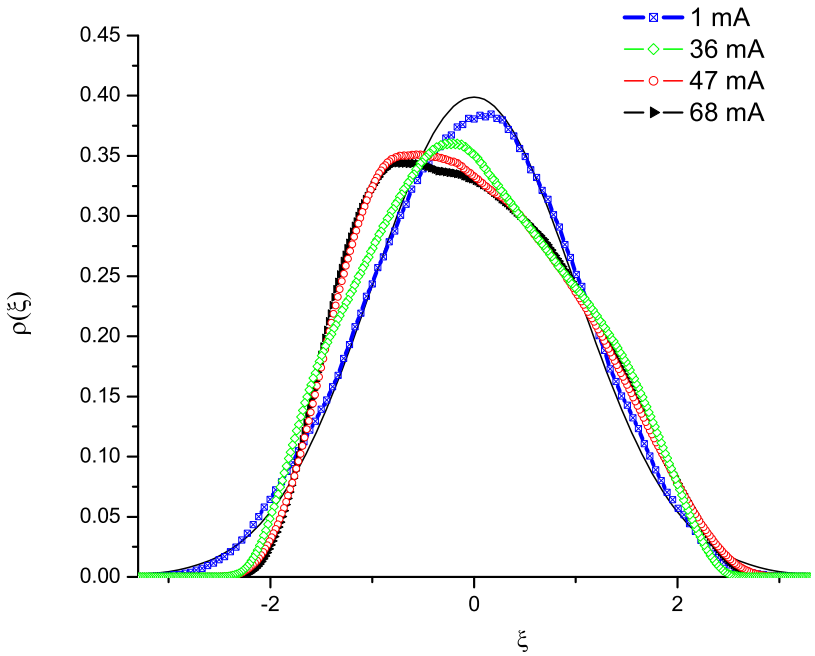

Figure 4.4: *Bunch longitudinal distribution measured with the DSSC camera, for several values of the current at V_{hRF} = 90 kV, and compared with the Gaussian distribution (line). The skewness of the distribution is -0.4, -0.11, -1, -0.24 and the kurtosis is -0.4, -0.75, -0.67, -0.73, for I= 1, 36, 47, 68 mA respectively.*

$$\sigma_\tau(0) = \frac{\alpha_c}{\Omega_s(V_{hRF})}\sigma_{\epsilon,0} \tag{4.4}$$

$$\Omega_s(V_{hRF}) = \Omega_{s,0}\sqrt{1 + h\frac{V_{hRF}}{V_{RF}}}, \tag{4.5}$$

with $\Omega_{s,0} = \left(\frac{\alpha_c V_{RF}\omega_{RF}}{T_0 E_0}\right)^{\frac{1}{2}}$ the synchrotron angular frequency with the main RF cavity alone, T_0 is the revolution period, E_0 is the electron energy and ω_{RF} the angular RF frequency.

Figure (4.6) shows the measurements at near zero current of the bunch length and the relative energy spread for several values of V_{hRF}, which are within 95 % agreement with the theoretical values given by expression (4.4). The one-particle analysis [25] holds when the current density is very low.

In normal operation at Super ACO the current decreases from the injected value to nearly 0. At high current, and down to an anti-threshold current, I_s, which is a function of V_{hRF}, the collective effects manifest themselves by bunch lengthening proportional to energy spreading. The lengthening is proportional to the current I^α, which is a signature of the microwave instability[31]-[32]-[33]. A fit of the curves of bunch length and energy spread vs. current in the considered current region gives the value $\alpha \approx 0.8$.

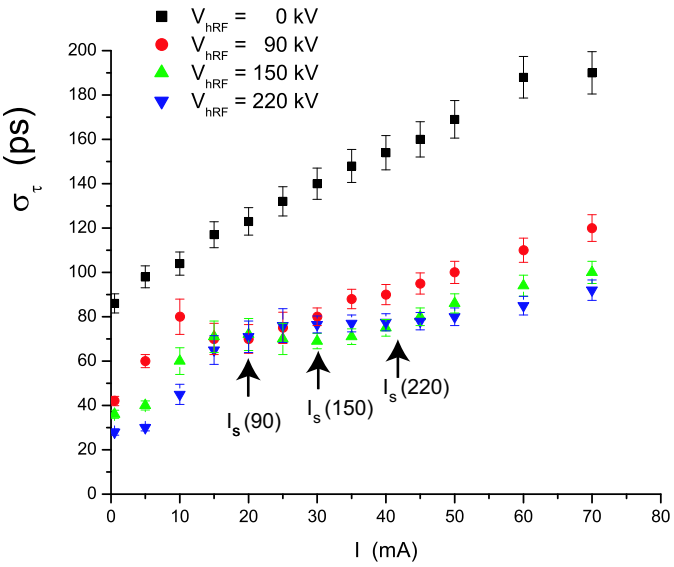

(a) Bunch length

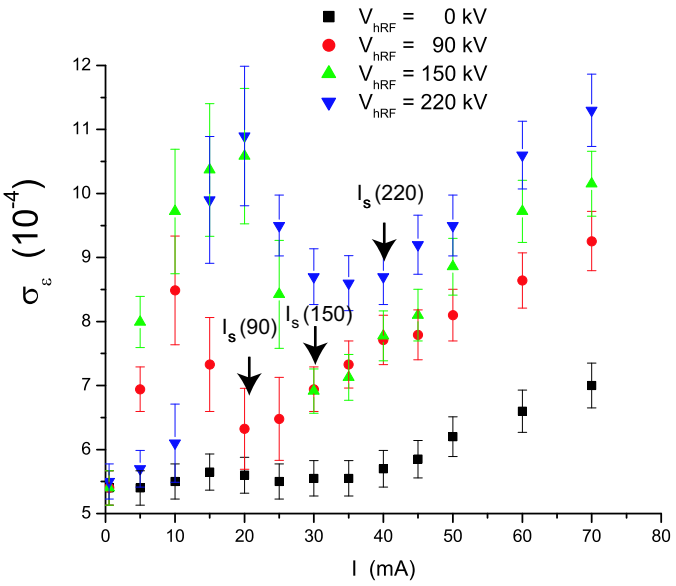

(b) Energy spread

Figure 4.5: *Bunch length and energy spread vs. current, measured at Super ACO, for several values of* V_{hRF}.

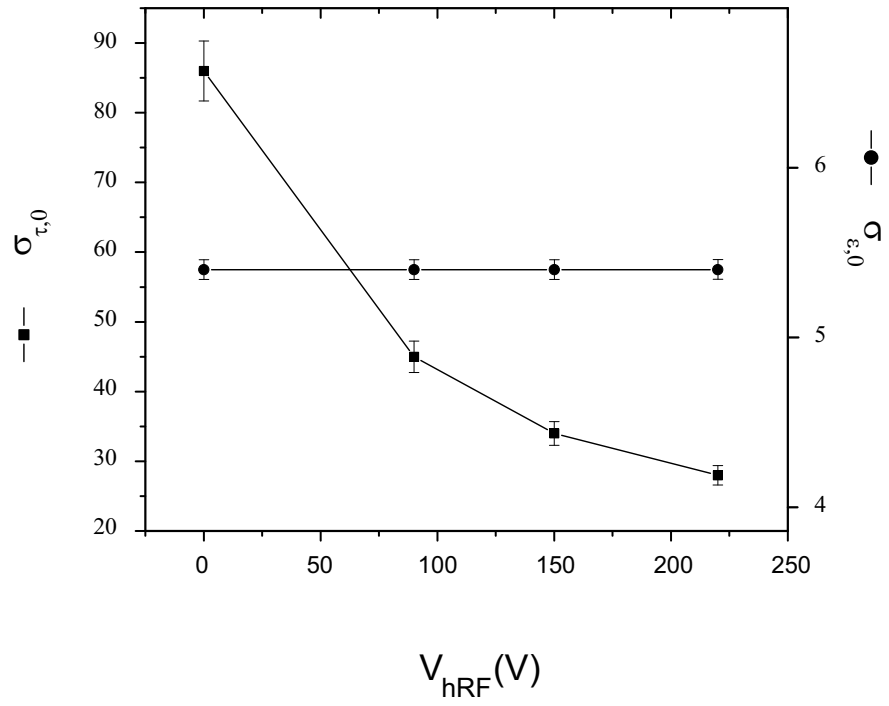

Figure 4.6: *Relative energy spread (points) and bunch length (squares), measured at Super ACO, at near zero current (I= 0.5 mA) for several values of the harmonic cavity voltage.*

The microwave instability is the instability resulting from the interaction of the electrons with that part of the wakefield of which the wavelength is in the micrometer range. The current threshold where the microwave instability sets on has been given by Boussard [31] and depends on the normalized ring impedance $\frac{Z_n}{n}$ and the synchrotron tune, ν_s, as follow:

$$I_{th} = \frac{\sqrt{2\,\pi}\,\alpha_c^2 \sigma_{\epsilon,0}^3 (E_0/e)}{\nu_s \frac{Z_n}{n}}, \tag{4.6}$$

where e is the elementary charge. Considering an impedance $\frac{Z_n}{n} \approx 5\Omega$ the Boussard threshold, at $V_{hRF} = 90$ kV, is $I_{th} \approx 2.5$ mA. However the curves in figure (4.5) show that the microwave instability at Super ACO is clearly present at above 40 to 50 mA, at values higher than equation (4.6) predicts. In between different phenomena occur: instabilities of unknown type appear above 10 mA and disappears above an anti-threshold I_s, where the microwave instability shows up, as discussed above.
In figure (4.5) the anti-threshold current, I_s, which is given by the curvature change, from high to low current, of both bunch length and energy spread curves, is approximatively equal to 40 mA for $V_{hRF} = 220$ kV, 30 mA for 150 kV, 20 mA for 90 kV. The anti-threshold I_s increases with increasing V_{hRF}.

Another contribution to bunch lengthening is by the so-called potential well distortion (PWD): the wakefield distorts the RF cavity field which subsequently causes bunch lengthening. This effect of the PWD is clearly seen for the passive auxiliary cavity ($V_{hRF} = 0$ V) in figures (4.5(a)) and (4.5(b)), where the bunch lengthens while the

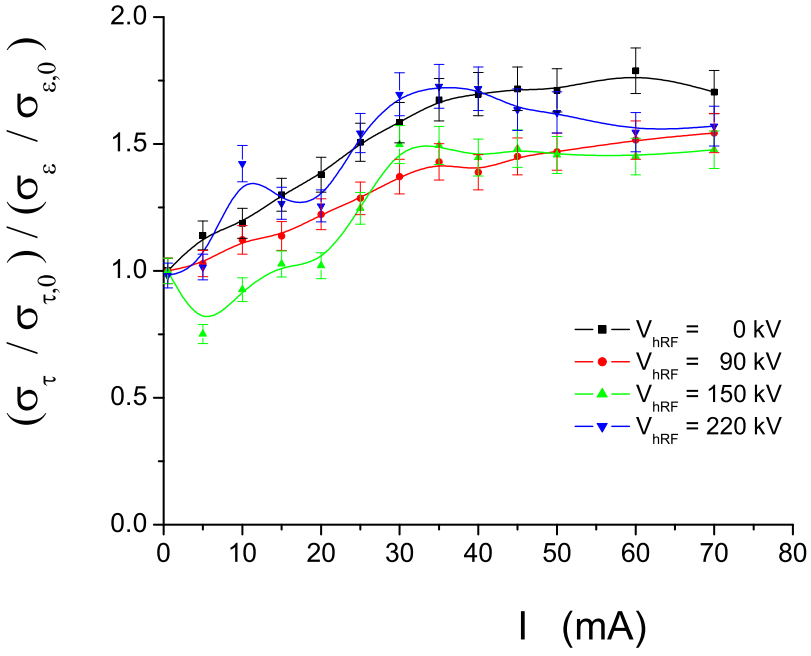

Figure 4.7: *Ratio of the normalized bunch length with the normalized energy spread vs. average current for the same values of the RF harmonic cavity voltage, V_{hRF}, as in fig 4.5.*

energy spread stays constant, until the microwave instability sets in at about 35 mA. The ratio $\frac{\sigma_\tau/\sigma_{\tau,0}}{\sigma_\epsilon/\sigma_{\epsilon,0}}$ is then expected to increase from 1 at near zero current, as the PWD increases with the current. Above the Boussard threshold, the microwave instability manifests itself, and the bunch lengthening becomes proportional to the energy spread. As a result, the PWD effect is negligible at high current and the ratio $\frac{\sigma_\tau/\sigma_{\tau,0}}{\sigma_\epsilon/\sigma_{\epsilon,0}}$ approaches a constant different from 1 (figure (4.7)). However figure (4.7) shows a similar behavior also for any voltage of the harmonic cavity. This indicates that the PWD is always present in the current region from 0 to 40 mA. Still, the PWD is not the only extra effect which occurs in this particular current region. As will be shown, coherent longitudinal oscillations also play an important role.

For currents lower than the anti-threshold the wakefield induces an instability, which depends on the current and on the voltage V_{hRF}. The bunch undergoing instabilities in that current region, has a non-static distribution. The first and higher order moments of the distribution generally oscillate at frequencies close to the synchrotron frequency and/or at a higher harmonics. This means that there is a coherent longitudinal oscillation of the bunch, or even that part of the bunch is divided into a few (1,2,3, etc.) smaller bunches which have coherent oscillations at the synchrotron frequency or at higher harmonics of the synchrotron frequency. The sub-bunches need not oscillate in phase with respect to each other. A dipolar oscillation means that the first order moment oscillates at the synchrotron frequency, f_s. For quadripolar oscillation the second order moment oscillates at the second harmonic, $2\,f_s$, etc. These typical features

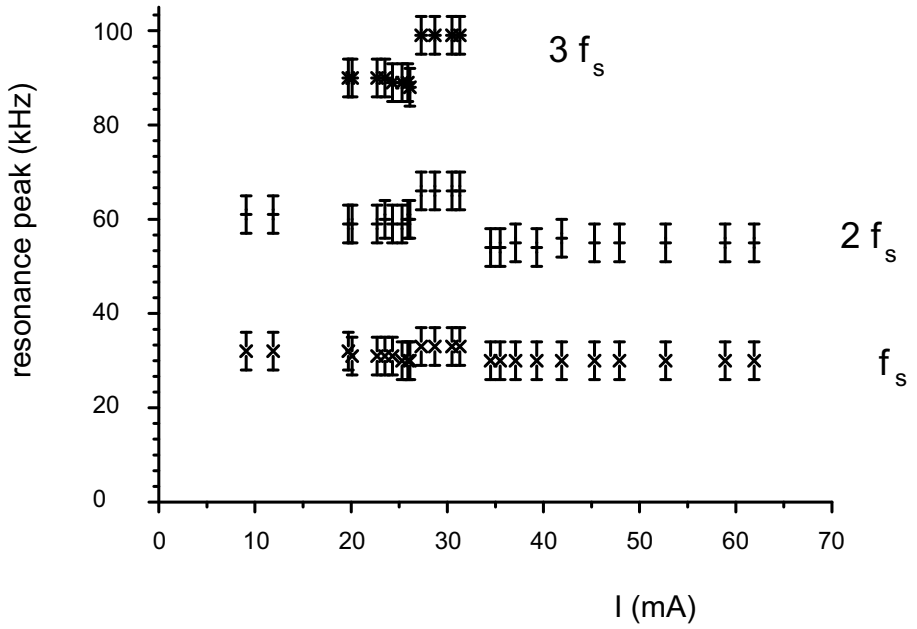

Figure 4.8: *Resonance peak of the coherent synchrotron oscillations observed with a spectrum analyzer in function of the current, $V_{hRF} = 150$ kV. f_s is the synchrotron frequency.*

appear clearly from the spectrum analyzer images and in more detail from the streak camera images taken at Super ACO. Figure (4.8) presents the detected coherent oscillations of the electrons in the bunch with a spectrum analyzer. The spectrum analyzer pictures exhibit resonance frequency peaks separated from the central frequency peak, which is at a harmonic of the revolution frequency. Figure (4.8) displays the distance of these peaks with respect to the central value. Coherent synchrotron oscillations of dipolar and quadripolar type are always present from low to high current. We observe that even sextupolar coherent oscillations appear in the current region below the anti-threshold, here $I_s = 33$ mA for $V_{hRF} = 150$ kV.
It is to be noted that the amplitudes of the side peaks, with respect to that of the central peak, gives an indication of the number of electrons oscillating coherently. At high current, above the anti-threshold and for a relatively stable beam, these amplitudes are rather small; in the intermediate current region these amplitudes are comparable to the amplitude of the central peak: a substantial number of electrons undergoes the coherent oscillations and the resulting instability is quite strong.
Figure (4.9) shows the electron longitudinal distribution in a complex oscillation mode at the anti-threshold. The distribution is not Gaussian, but shows that the bunch is divided in parts, oscillating in phase opposition at the synchrotron frequency. The wakefield is a function of the electronic density and may be modelled by a decaying exponential multiplied by a periodic function, where the decay time constant as well as the period depend on the impedance of the ring [29]. A simple model has been used [23] to reproduce the instability modes observed at Super ACO with the auxiliary cavity, from the simple coherent synchrotron oscillation to complex modes like the fish-bones instability [34] (named as such due to its appearance on a DSSC image). This simple model suggests that the collective oscillating modes of the electrons in the bunch derive

from a relatively short decay time constant of the wakefield, so that the wakefield interacts only with the electrons of the same bunch, the instability being a single bunch instability. In addition, the wakefield responsible for the complex modes observed in the intermediate current region may explain the anti-threshold value: the instability sets in when the electrons are sufficiently close to each other that their wakefield is so strong to perturb their closest neighbors. When the current increases, the bunch lengthens, and the electron density decreases. When the closest neighbors are too far to be perturbed by the wake, the instability disappears. This explains the increasing anti-threshold current with increasing V_{RF}.
The dynamics of the electron beam and the different perturbations that are present in the beam are important because they influence the SRFEL dynamics. The longitudinal instabilities observed here modify the electron bunch parameters. This consists of an increase of the energy spread, and as a consequence of the bunch length, and also of a coherent oscillating movement of the bunch longitudinal phase space distribution moments. These effects on the beam induce perturbations in the laser dynamics and in the laser properties such as gain, stability, etc. This will be described in the coming section.

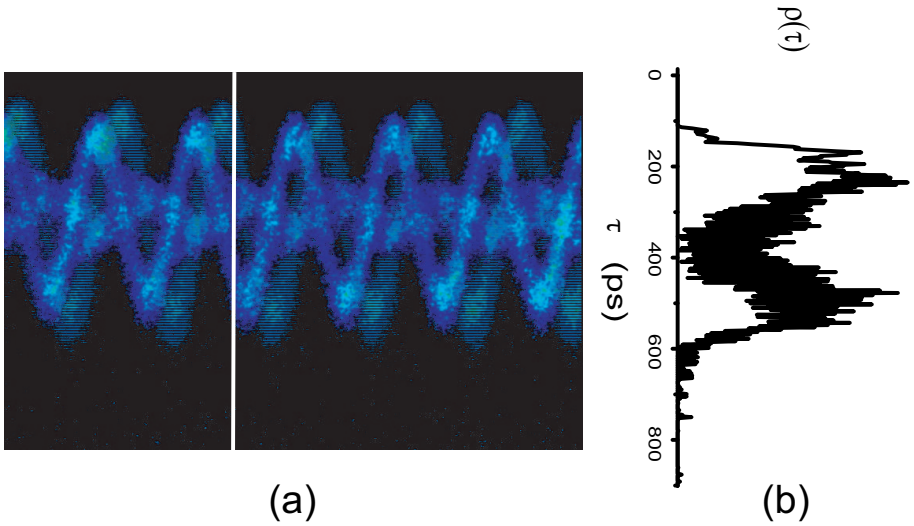

Figure 4.9: *(a) DSSC image showing the evolution of the perturbed longitudinal bunch distribution. The instability sets on when the total current is below the 'anti-threshold' $I_s \approx 32$ mA with $V_{hRF} = 150$ kV. The bunch distribution is split in three parts oscillating at near the synchrotron frequency $f_s = 33$ kHz. $V_{hRF} = 150$ kV, one bunch mode (horizontal scale: 200 μs, vertical scale: 800 ps). (b) Bunch longitudinal distribution, $\rho(\tau)$, extracted from the DSSC image (a). $V_{hRF} = 150$ kV.*

4.3 Laser-beam dynamics

The Super-ACO FEL is a pulsed laser with a pulse repetition rate corresponding to that of the passage of the electron bunches in the optical cavity, 8.33 MHz. The optical klystron [35] in the laser cavity is composed of two undulators separated by a dispersive section. The laser r.m.s pulse duration is much shorter than the electron bunch length,

Table 4.1: *Super-ACO FEL parameters*

Storage ring		**FEL Constituting elements**	
E_0 (MeV)	800	Cavity length (m)	18
T_0 (ns)	240		
α_c	0.0148	Optical klystron length (m)	3,1
$\sigma_{\epsilon,0}$	$5.4 \cdot 10^{-4}$	undulators period length (cm)	12.9
ν_{RF} (MHz)	100	N_u	10
ν_{hRF} (MHz)	500	N_d	80-100
V_{RF} (kV)	170		
V_{hRF} (kV)	0-280	**FEL Characteristics**	
β_x (m)	1.528	r.m.s pulse duration (ps)	10
η(m)	0.364	beamwaist (μm)	400
ϵ_x (m)	$2.7 \cdot 10^{-8}$	Maximum average output power (350 nm) (mW)	300

typically 10-20 ps, at zero 'detuning', the detuning being the cumulative delay between the laser pulse and the electron bunch. The Super ACO FEL parameters can be found in table (4.1). In this section we present the laser properties in presence of the auxiliary cavity. At the same time the instabilities due to wakefields perturb the laser and modify its performance. The laser operates in competition with the instabilities, in particular the microwave instability. In fact the laser itself can be considered as an instability of a different kind.

4.3.1 Super-ACO FEL gain

One important parameter for the SRFEL dynamics is the gain. The gain is a dynamical quantity. The maximum gain is when the laser starts, and is called the small signal gain. The gain evolves with the electron bunch quality and the detuning condition.
The small signal gain, for the optical klystron case, can be deduced from bunch length and relative energy spread measurements [35]:

$$G_0 = 2.22 \cdot 10^{-13} K^2 L_{und}^2 (JJ)^2 \left(N_u + N_d\right) f \frac{\rho_e F_f}{\gamma^3}, \tag{4.7}$$

where K is the undulator strength, L_{und} is the length of one undulator, JJ is the difference between the first kind Bessel functions of order 0 and 1 with argument $x = \dfrac{K^2}{4+2K^2}$, F_f is the filling factor (taking into account the transverse overlap of the electrons with the photon beam), N_u is the number of periods of each identical undulator, N_d is the number accounting for the advance of the light with respect to the electrons due to the dispersive section, and it is expressed in number of light wavelength [35]; $f = f_0 \exp\left(-8\left(\pi\left(N_u + N_d\right)\sigma_\epsilon\right)^2\right)$ is the so-called 'modulation rate' of the optical klystron [35] with f_0 a constant between 0 and 1; σ_ϵ is the relative beam energy spread; ρ_e is the electron density and γ is the Lorentz factor corresponding to the electrons nominal energy.

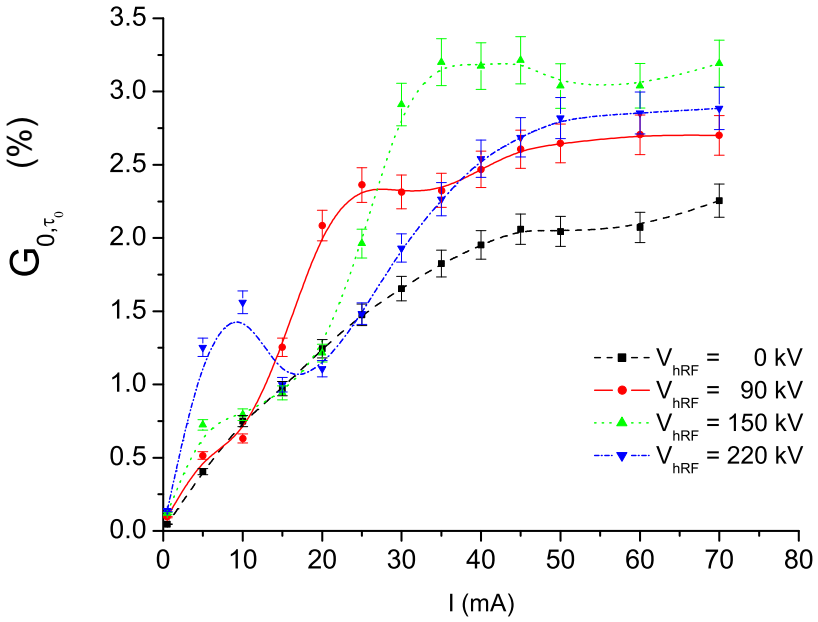

Figure 4.10: *Maximum Gain curves vs. current at 350 nm and for different values of the harmonic cavity voltage V_{hRF}, using the expression (4.7) with an optimized N_d value, $(N_u + N_d)f = (N_u + N_d)e^{-8\pi^2(N_u+N_d)^2(\frac{\sigma_\gamma}{\gamma})^2} \approx \frac{\exp(-\frac{1}{2})}{4\pi\frac{\sigma_\gamma}{\gamma}}$, and $K = 3.5$, $L_{und} = 1.3$ m, $F_f = 0.9$, $\sigma_x = 380$ (μm), $\sigma_y = 380$ (μm) .*

Figure (4.10) presents the small signal gain as a function of the current at the laser wavelength 350 nm and for different values of V_{hRF}. At low current, the small signal gain increases monotonically with V_{hRF}: the harmonic cavity, reducing the bunch length, is efficient. However, for 1% total cavity loss, the threshold value of the current for which the laser starts is $I_{thr,Las} \approx 5$, 12, 15, 16 mA with $V_{hRF} = 220$, 150, 90, 0 kV respectively.
For intermediate current zone instabilities occur on the beam. The small signal gain is lowered due to the bunch lengthening and the increased energy spread, and the reduction of G_0 is more important for higher values of V_{hRF}. For non static electron bunch distribution the small signal gain can not be defined: this is only possible for a static longitudinal phase space distribution.
Above the 'anti-threshold', I_s, the microwave instability dominates. This leads to a limitation of the small signal gain, which does not increase significantly with the current as expected from expression (4.7).
The harmonic cavity functioning in the bunch shortening mode for enhance the laser gain is efficient because the gain increases with the V_{hRF}, but at the same time the efficiency is less than expected as the beam also experiences instabilities.

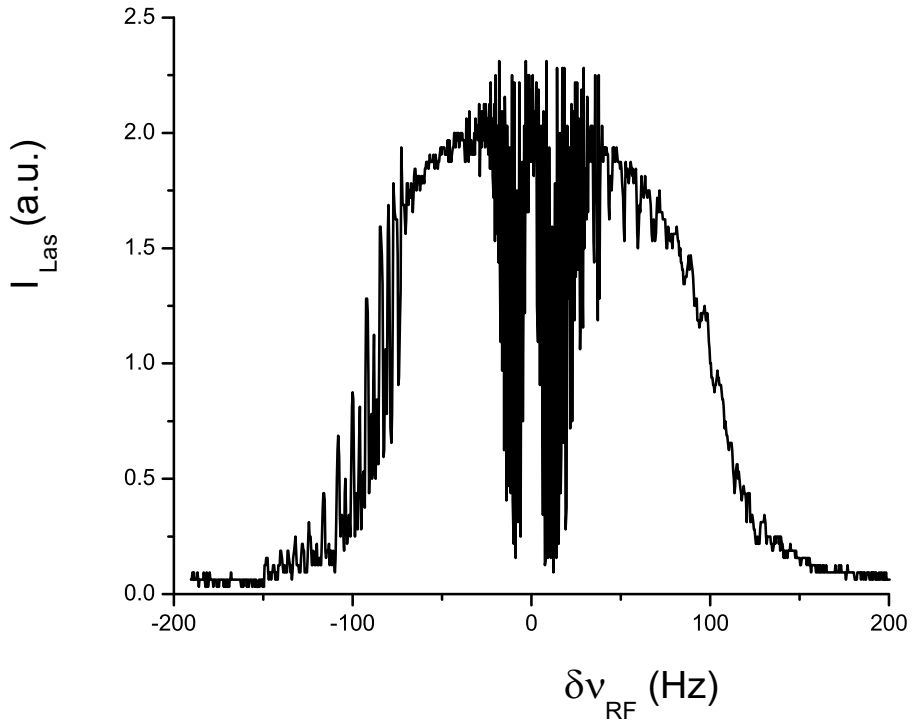

Figure 4.11: *Detuning curve for the passive harmonic cavity. The current is 39.4 mA.*

4.3.2 Temporal and dynamical features

The DSSC also provides information on the laser pulse as for the electron bunch longitudinal distribution, i.e. the pulse duration, the pulse centroid, etc.

The temporal behavior of the laser corresponds to the periodic structure of the electron beam. For perfect longitudinal tuning the laser behaves as a cw-laser. Longitudinal detuning leads to a cumulative delay between the pulse and the bunch: for small and large detuning values the laser is cw [36] on a macro-temporal scale (time greater than the cavity round trip, of the order of several synchrotron damping time), and for intermediate detuning values the laser shows a pulsed behavior. A 'detuning curve' presents a particular laser property as function of the detuning, such as the intensity or pulse duration. It provides information on the dynamics of the coupled system. As seen in the previous section, collective effects distort the bunch distribution, and the distortion is more important for higher current and higher voltage V_{hRF}. The detuning curves for passive harmonic cavity are symmetrical, as shown in figure (4.11), and become asymmetrical while increasing the voltage V_{hRF} (figure (4.12)). The symmetry of the detuning curve depends on the symmetry of the longitudinal bunch distribution: the position of the laser pulse centroid is subject to the detuning, which pushes the pulse centroid away from the electron bunch centroid, and to the gain variation along the bunch distribution, which pulls the laser pulse centroid back to the electron bunch centroid where the electron density is maximum ('gain gradient effect'). When the laser reaches an equilibrium for a given detuning, its centroid also reaches an equilibrium point and the detuning effect is compensated by the gain gradient effect. With an asymmetrical bunch distribution, this effect is asymmetrical, and the equilibrium found

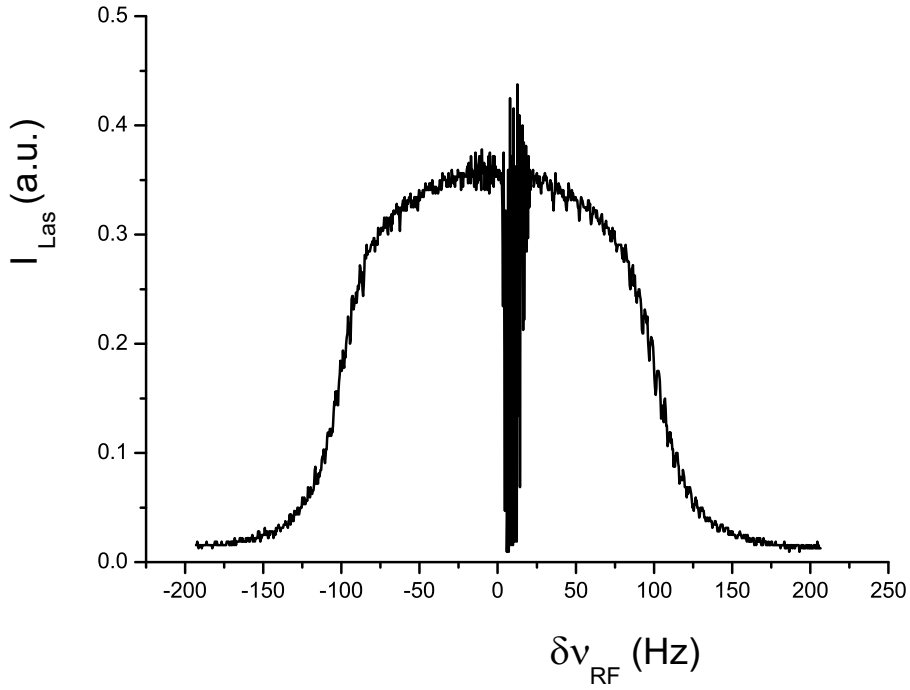

Figure 4.12: *Detuning curve for $V_{hRF} = 90$ kV. The current is 26 mA.*

for a given detuning may not be the same for the symmetrical detuning amount. Then the resulting detuning curve is asymmetrical.

The detuning curve characteristics, such as the total width (≈ 250 Hz in figure (4.11)), depend on the properties of the dynamical system, e.g. the laser gain, the cavity loss, the instability strength. The first two quantities determine the level of the laser intra-cavity power at equilibrium. This level is important because it determines if the laser is capable to switch off the microwave instability. The gain decreases with decreasing current but also under detuning condition. At large detuning, the gain reaches a limit where the intra-cavity power can not switch the microwave instability off. Therefore the instability starts, with a consequent increase of energy spread that further decreases the gain bellow the cavity loss. As a result the laser is switched off. Consequently, for a given current, cavity loss and microwave instability strength, the larger the gain the larger the detuning width [22].

4.3.3 Spectral features

The spectral tunability of an FEL depends, in practice, on the undulator strength parameter, $K = 0.94[T^{-1}cm^{-1}]\,\lambda_u\,B_u$ (with B_u the amplitude of the periodic magnetic field of the undulator) and also on the reflexivity of the mirrors. At Super ACO, at 350 nm the sets of mirrors allow a global tunability range of [300, 600] nm.
One interesting characteristic of the *UV-VUV* SRFEL (down to 189 nm for ELETTRA and 300 nm for Super ACO) is its spectral width which is sufficiently small, and combined with the short laser pulse duration, makes the laser an interesting device to perform time resolved spectroscopy [11]. The relative spectral bandwidth, $\frac{\Delta\lambda}{\lambda}$, obtained

with an SRFEL is roughly given by the expression [37] :

$$\frac{\Delta\lambda}{\lambda} \approx \frac{1}{\pi}\sqrt{\frac{\lambda}{(N+N_d)c\sigma_\tau}}, \tag{4.8}$$

with c the speed of light in vacuum. For high time-resolved spectroscopy one needs a high frequency resolution as well as high time resolution, which are both coupled with the Fourier limit. Measurements of the laser pulse duration and its spectral width as function of the detuning have shown the laser operating near the Fourier limit in a narrow central detuning zone [37]. The laser pulse duration, σ_{Las}, depends on the bunch length. With the auxiliary cavity it should operate at shorter pulse duration, so that the product $\sigma_{Las}\frac{\Delta\lambda}{\lambda}$ may be closer to the Fourier limit. But any longitudinal instability adds a certain amount of detuning pushing the laser away from the limit. With a feedback system [38], which maintains the laser at zero detuning, the pulse duration has been found shorter and closer to the theoretical value given by $\sigma_{Las} \approx \sqrt{\Delta\,\sigma_\tau}$ [39] (where $\Delta = (N+N_d)\frac{\lambda_{las}}{c}$ is the slippage length expressed in s). Operating the laser near the Fourier limit appears like a trade-off between the laser pulse shortening and the rising of instabilities.

4.3.4 FEL power

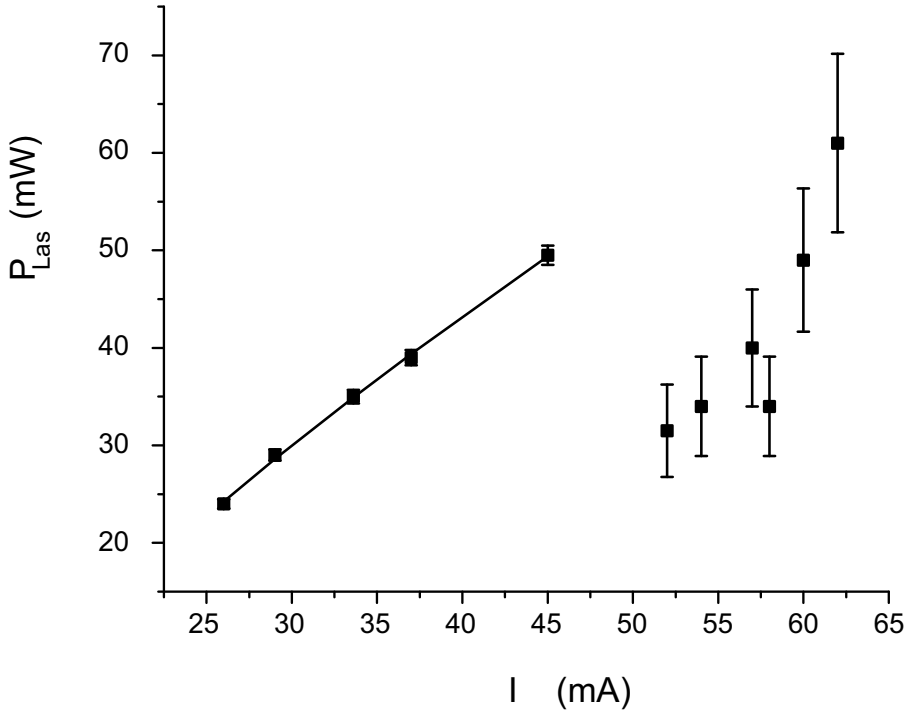

Figure 4.13: *Laser power vs. current for $V_{hRF} = 120$ kV.*

The Renieri limit [40] tells that the SRFEL average power extracted is proportional to the average power emitted by the synchrotron radiation in a bending magnet. For an optical klystron the average power which can be extracted is [41]:

$$P_{laser} = \eta_c 8\pi^2 (N_u + N_d) f((\frac{\sigma_\gamma}{\gamma})^2_{on} - (\frac{\sigma_\gamma}{\gamma})^2_{off}) P_s, \tag{4.9}$$

where η_c is the ratio between the transmission of the mirrors and the total losses of the cavity, $((\frac{\sigma_\gamma}{\gamma})^2_{on} - (\frac{\sigma_\gamma}{\gamma})^2_{off})$ measures the laser induced energy spread of the beam, and $P_s = \frac{2\,c\,r_e\,m_e c^2\,T_0}{3\,e}\,\frac{\gamma^4 I}{\rho_0^2}$ is the synchrotron power, with r_e the electron classical radius, m_e the electron mass, e the electron charge, I is the current and ρ_0 is the average radius of curvature of the storage ring bending magnets. Since P_s is proportional to the current and $(N_u + N_d)f$ is, when optimized, inversely proportional to the relative energy spread of the beam, P_{laser} is expected then to be proportional to the current I^β. In fact the situation is more complex. At high current the laser starts. Then it is in competition with the microwave instability, it switches off the instability [21]-[42], and the resulting power may be in a large range, depending on the strength of the instability. Figure (4.13) presents the power extracted at Super ACO and shows this effect. When the current decreases, the strength of the wakefield, responsible for the instabilities, decreases also. The laser is then less sensitive to the instabilities, and the behavior of the power vs. current is indeed proportional to I^β (where $\beta \approx 0.8$).

4.3.5 Competition between the FEL and the beam instabilities

As seen in the previous section the FEL gain and the extracted power can be reduced by perturbations of the electron beam. A simple effect of the laser on the beam, which has been observed at VEPP3 [14] and UVSOR [43], is "heating" of the beam. The FEL induces beam energy spread which results proportionally in bunch lengthening. At Super-ACO, the FEL induced heating of the beam has also been observed, by measuring a difference of energy spread laser on and off in excess of 10 %. Instead of only heating the beam, the laser, by inducing energy spread to the beam, damps the beam instabilities. As observed on the spectrum analyzer, the quadrupolar coherent synchrotron oscillations disappear with laser on, and reappear with laser off. Furthermore, as has been described in [42] the laser induced energy spread shifts the Boussard threshold current and then prevents the start of the microwave instability.
This results have been reproduced with simulations using the model described in [21]. We made simulations for the case of Super ACO, $V_{hRF} = 90$ kV in the perfect longitudinal tuning condition, in the case (a), the current $I = 100$ mA, and in the case (b) the current is $I = 60$ mA.
In the case (a) we evaluate the small signal gain $g_0 = 3\%$ and the microwave instability strength has been calculated using a normalized impedance $\frac{Z_n}{n} = 4\,\Omega$. The laser starts, but the microwave instability is too strong and switches the laser off, as can be seen in figure (4.14) showing the intra-cavity dimensionless power, the relative energy spread and the microwave instability growth rate vs. time respectively. The induced relative energy spread is then oscillating in the characteristic sawtooth regime of the microwave instability.
In the case (b), the small signal gain is $g_0 = 2.5\%$, the gain is smaller but the microwave instability strength is also smaller. The laser starts, reaches saturation, and the laser

induced relative energy spread is high enough to switch the microwave instability off and to prevent it from starting again, as shown in figure (4.14). The laser characteristics in that simulation are close to the non perturbed case. But for example the pulse duration $\sigma_{Las} = 20$ ps, in agreement with the measurements, is longer than in the ideal case without instability (numerical), $\sigma_{Las} = 7$ ps. The latter value is close to the theoretical value given by the 'Super mode' model [39], $\sigma_{Las,th} = 3$ ps.
In addition the code shows that the start-up of the laser is possible only in a range of current for which the upper limit depends on the microwave instability strength, which is given by the impedance of the ring and the current. In this particular case the upper limit is near 90 mA. We observe experimentally that the laser is not stable above 60 mA
In summary, the laser can be seen as a beam stabilizer as it is able to damp the beam instabilities, and as a consequence the laser, whenever it starts and reaches a sufficient power level, self-stabilizes.

4.4 Conclusion

Beam phenomena in a storage ring, in particular for the Super ACO storage ring, using an auxiliary 5^{th} harmonic cavity have been described both for the situations without and with the operation of an FEL.
First the particular phenomena in the storage ring without operating the FEL have been characterized, such as the PWD and MI effects, as a function of the setting of the harmonic cavity voltage. Explanations for most of these phenomena have been given. Their consequences on the FEL dynamics have been considered next.
Gain enhancement due to the bunch length shortening as a function of the harmonic cavity voltage has been observed.
However gain reduction occurs also, which is caused by: bunch lengthening induced by the PWD, bunch lengthening proportional to the increased energy spread induced by the MI and by coherent synchrotron oscillations.
Phenomena observed under detuning conditions are linked to the bunch parameters, as influenced by the MI and the harmonic cavity voltage. The detuning curve properties derive from the effective gain, the MI strength, and the bunch longitudinal distribution shape. The detuning studies as such are primarily intended for providing understanding of the combined laser - electron beam system.
The competition of the laser with the MI has been illustrated with our numerical code and has been compared with experimental results.
Optimum conditions for operating the FEL use a moderate harmonic cavity voltage, e.g. 150 kV for Super ACO, and a beam current in the range of 20 to 60 mA, which allows stable operation of the FEL near the Fourier limit.

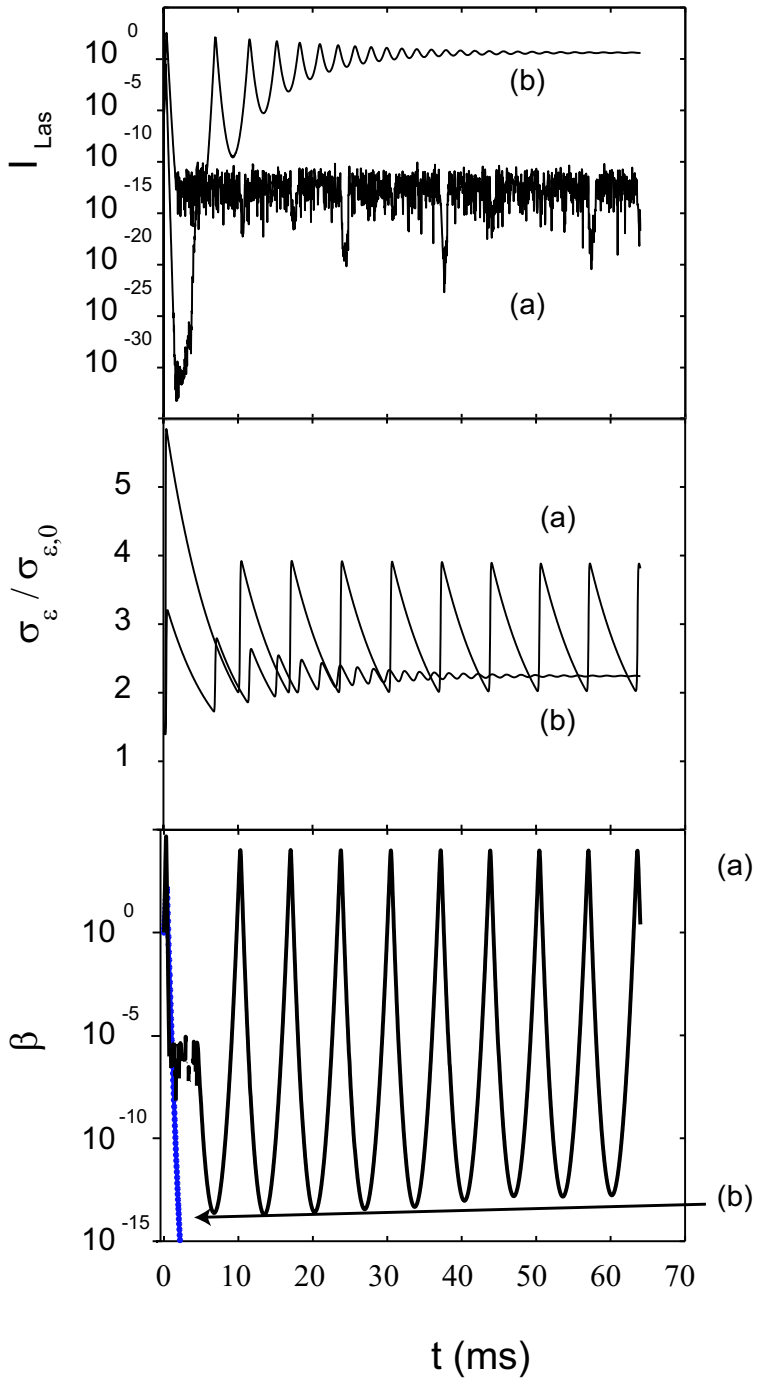

Figure 4.14: *Simulation for the case of Super ACO with $V_{hRF} = 90$ kV and the current $I = 100$ mA (a) and $I = 60$ mA (b).* ***Top****: Laser dimensionless intra-cavity power, I_{Las} .The power density is given by $P = I_{Las}\, I_{sat}$ [21] with $I_{sat} = 690(\frac{\gamma}{N_u})^4 \frac{1}{(K\,\lambda_u f_b(\xi))^2}$ MW cm^{-2}, where $\gamma = 1566.55$ is the Lorentz factor of the electrons, $N_u = 44$ is the number of undulator period (for the equivalent undulator to the Super ACO optical klystron), $K = 3.3$ is the undulator strength, $\lambda_u = 0.13$ m, and $f_b(\xi)$ is the difference between the first kind Bessel functions of zero and first order with the argument $\xi = \frac{K^2}{4+2\,K^2}$.* ***Center****: relative energy spread, $\sigma_\epsilon/\sigma_{\epsilon,0}$.* ***Bottom****: microwave instability growth rate, β.*

References

[1] J. M. J. Madey. Stimulated emission of bremmstrahlung in a periodinc magnetic field. *Jounal of Applied Physics*, 42(5):1906, 1971.

[2] M. Billardon, D. Garzella, and M. E. Couprie. Saturation mechanism for a storage-ring free-electron laser. *Physical Review Letters*, 69:2368–2371, October 1992.

[3] D. A. G. Deacon, L. R. Elias, J. M. J. Madey, G. J. Ramian, H. A. Schwettman, and T. I. Smith. First operation of a free-electron laser. *Physical Review Letters*, 38:892, April 1977.

[4] M. Billardon, J. M. Ortega, P. Elleaume, C. Bazin, M. Bergher, M. Velghe, Y. Petroff, D. A. G. Deacon, K. E. Robinson, and J. M. J. Madey. First operation of a storage-ring free-electron laser. *Physical Review Letters*, 51:1652–1655, October 1983.

[5] D. Nutarelli, D. Garzella, E. Renault, L. Nahon, and M. E. Couprie. Super ACO FEL oscillation at 300 nm. *Nuclear Instruments and Methods in Physics Research A*, 445:143, May 2000.

[6] R. P. Walker, J. A. Clarke, M. E. Couprie, G. Dattoli, M. Eriksson, D. Garzella, L. Giannessi, M. Marsi, M. W. Poole, E. Renault, R. Roux, M. Trovò, S. Werin, and K. Wille. The European UV/VUV storage ring FEL at ELETTRA: first operation and future prospects. *Nuclear Instruments and Methods in Physics Research A*, 467:34–37, July 2001.

[7] D. Nölle, D. Garzella, A. Geisler, L. Gianessi, M. Hirsch, H. Quick, M. Ridder, T. Schmidt, and K. Wille. First lasing of the FELICITA I FEL at DELTA. *Nuclear Instruments and Methods in Physics Research A*, 445:128–133, May 2000.

[8] V. N. Litvinenko, S. H. Park, I. V. Pinayev, and Y. Wu. Operation of the OK-4/Duke storage ring FEL below 200nm. *Nuclear Instruments and Methods in Physics Research A*, 475:195–204, December 2001.

[9] M. Hosaka, S. Koda, M. Katoh, J. Yamazaki, K. Hayashi, K. Takashima, T. Gejo, and H. Hama. From the operation of an SRFEL to a user facility. *Nuclear Instruments and Methods in Physics Research A*, 483:146–151, May 2002.

[10] K. Yamada, N. Sei, H. Ohgaki, T. Mikado, S. Sugiyama, and T. Yamazaki. Lasing towards the VUV in the NIJI-IV FEL. *Nuclear Instruments and Methods in Physics Research Section A*, 445(1-3):173, 2000.

[11] M. E. Couprie, F. Mérola, P. Tauc, D. Garzella, A. Delboulbé, T. Hara, and M. Billardon. First use of the UV Super-ACO free-electron laser: Fluorescence decays and rotational dynamics of the NADH coenzyme. *Review of Scientific Instruments*, 65:1485–1495, May 1994.

[12] M. Marsi, M. E. Couprie, L. Nahon, D. Garzella, R. Bakker, A. Delboulbé, D. Nutarelli, R. Roux, B. Visentin, C. Grupp, G. Indlekofer, G. Panaccione,

A. Taleb-Ibrahimi, and M. Billardon. Two color experiments combining Free Electron Laser and Synchrotron Radiation. *Nuclear Instruments and Methods in Physics Research A*, 393:548–551, February 1997.

[13] M. Katoh, K. Hayashi, T. Honda, Y. Hori, M. Hosaka, T. Kinoshita, S. Kouda, Y. Takashima, and J. Yamazaki. New lattice for UVSOR. *Nuclear Instruments and Methods in Physics Research A*, 467:68–71, July 2001.

[14] N. A. Vinokurov, I. B. Drobyazko, G. N. Kulipanov, V. N. Litvinenko, and I. V. Pinayev. Lasing in visible and ultraviolet regions in an optical klystron installed on the VEPP-3 storage ring (invited). *Review of Scientific Instruments*, 60:1435–1438, July 1989.

[15] M. Kamada and H. Hama. Status of the UVSOR facility–1994. *Review of Scientific Instruments*, 66:2362–2364, February 1995.

[16] G. Dattoli, A. Dipace, E. Sabia, A. Torre, G. K. Voykov, and M. Carpanese. A simple three-dimensional free electron laser code. *Journal of Applied Physics*, 80:6589, December 1996.

[17] V. N. Litvinenko, B. Burnham, J. M. J. Madey, and Y. Wu. Giant laser pulses in the Duke storage ring UV FEL. *Nuclear Instruments and Methods in Physics Research A*, 358:334, February 1995.

[18] V. N. Litvinenko, Y. Wu, B. Burnham, and J. M. J. Madey. Expected performance of the mm-wave isochronous FEL at the Duke storage ring. *Nuclear Instruments and Methods in Physics Research A*, 358:349, February 1995.

[19] G. Dattoli, L. Mezi, M. Migliorati, and L. Palumbo. A simple model for the saw-tooth instability in storage rings. *Nuovo Cimento A Serie*, 112:491, May 1999.

[20] R. Roux and M. Billardon. Storage ring free electron laser and coherent synchrotron oscillation: Simulation approach. *Nuovo Cimento A Serie*, 112:513, May 1999.

[21] C. A. Thomas, J. I. M. Botman, G. D. Ninno, M. E. Couprie, L. Mezi, and G. Dattoli. SRFEL dynamics investigated with a 1-D numerical code. *Nuclear Instruments and Methods in Physics Research A*, 483:181–185, May 2002.

[22] C. A. Thomas, J. I. M. Botman, C. Bruni, D. Garzella, M. E. Couprie, G. D. Ninno, and G. Dattoli. Longitudinal Detuning for an SRFEL. *to be published in Nuclear Instruments and Methods in Physics Research A*, 2003.

[23] R. Roux, M. E. Couprie, T. Hara, R. J. Bakker, B. Visentin, M. Billardon, and J. Roux. The Super-ACO FEL dynamics measured with a streak camera. *Nuclear Instruments and Methods in Physics Research A*, 393:33–37, February 1997.

[24] D. Nutarelli. *Dynamique et performances du laser à électron libres de Super-ACO avec une cavité harmonique à 500 MHz.* PhD thesis, Université Paris Sud, Orsay (France), January 2000.

[25] M. Sands. *The physics of electron storage ring, an introduction*, volume 121. SLAC report, November 1970.

[26] J. Haissinski. *Nuovo Cimento B*, 18:72, 1973.

[27] K. Bane. Bunch lengthening in the SLC damping ring. SLAC-PUB Report 5177, SLAC, 1990.

[28] C.A. Thomas, J.I.M. Botman, R. Bartolini, G. Dattoli, L. Mezi, and M. Migliorati. An analytical solution for the Haissinski equation with purely inductive wake fields. *Europhysics Letters*, 60(1):66, October 2002.

[29] A. Hofmann. *Beam instabilities*, volume 95-06 of *CAS: 5th Advanced Accelerator Physics Course*, chapter 14. CERN Accelerator School, 1995.

[30] H. Hama and M. Hosaka. Longitudinal beam dynamics and FEL interaction on a negative momentum compaction storage ring. *Nuclear Instruments and Methods in Physics Research A*, 429:172–178, June 1999.

[31] D. Boussard. internal report 75-2, CERN, 1975.

[32] G. Dattoli, L. Mezi, M. Migliorati, A. Renieri, M. E. Couprie, D. Garzella, D. Nutarelli, C. Thomas, G. De Ninno, and R. Walker. Electron beam properties and impedance characterization for storage rings used for free electron lasers. *Nuclear Instruments and Methods in Physics Research A*, 471:403, October 2001.

[33] M. Migliorati, L. Palumbo, G. Dattoli, and L. Mezi. Saw-tooth instability in storage rings: simulations and dynamical model. *Nuclear Instruments and Methods in Physics Research A*, 437:134, November 1999.

[34] Roux R. *Dynamique et condition de stabilité du laser à électron libres de Super-ACO. Fonctionnement avec une cavité simple ou double.* PhD thesis, Université Paris Sud, Orsay (France), January 1999.

[35] P. Elleaume. The Optical klystron. *J. de Phys. (Paris)*, 44(C1):353, 1983.

[36] M. E. Couprie, V. Litvinienko, D. Garzella, A. Delboulbé, M. Velghe, and M. Billardon. Dynamical study of the Super-ACO free electron laser with the dissector. *Nuclear Instruments and Methods in Physics Research A*, 331:37, July 1993.

[37] M. E. Couprie, G. De Ninno, G. Moneron, D. Nutarelli, M. Hirsch, D. Garzella, E. Renault, R. Roux, and C. Thomas. Towards the Fourier limit on the super-ACO Storage Ring FEL. *Nuclear Instruments and Methods in Physics Research A*, 475:229, December 2001.

[38] M. E. Couprie, D. Garzella, T. Hara, J. H. Codarbox, and M. Billardon. A longitudinal feedback for the Super-ACO free electron laser stability in the UV. *Nuclear Instruments and Methods in Physics Research A*, 358:374, February 1995.

[39] G. Dattoli and A. Renieri. Storage ring operation of the free-electron laser - The oscillator. *Nuovo Cimento B*, 59:1, September 1980.

[40] A. Renieri. Storage ring operation of the free-electron laser - The amplifier. *Nuovo Cimento B Serie*, 53:160, September 1979.

[41] D. A. G. Deacon, K. E. Robinson, J. M. J. Madey, C. Bazin, Y. Petroff, M. F. Velghe, M. Billardon, Y. Farge, J. M. Ortega, and P. Elleaume. Gain measurements versus theory for the ACO storage ring laser. *Optics Communications*, 40:373–378, February 1982.

[42] R. Bartolini, G. Dattoli, L. Mezi, A. Renieri, M. Migliorati, M. E. Couprie, G. de Ninno, and R. Roux. Suppression of the Sawtooth Instability in a Storage Ring by Free-Electron Laser: An Example of Nonlinear Stabilization by Noise. *Physical Review Letters*, 87:134801, September 2001.

[43] M. Hosaka, S. Koda, M. Katoh, J. Yamazaki, and H. Hama. FEL induced electron bunch heating observed by a method based on synchronous phase detection. *Nuclear Instruments and Methods in Physics Research A*, 475:217–221, December 2001.

Chapter 5

Comparison simulations vs. experiments

C. A. Thomas*, J.I.M. Botman
Applied Physics Department, Technische Universiteit Eindhoven, The Netherlands
C. Bruni, D. Garzella, M. E. Couprie
LURE, Université Paris Sud, France.
and
DSM/DRECAM/SPAM, CEA de Saclay, Gif sur Yvette, France.
G. De Ninno
Sincrotrone Trieste, Italy.
G. Dattoli
ENEA Frascati, Rome, Italy.

5.1 Introduction

The Storage ring free electron laser is a complex coupled dynamical system, and various models have been used to understand and predict its behavior. First models described analytically the FEL intensity evolution [1]-[2]. Later, more advanced and sophisticated models were developed providing numerically the evolution of the coupled system laser pulse - electron bunch [3]-[4]-[5] -[6]-[7]-[8]. As described in section (1.3) and in order to get more insight in the coupled dynamics, we implemented a 1-dimensional model in a numerical code [9] (see chapter 3), taking into account the laser pulse evolution, derived from the field propagation equations, coupled to the electron† longitudinal phase space evolution, and to the main longitudinal instability in storage rings, the microwave instability (MI) [10]-[11]. In the code, transverse effects are neglected and the electron bunch distribution has a Gaussian shape with a width proportional to the energy spread. The numerical values of the parameters used in the code are taken from the real parameters that characterize the studied SRFEL (see table (5.1)).

*This chapter in the present form in based on a article accepted by NIM A under the title "Longitudinal Detuning for an SRFEL".

†We use the term 'electrons' both for electrons (ELETTRA) and positrons (Super ACO).

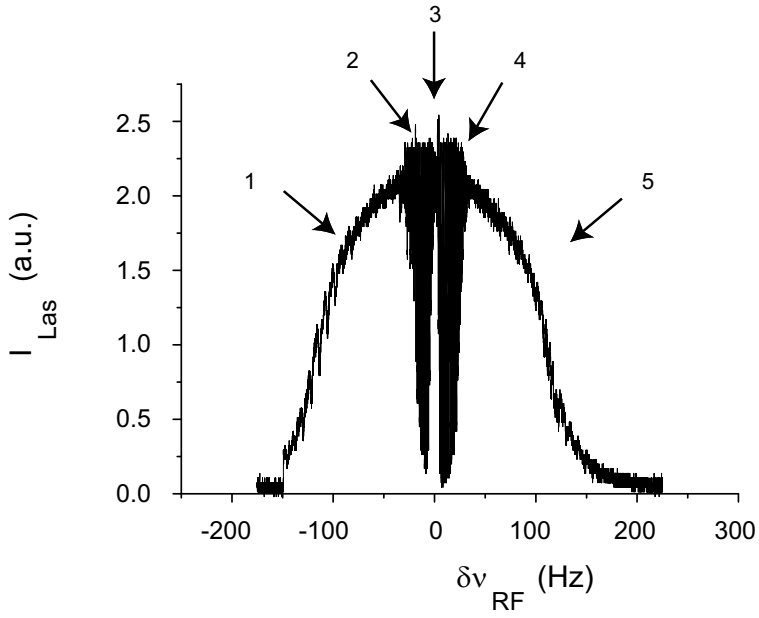

(a) Super ACO

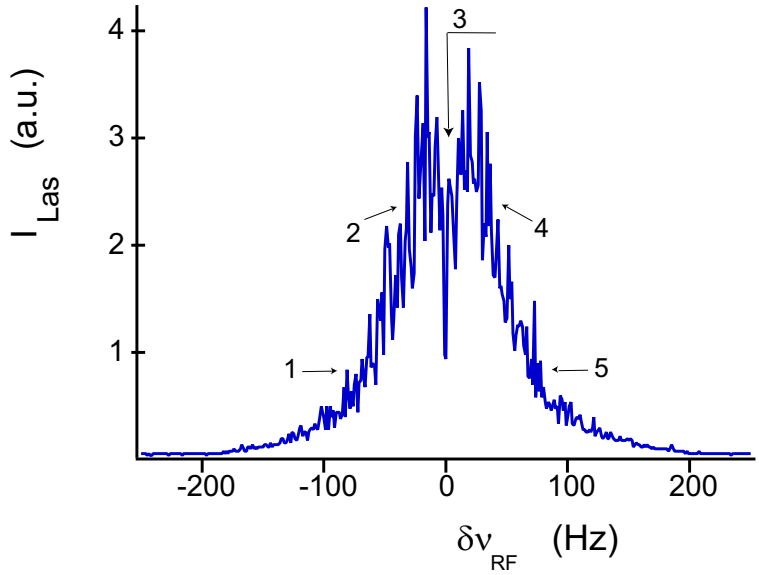

(b) ELETTRA

Figure 5.1: *Detuning curves measured at Super ACO (total current $I = 39.4$ mA, $g_0 = 2\%$, $\eta = 0.7\%$, passive harmonic cavity) and ELETTRA ([12]) ($I = 20$ mA, $g_0 = 12\%$, $\eta = 6\%$). a) The width is 330 Hz, zone 3 is less than 10 Hz large, zones 2 and 4 are in the detuning range $\nu_{RF} = [5, 25]$ Hz. b) The width is 400 Hz, zone 3 is less than 1 Hz, zones 2 and 4 are in the range $\nu_{RF} = [1, 30]$ Hz (1 Hz corresponding to a delay per pass of 1.2 fs at Super ACO and 0.86 fs at ELETTRA).*

The temporal behavior of the laser corresponds to the periodic structure of the electron beam. On a long time scale the behavior of the laser depends on the detuning condition. For perfect tuning the laser behaves as a cw-laser. A given detuning leads to a cumulative delay between the pulse and the bunch. For small and large detuning values the laser appears cw, and for intermediate detuning values the laser shows a pulsed behavior [13]. A detuning curve is a curve of a particular laser property, such as the intensity, pulse duration, etc, as function of the detuning, which is controlled by the cavity length or by the RF cavity frequency[‡]. It provides information on the dynamics of the coupled system. In this chapter we first present detuning curves obtained experimentally at Super ACO, and presented in a previous work [14], and at ELETTRA. In the second part we compare them with results obtained with the simulation code and finally we discuss the characteristics of the curves linked to the properties of the dynamical system.

5.2 Detuning curves

In general the shape of a detuning curve depends on the properties of the system, such as the FEL gain, the electron bunch phase space distribution, and on the instabilities in the laser and/or in the electron bunch.
The detuning curves shown in figure (5.1) are recorded by measuring the laser intensity while varying the frequency of the main RF cavity around the value for which the laser pulse period in the optical cavity corresponds to the inter-bunch period. Figure (5.1(a)) presents a detuning curve taken at Super ACO showing the laser intensity as a function of the RF frequency deviation $\delta\nu_{RF}$ from the central value. The curve is almost symmetrical and exhibits five characteristic detuning zones: in the central zone 3, 5 to 10 Hz wide, the laser operates in cw mode. For detuning values in the range between 5 and 25 Hz (zone 2 and 4) the laser appears pulsed (laser switches off periodically) or modulated (intensity modulation). Finally for larger detuning, more than 25 Hz (zone 1 and 5), the laser is cw again. This zones with a cw and modulated laser are also observed in Linac based FEL, although the detuning curve is quite asymmetrical and is mainly due to the slippage.
The case ELETTRA is different. The small signal gain ($g_0 > 30\%$) is large compared to Super ACO ($g_0 \approx 2.5\%$). The detuning curve is found to be more noisy, with a less sharp border between stable and pulsed behavior. However, figure (5.1(b)) still displays five distinct zones where the laser macro-temporal regime is either cw, (central zone 3 and lateral zones 1 and 5), or pulsed (zones 2 and 4).
A simple intuitive argument that can be used to determine the nature of the detuned dynamics of an SRFEL is the following: the position of the laser pulse centroid is pushed away from the electron bunch centroid due to the detuning, and is pulled back to the electron bunch centroid where the electron density is maximum, due to the gain variation along the bunch distribution. When for a given detuning the laser reaches an equilibrium in a cw mode, its centroid also reaches an equilibrium point and the detuning effect is compensated by the gain gradient effect. If no equilibrium is found the laser exhibits a pulsed or modulated behavior.

[‡]At Super ACO $\delta_{RF} = 1$ Hz is equivalent to a cavity length variation of $\Delta L_c = 0.18\,\mu$m, and at ELETTRA 1 Hz $\Leftrightarrow$ $0.13\,\mu$m

Another characteristic of the detuning curve is its total width. Figure (5.1) shows 330 and 400 Hz detuning width at Super ACO and ELETTRA respectively. Experimentally it is found to decrease with decreasing current and small signal gain (g_0).
The laser pulse duration vs. detuning is shown in figures (5.2(a)) and (5.2(b)) for Super ACO and ELETTRA respectively. The curves are symmetrical. One remarks that the pulse duration has a minimum in zone 3. In that zone the laser operates near the Fourier limit [15]. Zone 3 is quite interesting for user applications, as the laser has the shortest pulse duration and the smallest spectral width. For stability reasons this zone should be as large as possible. The extent of that zone depends on the gain and also on the ring synchrotron damping time (τ_s) [16], which is a crucial parameter. This zone has been measured to be as large as 5 to 10 Hz at Super ACO, with $\tau_s = 8.5$ ms and may have 1 Hz extent at ELETTRA, where $\tau_s = 65$ ms (for 1 GeV nominal electron energy).
In zone 2 and 4, the laser is pulsed or modulated. Figure (5.3) presents the pulse frequency in zone 2 and 4 as function of the detuning. The small asymmetry may be attributed to the slippage (delay between electrons and photons after traversing the undulator). The curve shows a high frequency modulation of the intensity for detuning values near ± 5 Hz. The frequency rapidly decreases to a minimum around 300 Hz, where the laser appears pulsed. The frequency increases linearly with $\delta\nu_{RF}$, the slope depending on the synchrotron damping time [16], with the laser becoming modulated again, as can be seen in figure (5.4).
In summary, several aspects of the experimental detuning curves at ELETTRA and Super ACO have been investigated. The total curve width depends on the small signal gain. The width of zone 3 depends on the small signal gain and on the damping time, which are also important parameters for the behavior of the laser in zones 2 and 4. In the following section, we compare these experimental results with the numerical results from our code.

Table 5.1: *ELETTRA and Super-ACO parameters.*

		ELETTRA	Super ACO
Nominal energy (GeV)	E_0	1	0.8
Number of electron bunches		4	2
Period (ring) (ns)	T_0	864	240
Momentum compaction factor	α_c	0.00161	0.0148
Synchrotron damping time (ms)	τ_s	65	8.5
Normalized impedance (Ω)	Z_n/n	0.1	5
Natural r.m.s energy spread (10^{-4})	σ_γ	3.97	5.4
Natural r.m.s bunch length (ps)	σ_b	6.28	86
Period (optical cavity) (ns)	T_c	216	120
small signal gain	g_0	0.35	0.025
cavity loss	η	0.06	0.005-0.01
laser wavelength (nm)	λ_{Las}	250	350
slippage (μm)		20	35

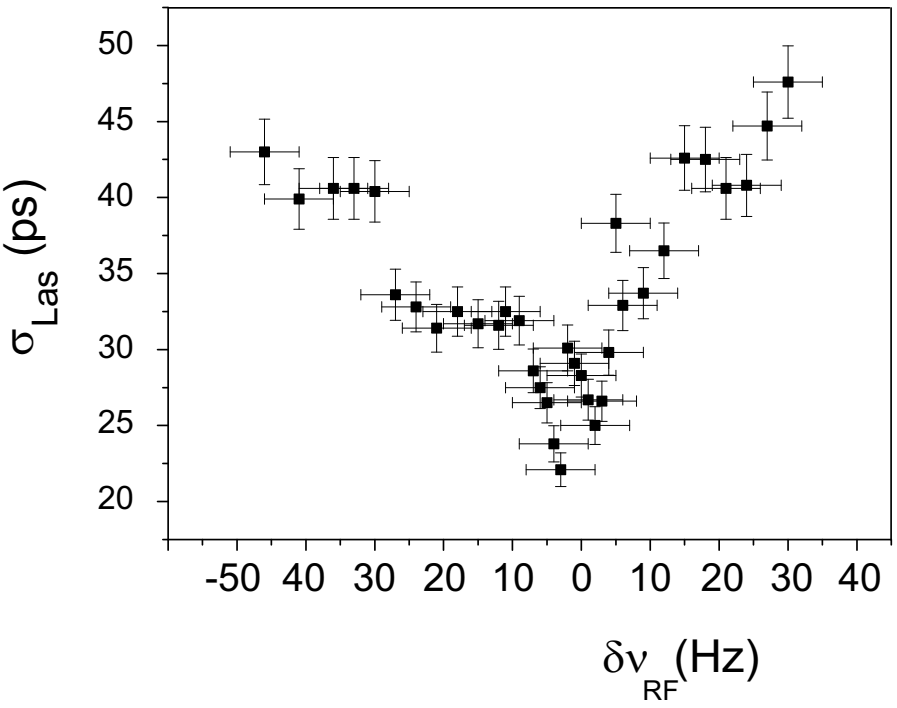

(a) Pulse duration vs. $\delta\nu_{RF}$ at Super ACO

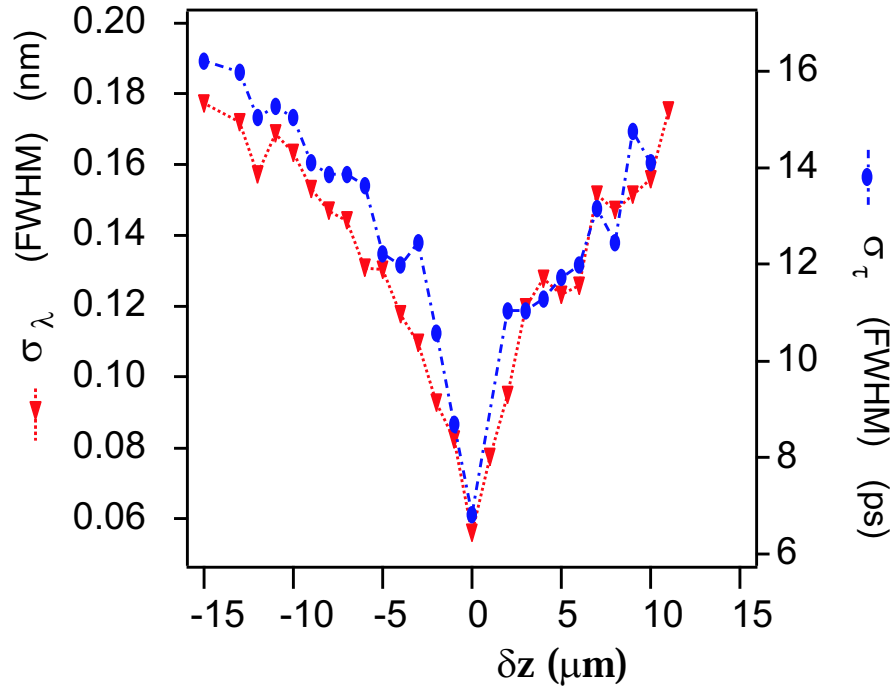

(b) Pulse duration and spectral width vs. detuning at ELETTRA

Figure 5.2: *Laser pulse duration vs. detuning: 5.2(a)(r.m.s value) $I = mA$, $g_0 = 2\%$, $\eta = 1\,\%$. 5.2(b) (FWHM value) $I = 15$ mA, $g_0 = 20\%$, $\eta = 6\%$; 5.2(b) laser spectral width (FWHM value) measured at the same time as for the pulse duration.*

5.3 Numerical results vs. experiments

The SRFEL longitudinal dynamics vs. detuning, taking the parameters of Super ACO and ELETTRA, is studied with our numerical code [9]. The code solves 3 differ-

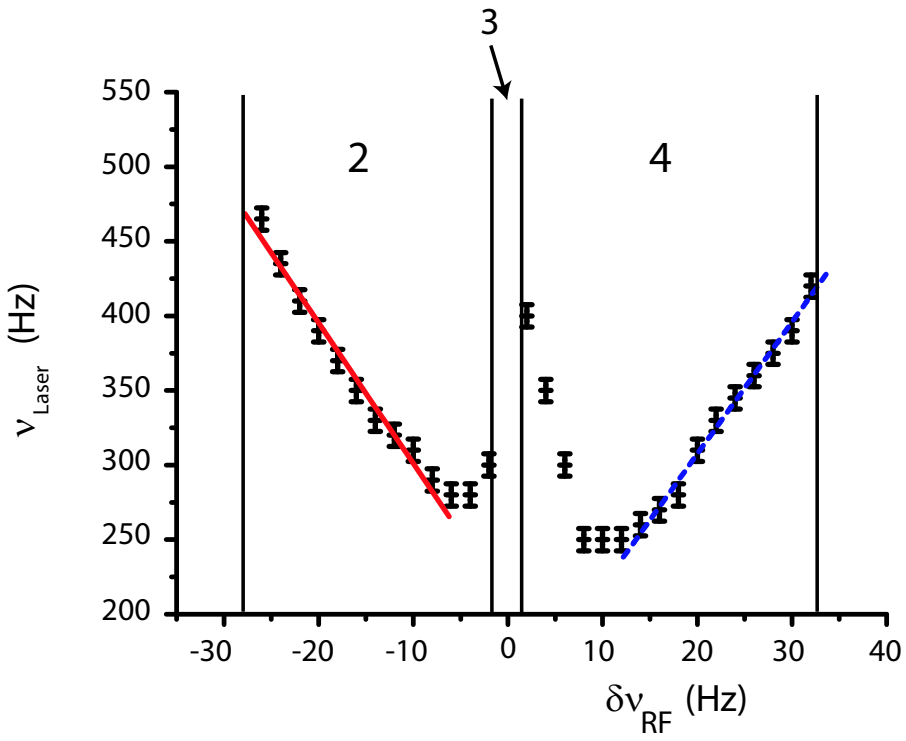

Figure 5.3: *Laser macro-temporal pulse frequency vs. detuning in zone 2 and 4 measured at Super ACO. The curve presents two linear domains nearly symmetrical as shown by the fitting slopes in the legend.* $I = 43\ mA$, $g_0 = 2\%$, $\eta = 0.8\%$

ential equations accounting for the laser intra-cavity electric field, the electron bunch energy spread and the microwave instability (MI) (see details in chapter (3)).
Figure (5.5(a)) presents the laser average power vs. detuning for the case of Super ACO. The bars represent the laser maximum and minimum intensity at equilibrium. One observes the five zones where the laser appears cw and pulsed. They are in relatively good agreement with Super ACO measurements: 300 Hz total width, 5 Hz width for zone 3 and 15 Hz width for zones 2 and 4, with $g_0 \approx 2\%$ and $\tau_s = 8.5$ ms. A similar experimental curve is obtained for ELETTRA exhibiting 5 characteristic zones. Zone 3 is 1 Hz wide and the total width is larger than 600 Hz. This is larger than the width of the experimental curve. A larger detuning curve for the case of ELETTRA may come from an overestimation of the effective gain and/or an underestimation of the MI strength. We develop this further argument below.

Variations of the effective gain, ($g_{0,eff} = g_0 - \eta$, with η the cavity loss) lead, as expected, to a variation of the curve width: the larger the gain, the larger the width. Figure (5.6(a)) of the laser power vs. detuning for different values of the effective gain shows a larger width for the larger effective gain. We also varied the microwave instability (MI) strength. In the code, the MI depends on two parameters, the MI excitation and the MI damping parameters, which are describing the onset and the growth of the instability, and its relaxation. The strength of the MI is measured by the ratio between these two parameters. It may be varied with the MI excitation parameter, which is directly linked to the impedance of the ring and the stored current [9]. Figure (5.7) presents the laser intra-cavity power at saturation in zone 3 as a function of the effective gain, and for two

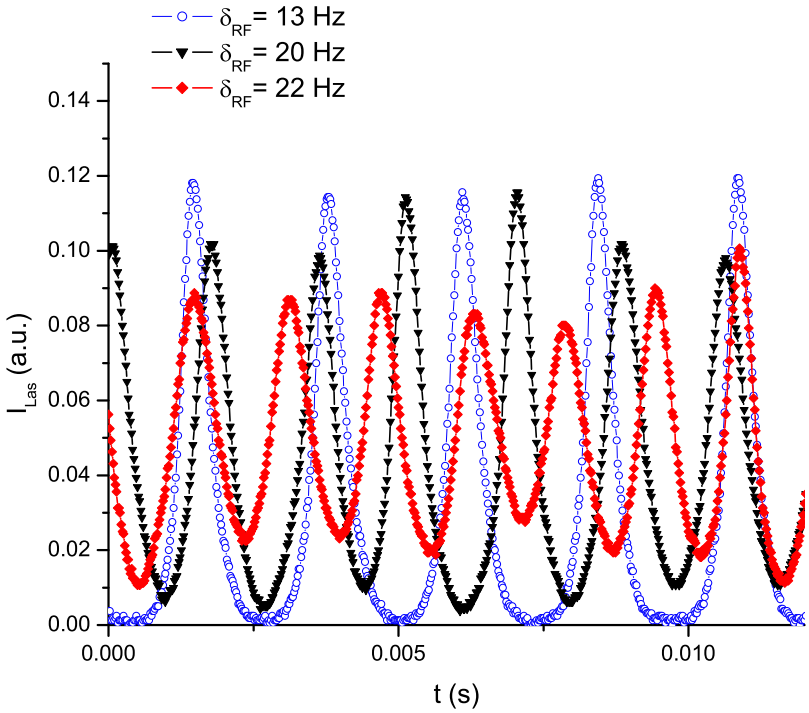

Figure 5.4: *Laser macro-temporal behavior in zone 4 measured at Super ACO. The laser appears pulsed ($\delta\nu_{RF} = 13$ Hz) and modulated ($\delta\nu_{RF} = 20, 22$ Hz).*

different values of the MI excitation parameter. We remark that the laser starts up at a positive threshold effective gain which depends on the MI excitation parameter: the larger this parameter the larger the effective gain needs to be to compensate the gain reduction due to the MI. A second remark is that when the laser starts with sufficient gain, the MI has no effect on the saturation value. The laser has switched off the MI. Figure (5.8) shows the dimensionless intra-cavity power at saturation as function of the detuning and for several value of the MI excitation parameter, for the case of Super ACO. The width is also dependent on the MI strength. This dependency also illustrates the competition between the laser and the MI [17]. At maximum detuning, the laser intensity is at the limit at which the laser-induced energy spread prevents the MI to start. For larger detuning the intra-cavity power is too low to induce sufficient energy spread for preventing the MI to start. As a consequence, at maximum detuning the MI starts, switches the laser off. The maximum detuning depends also on the MI strength so that the detuning curve width can be reduced with a stronger instability. A further remark is that at maximum detuning the level of energy spread induced by the laser is at the threshold for which the MI may start. This value of the energy spread is linked to the impedance of the ring so that the detuning curve may provide a means to measure the storage ring impedance.

From the same simulation one can also retrieve the laser pulse duration vs. detuning, as shown in figure (5.6(b)). The curve is symmetrical and the laser pulse duration increases with the detuning. It is minimum for a very narrow detuning range around

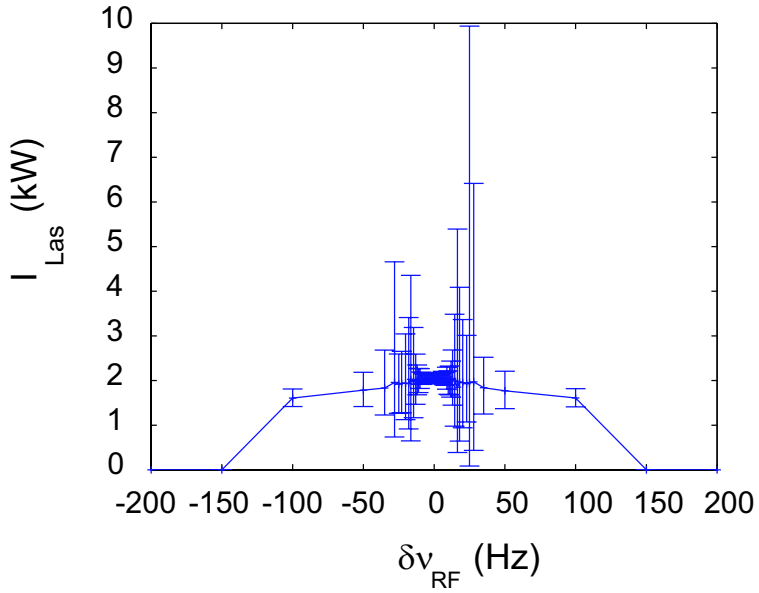

(a) Super ACO case

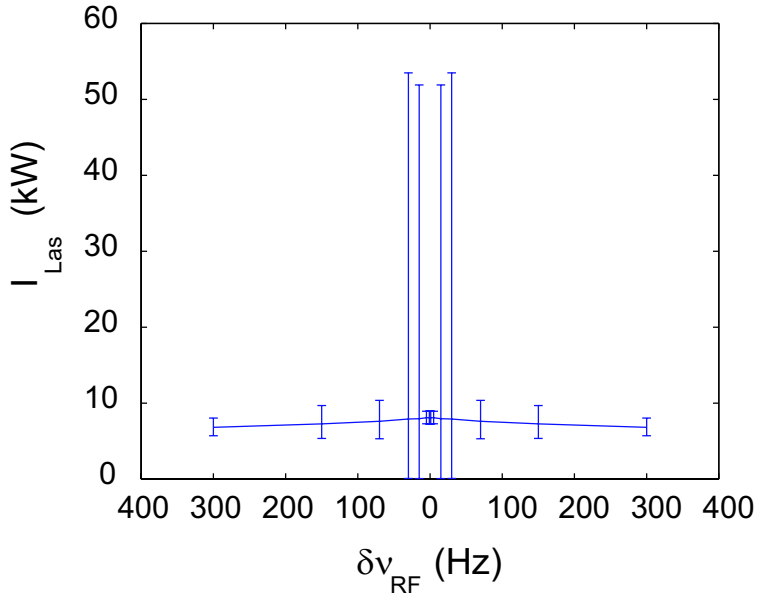

(b) ELETTRA

Figure 5.5: *Numerical detuning curves for the cases of Super ACO and ELETTRA. The machine parameters used in the code correspond to the ones figure in 5.1, and can be seen in table (5.1) .*

$\delta\nu_{RF} = 0$. In this range, the laser operates near the Fourier limit [15]. Any longitudinal instability, e.g. of the electron beam, can push the laser out of this narrow detuning zone. To maintain the laser in zone 3 against longitudinal instabilities a feedback system [18] has been developed at Super ACO. Using this system, we observed that the laser operates closer to the Fourier limit than in the zone 3 without feedback. The curve is in good agreement with measurements, giving a minimum pulse duration (r.m.s) $\sigma_{Las} = 20$ ps for Super ACO. Similar simulation for ELETTRA gives $\sigma_{Las} = 3$

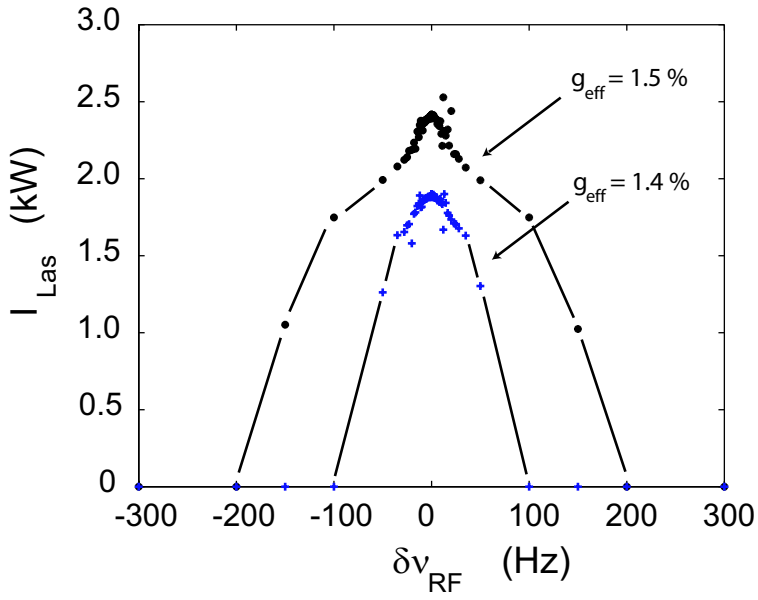

(a) Power vs. $\delta\nu_{RF}$

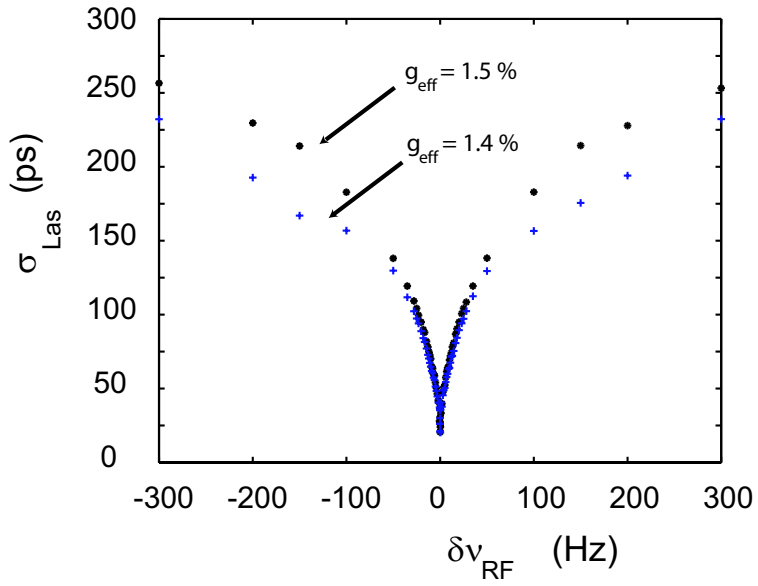

(b) σ_{Las} vs. $\delta\nu_{RF}$

Figure 5.6: *Numerical detuning curves for the Super ACO case, $I = 70$ mA, $g_0 = 2.5\%$ and the effective gain $g_{eff} = 1.5$ for (*) and $g_{eff} = 1.4$ for (+). Figure (5.6(a)) presents the curve laser power vs. detuning. Figure (5.6(b)) shows the pulse duration retrieved from the same simulation.*

ps in agreement with figure (5.2(b)). This justifies the approximations applied in our code.

In summary, a relatively good quantitative agreement with experimental results has been found. The detuning curve presents five characteristic zones where the lasers macro-temporal behavior is cw or modulated. The detuning curves are relatively symmetrical, except when the electron bunch longitudinal distribution is not symmetrical. The width of the detuning curve depends on the gain, but also on the cavity loss and

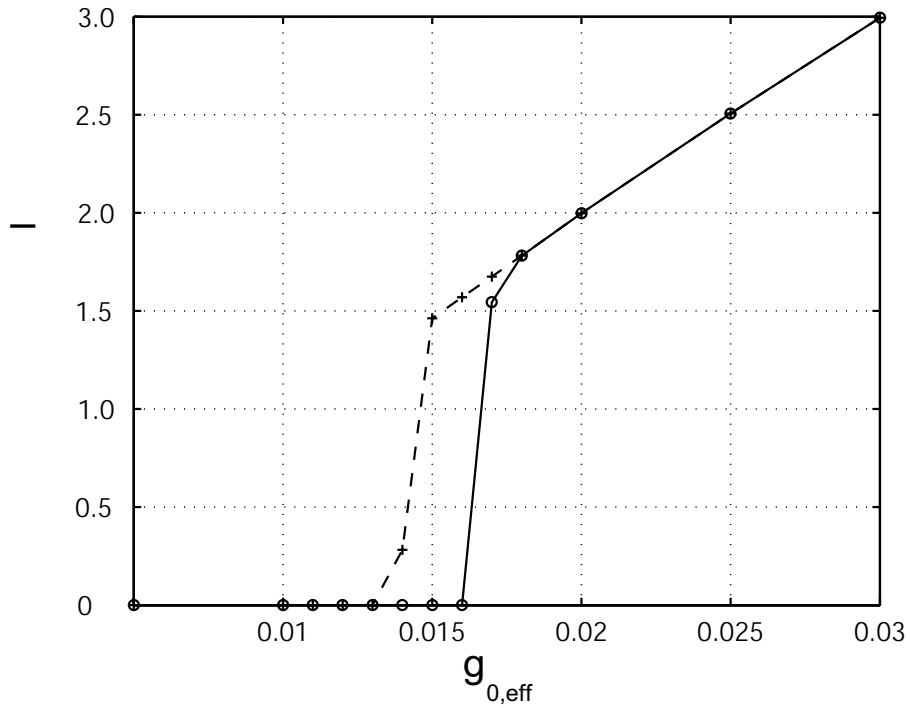

Figure 5.7: *Numerical dimensionless intra-cavity power, I, in zone 3, for the case of Super ACO, as function of the effective gain and for two different values of the MI excitation parameter: the lower MI parameter value corresponds to the crosses and the higher to the circles.*

on the MI strength. The curve characteristics and the dependency on the bunch distribution, should provide a deeper understanding of the dynamical interaction between the laser pulse and the electron bunch. The laser pulse duration is minimum, as well as the spectral width is found in a very narrow detuning range. In this range the laser operates near the Fourier limit.

5.4 Conclusion

A comparison of the measured dynamics of two SRFELs with numerical results has been done by studying the behavior of the laser as function of the longitudinal detuning. The model we implemented in our simulation code gives quantitative agreement for each of the two experimental cases. Detuning curves give certain laser properties (intensity, pulse width, etc) as function of detuning. Their characteristics are dependent on the coupled dynamical system properties. The detuning curve exhibit five characteristic zones where the laser appear cw and modulated. The width depends on the effective gain, but also on longitudinal instabilities such as the microwave instability. The laser pulse length is minimum only in a narrow detuning range around $\delta\nu_{RF} \approx 0$. This shows the importance of incorporating a feedback system, as mentioned in section 3, when the laser is operating for user applications that require a laser functioning near the Fourier limit. The laser is in competition with the microwave instability. The maximum detuning provides the level of energy spread where the microwave instability competes with the laser. Furthermore it can be used to evaluate the normalized impedance of a

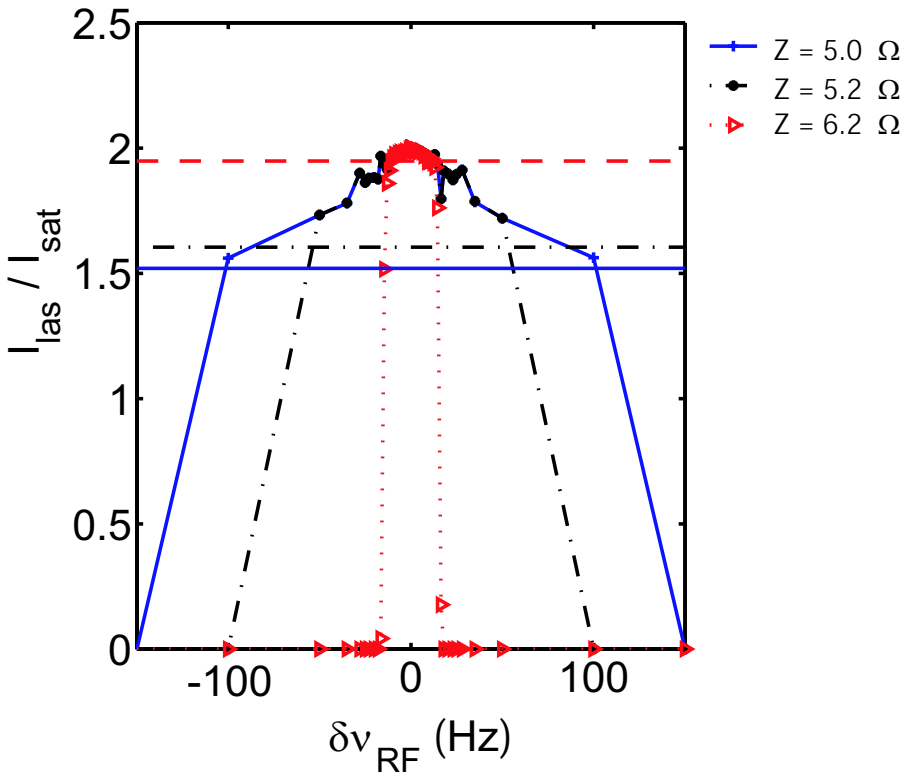

Figure 5.8: *Numerical dimensionless intra-cavity power vs. detuning, for the case of Super ACO, and for several values of the MI excitation parameter, corresponding to a given normalized impedance Z. The horizontal lines corresponds to the Boussard threshold.*

storage ring.

References

[1] J. M. J. Madey. Stimulated emission of bremmstrahlung in a periodinc magnetic field. *Jounal of Applied Physics*, 42(5):1906, 1971.

[2] N. A. Vinokurov and A. N. Skrinsky. *Preprint 77-59*. Nuclear Physics Institute of Novossibirsk, 1977.

[3] M. Billardon, D. Garzella, and M. E. Couprie. Saturation mechanism for a storage-ring free-electron laser. *Physical Review Letters*, 69:2368–2371, October 1992.

[4] G. Dattoli, A. Dipace, E. Sabia, A. Torre, G. K. Voykov, and M. Carpanese. A simple three-dimensional free electron laser code. *Journal of Applied Physics*, 80:6589, December 1996.

[5] G. Dattoli, L. Mezi, M. Migliorati, and L. Palumbo. A simple model for the saw-tooth instability in storage rings. *Nuovo Cimento A Serie*, 112:491, May 1999.

[6] V. N. Litvinenko, B. Burnham, J. M. J. Madey, and Y. Wu. Giant laser pulses in the Duke storage ring UV FEL. *Nuclear Instruments and Methods in Physics Research A*, 358:334, February 1995.

[7] V. N. Litvinenko, Y. Wu, B. Burnham, and J. M. J. Madey. Expected performance of the mm-wave isochronous FEL at the Duke storage ring. *Nuclear Instruments and Methods in Physics Research A*, 358:349, February 1995.

[8] G. de Ninno, M. E. Couprie, D. Nutarelli, D. Garzella, E. Renault, and M. Billardon. Local energy exchange in a storage-ring free-electron laser. *Physical Review E*, 64:26502, August 2001.

[9] C. A. Thomas, J. I. M. Botman, G. D. Ninno, M. E. Couprie, L. Mezi, and G. Dattoli. SRFEL dynamics investigated with a 1-D numerical code. *Nuclear Instruments and Methods in Physics Research A*, 483:181–185, May 2002.

[10] G. Dattoli, A. Renieri, and G. Voykov. Storage-ring free-electron-laser amplifiers and the microwave instability. *Physical Review E*, 55:2056, February 1997.

[11] G. Dattoli, L. Mezi, M. Migliorati, and L. Palumbo. Storage ring free-electron laser and microwave-type instabilities. *Nuovo Cimento B Serie*, 115:639, June 2000.

[12] G. De Ninno, M. Danailov, B. Diviacco, M. Marsi, and M. Trovó. Laser-electron beam dynamics of the european free electron laser at ELETTRA. In *Proc. of EPAC 2002, (Paris)*, page 799, June 2002.

[13] M. E. Couprie, V. Litvinienko, D. Garzella, A. Delboulbé, M. Velghe, and M. Billardon. Dynamical study of the Super-ACO free electron laser with the dissector. *Nuclear Instruments and Methods in Physics Research A*, 331:37, July 1993.

[14] C. A. Thomas, J. I. M. Botman, C. Bruni, D. Garzella, M. E. Couprie, G. D. Ninno, and G. Dattoli. Longitudinal Detuning for an SRFEL. *to be published in Nuclear Instruments and Methods in Physics Research A*, 2003.

[15] M. E. Couprie, G. De Ninno, G. Moneron, D. Nutarelli, M. Hirsch, D. Garzella, E. Renault, R. Roux, and C. Thomas. Towards the Fourier limit on the super-ACO Storage Ring FEL. *Nuclear Instruments and Methods in Physics Research A*, 475:229, December 2001.

[16] G. De Ninno, D. Fanelli, and M. E. Couprie. Detuned dynamics of a storage ring free electron laser. *Nuclear Instruments and Methods in Physics Research A*, 483:177, May 2002.

[17] R. Bartolini, G. Dattoli, L. Mezi, A. Renieri, M. Migliorati, M. E. Couprie, G. de Ninno, and R. Roux. Suppression of the Sawtooth Instability in a Storage Ring by Free-Electron Laser: An Example of Nonlinear Stabilization by Noise. *Physical Review Letters*, 87:134801, September 2001.

[18] M. E. Couprie, D. Garzella, T. Hara, J. H. Codarbox, and M. Billardon. A longitudinal feedback for the Super-ACO free electron laser stability in the UV. *Nuclear Instruments and Methods in Physics Research A*, 358:374, February 1995.

Chapter 6

Conclusions

The storage ring free electron laser is a powerful, continuously tunable laser in the UV-VUV wavelength range. This laser is a unique tool to perform two-color time-resolved spectroscopy, using both the laser and the synchrotron light which are naturally synchronized. For this type of experimental analysis the stability of the laser and of the stored electron beam is an issue. With the operation of a free electron laser on a storage ring, the electron beam is composed of only a few bunches (2 in Super ACO, 4 in ELETTRA). The charge per bunch has to be high to assure a sufficient laser gain. Because of this, all storage rings used for free electron laser operation are affected by an instability called the microwave instability, which can seriously perturb the electron beam and limit the laser performance.
The main goal of this thesis is to provide understanding of the behavior of the storage ring free electron laser in the presence of the microwave instability and to predict this behavior for a specific storage ring free electron laser. To this end we developed a numerical code that has been validated with measurements performed at Super ACO and at ELETTRA.

0-dimensional model

In order to describe qualitatively the storage ring free electron laser dynamics, a '0-dimensional' model for the laser behavior has been presented. With the term 0-dimensional we mean that we restrict ourselves to the description of the evolution of the laser intensity and the electron beam energy spread, assuming perfect overlapping between Gaussian laser pulses and Gaussian electron bunches. The Intensity and the electron energy spread are strongly coupled. The model predicts analytically the saturation of the laser and the induced energy spread to the beam by the laser.
Moreover, a simple model of the beam behavior in presence of the microwave instability has been presented separately. This describes the on set, the growth and the damping of the microwave instability in the beam. We have coupled the 0-dimensional storage ring free electron laser model with that of the microwave instability evolution. The new system obtained is a 0-dimensional model of the storage ring free electron laser in presence of the microwave instability. This gives the general behavior of the system and illustrates the competition of the free electron laser with the instability. With

specific initial values for the free electron laser gain, the cavity loss and the microwave instability strength, the system evolves towards two situations: the laser reaches saturation with damping of the instability, or, the microwave instability wins, and the laser is switched off.

1-DIMENSIONAL MODEL

Successful as the 0-dimensional model has shown to be in the qualitative description of many storage ring free electron laser phenomena, we nevertheless wanted more quantitative predictions, for which a so-called 1-dimensional code was developed. Here with 1-dimensional we mean that the longitudinal coordinate, the propagation axis, is taken into account, i.e. the laser electric field is calculated as a function of the longitudinal coordinate. The model integrates three differential equations. The first two equations account for the stored electron beam behavior, neglecting the potential well distortion effect, assuming the bunch length proportional to the relative energy spread, and including the microwave instability effects. The third equation describes the evolution of the intra-cavity electric field of the free electron laser pulse along the optical cavity axis. For the evaluation of the laser gain along the optical axis, the longitudinal phase-space of the beam is taken into account, which provides the coupling with the electron beam. The coupling is reinforced by the laser induced energy spread, which is also taken into account in the first equation.
To understand deeper the effect of the wakefield on the electron beam, described with the impedance of the ring, we present the analytical solution of the Haissinski equation for purely resistive impedance, and we solve analytically the equation for a purely inductive impedance. The two solutions give a clear picture of the effects of the wakefield on a the electron bunch distribution. Moreover, the solution of the Haissinski equation provides a measure of the storage ring impedance by fitting the longitudinal beam distribution. This quantity provides information on the microwave instability strength. The perturbation from the wakefield may not be damped, inducing an instability to the beam. The beam undergoes then typical oscillations, like for example the sawtooth-like periodic oscillations of the beam energy spread and the electron bunch length, or the coherent synchrotron oscillations. The microwave instability also induces an average enhancement of the beam energy spread, which is always accompanied by a proportional electron bunch lengthening.
The behavior of the storage ring free electron laser is quantitatively understood, in particular the competition of the laser with the microwave instability. A typical range of current for stable operation is found in which range the laser is able to damp the microwave instability. There is a maximum current value above which the laser can not start, in spite of a positive effective gain, due to the on set of the microwave instability. The laser pulse characteristics, pulse duration, peak power, etc., can be retrieved from the simulation results. The code also allows to study the laser behavior under 'detuning' conditions. The detuning is an important parameter for the dynamics of the storage ring free electron laser. The behavior of the free electron laser changes with the detuning, and the performance of the laser degrades. Maximum power and the shortest pulse duration are found at zero detuning. The code has shown the laser to be 'cw' for small and large detuning values, and modulated for intermediate detuning

values.

VALIDATION BY EXPERIMENTS

As stated above the laser behavior is intimately connected with the electron beam properties. Experimental characterization of the Super ACO electron beam behavior has been carried out. To a large extent the behavior of the beam for free electron laser operation at Super ACO is understood. The role of the wakefield, e.g. the perturbation it gives to the electron beam, is important. The measurements have shown a stable behavior of the beam, where the bunch characteristics are described by the Haissinski equation, and an unstable behavior, dominated by the microwave instability.
The free electron laser characteristics, pulse duration, power at saturation, gain at start-up, etc., have been measured at Super ACO and at ELETTRA. The measurements have been done at perfect longitudinal tuning, and under detuning conditions. The detuning curves, giving laser characteristics as a function of the detuning, exhibit five characteristic zones where the laser is cw, for small and large detuning, and modulated, for intermediate detuning. In particular the laser is found to be nearly Fourier limited in a narrow range of the central detuning zone. The properties of the detuning curves are linked to the parameters determining the dynamics of the storage ring free electron laser, such as the gain at start-up, the cavity loss and the microwave instability strength. The code has been used to simulate successfully the behavior of the Super ACO and the ELETTRA free electron lasers. The laser power, the laser pulse duration, and the laser regime as a function of the detuning have been found to be in a quantitative agreement with measurements.

CONCLUDING REMARKS

The numerical code has been applied successfully to simulate two different storage ring free electron lasers. The code can be used as a tool for the design of new storage ring free electron lasers, or for optimization of existing ones.
The study of the behavior of the storage ring free electron laser in presence of the microwave instability has clarified the important role of the instability for the free electron laser dynamics. The numerical code we implemented, combined with the experimental studies has shown the limitation of the performance of the laser due to the instability. The microwave instability strength depends on the storage ring impedance. A smaller impedance provides a better free electron laser, in terms of stability, power, pulse duration and spectral bandwidth, over a larger range of current. The numerical code and the measurements have shown that the microwave instability in particular perturbs the laser performance. The code has shown, in agreement with experiments, that at perfect tuning the laser is cw and has a minimum pulse duration; with the microwave instability the pulse duration is longer than without, demonstrating the necessity of having a feedback system, to maintain the laser at perfect tuning, for time-resolved experiments.
The microwave instability is an issue in the design of a stable and powerful storage ring free electron laser. The impedance of the storage ring has to be as low as possible in order to operate the laser at a sufficient power with the stability required for

applications.

Perspectives

The numerical code gives reliable results and can be used for the design of new storage ring free electron lasers. However the code does not describe the effects due the potential well distortion. In particular, the assumption of the asymmetry of the detuning curves, resulting from the distortion of the bunch longitudinal distortion, may be verified. Modelling the transverse effects might also slightly improve the code. Transverse perturbations of the beam induce transverse oscillations that are too fast to be followed by the free electron laser. Then the effect may be a reduction of the gain proportional to the average cross section seen by the free electron laser.
The impedance of the storage ring is a crucial issue. In order to enhance stability and performance of the free electron laser a very low impedance has to be designed, which requires careful choice of the materials used for building the vacuum chamber and on the geometry of the vacuum chamber.

Summary

The purpose of the present work is to study the dynamics of the storage ring free electron laser in the UV-VUV wavelength range and in the presence of the microwave instability. In practice this instability is always present during the operation of a free electron laser in a storage ring, and it may degrade the performance of the laser.
In order to investigate the behavior of this complex system, we used a dual approach, in which theoretical results have been compared with measurements performed on two storage ring free electron lasers, at Super ACO (France) and at ELETTRA (Italy).
As a first theoretical step, we analyzed a simple model which describes qualitatively the behavior of the storage ring free electron laser only, including the effects due to the microwave instability. In order to get more quantitative predictions, which can not be obtained from the simple model, we developed a 1-dimensional numerical code for the evolution of the laser electric field along the optical cavity axis. The code was validated by the comparison with experimental measurements performed at Super ACO and at ELETTRA.
The experimental approach has also been done in two steps. The first step was to characterize the electron beam behavior in the storage ring without the free electron laser. This has only been done at Super ACO. We measured the beam characteristics (electron distribution, beam energy spread, etc.) for the free electron laser operation, and we characterized two effects of the wakefield on the electron beam. The first effect is the so-called potential well distortion, which only modifies the beam properties, leaving the beam stable. The second effect induces instabilities in the beam, in particular the microwave instability, with on average an enhancement of energy spread and a proportional bunch lengthening. Next we characterized the laser behavior, measured the laser pulse properties (pulse duration, average power, etc.) under detuning conditions, and deduced from measurements the parameters of the dynamical system, such as the gain at start-up, the cavity loss, etc.
The main conclusion of the present work is that the microwave instability can seriously degrade the performance of the storage ring free electron laser. For any design of such a system one has to make sure that the impedance of the storage ring, which scales the strength of the microwave instability, is as low as possible. The laser is in competition with the instability, and is able to damp it in a range of current determined by the gain of the free electron laser, the optical cavity loss and the microwave instability strength. At higher current the laser is unstable, or simply, it may be switched off by the microwave instability.
The numerical code we developed has been used to simulate successfully the behavior of two different storage ring free electron lasers. It can be used reliably as a tool for the design of new storage ring free electron lasers.

Résumé

L'objectif principal de ce travail est l'étude de la dynamique du laser à électron libres sur anneaux de stockage, dans le domaine spectral UV-VUV et en présence de l'instabilité micro-onde. Cette instabilité affecte tous les anneaux de stockage en fonctionnement pour le laser à électrons libres.
Une étude à la fois théorique et expérimentale du comportement de ce système a été mise en place, dans laquelle les résultats théoriques ont été comparés aux mesures effectuées à Super ACO (France) et à ELETTRA (Italie).
Dans un premier temps, le comportement du système en présence de l'instabilité micro-onde est décrit qualitativement par un modèle simple. Ensuite, dans le but de prédire de façon quantitative le comportement du faisceau, nous avons développé un code numérique unidimensionel de la dynamique du laser à électrons libres sur anneau de stockage en présence de l'instabilité micro-onde. Le code décrit l'évolution du champ électrique du laser dans la cavité optique, couplée à l'évolution du faisceau d'électrons dans l'anneau, et a été validé par comparaison avec les résultats expérimentaux obtenus à Super ACO et ELETTRA.
L'étude expérimentale nous a amené en premier lieu à caractériser le comportement du faisceau dans l'anneau de stockage. Ceci a été effectué seulement à Super ACO. Nous avons mesuré les caractéristiques du faisceau d'électrons (distribution électronique, dispersion en énergie, etc.) pour le fonctionnement du laser à électrons libres, et nous avons caractérisé deux effets du champs de sillage sur le faisceau d'électrons. Le premier effet, communément appelé la "distortion du puits de potentiel", modifie les caractériques du faisceau sans générer aucune instabilité. Le deuxième effet du champ de sillage est la génération d'instabilités dans le faisceau d'électron, en particulier l'instabilité micro-onde. Cette instabilité induit en moyenne sur le temps un accroissement de la dispersion en énergie, qui s'accompagne d'un accroissement de la longueur des paquets d'électrons dans l'anneau. Ensuite nous avons caractérisé le comportement du laser, mesuré les caractéristiques de l'impulsion laser sous différentes conditions de désaccord, i.e. synchronisation entre l'impulsion laser et les paquets d'électrons. Les paramètres du système dynamique, tels que le gain, les pertes de la cavité optique etc., ont été déduits de ces mesures.
La principale conclusion de ce travail est que l'instabilité micro-onde peut sérieusement dégrader les performances du laser à électrons libres sur anneau de stockage. Pour tout projet de construction d'un tel système, l'impédance de l'anneau de stockage, qui régit la puissance de l'instabilité micro-onde, doit être la plus petite possible. Le laser est en compétition avec l'instabilité micro-onde, et est capable de l'amortir dans une plage de courant dont la borne supérieure est déterminée par le gain, les pertes de la cavité optique, et la puissance de l'instabilité. Pour des courants supérieurs, le laser n'est pas

stable, ou est tout simplement éteint par l'instabilité.
Le code numérique que nous avons développé a été utilisé pour simuler avec succès le comportement de deux lasers à électrons libres. Il peut donc être utilisé comme outil pour l'étude de tout nouveau laser à électrons libres sur anneau de stockage.

Samenvatting

Het onderwerp van dit proefschrift is de studie van de dynamica van vrije elektronen lasers in opslagringen, in het UV-VUV golflengte gebied, in aanwezigheid van de zogenaamde 'microwave' instabiliteit. In de praktijk is deze instabiliteit altijd aanwezig in de opslagring bij het gebruik van een dergelijke vrije elektronen laser, en kan de werking van de laser nadelig beïnvloeden. Om het gedrag van dit complexe systeem te bestuderen, hanteerden we een tweeledige aanpak, waarin theoretische resultaten werden vergeleken met metingen uitgevoerd aan twee faciliteiten, namelijk die van Super ACO, Frankrijk en ELETTRA, Italië.
Als eerste theoretische stap gebruikten we een eenvoudig kwalitatief model van een vrije elektronen laser in een opslagring waarbij effecten ten gevolge van de 'microwave' instabiliteit werden meegenomen. Om kwantitatieve voorspellingen te verkrijgen, hetgeen niet mogelijk is met het vereenvoudigde model, ontwikkelden we een 1-dimensionale numerieke code voor de berekening van de groei van het elektrische veld van de laser langs de as van de optische trilholte. De uitkomsten van de code bleken goed overeen te stemmen met metingen aan de systemen van Super ACO en ELETTRA.
De experimenten zijn ook in twee stappen gedaan. De eerste stap was het karakteriseren van het gedrag van de elektronenbundel in de opslagring in afwezigheid van een vrije elektronen laser. Dit werd uitsluitend gedaan bij Super ACO. We maten de bundeleigenschappen (elektronenverdeling, energiespreiding van de bundel, en dergelijke) zoals die gelden bij het werken met de laser, en we karakteriseerden twee effecten van het gereflecteerde veld van de elektronenbundel op die zelfde bundel. Het eerste effect is de 'potential well' verstoring die op zich de stabiliteit van de bundel niet aantast, maar wel bundeleigenschappen verandert. Het tweede effect houdt in het aanslaan van instabiliteiten in de bundel, in het bijzonder de 'microwave' instabiliteit, met gemiddeld een vergroting van de energiespreiding en een evenredige vergroting van de lengte van de elektronenpulsen. Vervolgens karakteriseerden we het gedrag van de laser: we hebben de eigenschappen van de laserpuls (pulsduur, gemiddeld vermogen, etcetera) gemeten bij verstemming van de optische trilholte, en bepaalden hiermee de parameters van het dynamische systeem, zoals de aanvangsversterking, het vermogensverlies, en dergelijke.
De hoofdconclusie van dit proefschrift is dat de 'microwave' instabiliteit de goede werking van de laser ernstig kan verstoren. Bij het ontwerp van een vrije elektronen lasersysteem in een opslagring dient men erop toe te zien dat de impedantie van de ring, die de sterkte van de instabiliteit bepaalt, zo laag mogelijk is. De laser verkeert in competitie met de instabiliteit, en is in staat de instabiliteit te dempen voor zekere waarden van de bundelstroom, afhankelijk van de versterking van de laser, het vermogensverlies in de optische trilholte en de sterkte van de instabiliteit. Bij hogere bundelstroom is de

laser óf instabiel, óf hij schakelt uit ten gevolge van de instabiliteit. Met de numerieke code die door ons is ontwikkeld, is het gedrag van vrije elektronen lasersystemen in twee verschillende opslagringen met succes gesimuleerd. De code kan als betrouwbaar hulpmiddel gebruikt worden bij het ontwerp van nieuwe systemen.

Acknowledgements

I would like to express my thankfulness to all the people that have been involved at various degrees in the accomplishment of this research work. I am grateful to them for their help, for their patience, for the examples they have been to me.
Jan, ik heb veel te vertellen, je bent een echte gids geweest, door nooit je mening op te gringen, altijd open voor discussie, je heb altijd zaken voldoende toegelicht om mij mijn eigen weg te laten kiezen. Ik leerde een hoop van jou. Hartelijk bedankt.
Marnix, bedankt voor je voorbeeld als groepsleider, als manager, en als fysicus met een scherpe en brede blik.
Marie Emmanuelle, merci pour m'avoir permis de faire cette thèse et de m'avoir mis le pied à l'étrier. Je te remercie pour toute l'énergie et la bonne volonté que tu mets dans ton travail et pour l'exigence que tu as envers celui des autres. Merci.
David, è sempre un piacere lavorare con te. Ho imparato molto durante le lunghe ore dei turni notturni, sempre in un ambiente positivo e stimolante. Ti apprezzo molto anche come persona, e condivido i tuoi valori, il tuo rispetto, la tua franchezza, e quel certo tuo modo di apprezzare le cose belle della vita.
Pino e Alberto, voglio ringraziarvi entrambi per la considerazione in cui mi avete tenuto. È stato un grande onore per me collaborare con voi e sarà un grande piacere seguire l'esempio che mi avete dato.
I am thankful to Jom, Fred, Walter, Gianluca, and Seth for the help they provided to me, for the useful discussions that we had, and for the good working atmosphere.
I thank also Giovanni, Christelle, Gian Luca, and all the other people of the Orsay FEL group for their collaboration during the shifts, and their efforts to make the experiments working.
I am gratefull to the members of the committee who read the manuscript for the enlightening discussions, and the maturation of the manuscript during the writing process.
I would like to thank my friends, Sylvie, Margot, Vincent, Maud, Jean-Charles, Gabriel, who gave me support and encouragements, specially during the last months.
Sigolène, je te remercie pour ton support moral, ta patience et pour m'avoir accordé tout ce temps que nous aurions pu passer ensemble.
I would like to thank all the others that I did not mentioned, I wish I could name all of them, but I simply say: thank you.
Enfin je tiens à rendre hommage à ma famille, à ma mère, à ma soeur, et particulièrement à Jacky et Marie Joe pour leur confiance et leur soutien.

List of publications

1. C.A. Thomas, J.I.M. Botman, C. Bruni, D. Garzella, M.E. Couprie, G. De Ninno, G. Dattoli, "Storage Ring Free Electron Laser Dynamics: Longitudinal Detuning Study", *submitted to Phys. Rev. Special Topics*, (2003).

2. C.A. Thomas, J.I.M. Botman, C. Bruni, G. De Ninno, D. Garzella, D. Nutarelli, R. Roux, M.E. Couprie, "Storage Ring Free Electron Laser dynamics in presence of a auxiliary harmonic Radio Frequency cavity", *submitted to Phys. Rev. E*, (2003).

3. C.A. Thomas, J.I.M. Botman, M.J. Van der Wiel, G. Dattoli, "Undulator vs. optical klystron induced dynamics of a storage ring free electron laser", *to be published in Nucl. Instr. and Methods in Physics Research* ***A***, (2003).

4. C.A. Thomas, J.I.M. Botman, C. Bruni, D. Garzella, M.E. Couprie, G. De Ninno, G. Dattoli, "Longitudinal Detuning for an SRFEL", *to be published in Nucl. Instr. and Methods in Physics Research* ***A***, (2003).

5. C. Thomas, J.I.M. Botman, R. Bartolini, G. Dattoli, L.Mezi, M. Migliorati, "An analytical solution for the Haissinski equation with purely inductive wake fields, Europhysics Letters, **60**, p. 66, (2002).

6. C. Thomas, J.I.M. Botman, R. Bartolini, G. Dattoli, M. Migliorati, "Longitudinal beam distribution in a storage ring with pure inductance described by the LambertW function", *Proc. EPAC 2002*, p. 1565, Paris, June, (2002).

7. C. Thomas, J.I.M. Botman, B. van de Geer, M. de Loos, "Investigation of FEL gain in the optical klystron configuration with the GPT simulation code", *Proc. EPAC 2002*, p. 843, Paris, June, (2002).

8. Thomas, C. A., Botman, J. I. M., Ninno, G. D., Couprie, M. E., Mezi, L., Dattoli, G., "SRFEL dynamics investigated with a 1-D numerical code", Nucl. Instr. and Methods in Physics Research **A**, 483, p. 181, (2002).

9. C.A. Thomas, J.I.M. Botman, "Simulations on Harmonic Generation with the Particle Tracking Code GPT", *Proc. of PAC 2001*, p. 2763, Chicago, June, (2001).

10. C.A. Thomas, J.I.M. Botman, C.A.J. van der Geer, M.E. Couprie, "Simulation of laser - electron beam interaction in the optical klystron of A free electron laser", *Proc. EPAC 2000*, p. 776, Vienna, June, (2000).

11. G. De Ninno, C. Bruni, D. Nutarelli, D. Garzella, C. A. Thomas, M. E. Couprie, "Steady state of a fully detuned storage ring Free Electron Laser", *to be published in Phys.Rev. E*, (2003).

12. C. Bruni, G. De Ninno, D. Garzella, A. Nadji, C.A. Thomas, M.E. Couprie, R. Bartolini, L. Giannessi, "Super-ACO free-electron laser (FEL) operation with a reduced momentum compaction factor", Nucl. Instr. and Methods in Physics Research **A**, 483, p. 167, (2002).

13. C. Bruni, M.-E. Couprie, D. Garzella, G. De Ninno, C.A. Thomas,"Super-ACO FEL Dynamics for Different Experimental Conditions", *Proc. of EPAC 2002*, p. 793, Paris, June, (2002).

14. D. Garzella, C. Bruni, M.-E. Couprie, G. De Ninno, C.A. Thomas,"Small Signal Gain of the Super ACO Storage Ring FEL", *Proc. of EPAC 2002*, p. 805, Paris, June, (2002).

15. M.E. Couprie, G. De Ninno, G. Moneron, D. Nutarelli, M. Hirsch, D. Garzella, E. Renault, R. Roux, C.A. Thomas, "Towards the Fourier limit on the super-ACO Storage Ring FEL", Nucl. Instr. and Methods in Physics Research **A**, 475, p. 229, (2001).

16. G. Dattoli, L. Mezi, M. Migliorati, A Renieri, M.E. Couprie, D. Garzella, D. Nutarelli, C.A. Thomas , G. De Ninno, R. Walker, "Electron beam properties and impedance characterization for storage rings used for free electron lasers", Nucl. Instr. and Methods in Physics Research **A**, 471, p. 403, (2001).

Curriculum Vitae

1972	Born in Pessac (*France*)
1992	French Baccalauréat in Mathematics and Physics (Libourne, *France*)
1992-1997	Physics at Université Bordeaux I (*France*)
1995	First scuba-diving diploma
1998	Military service
1999-2003	Ph-D Research at the Department of Applied Physics, *Technische Universiteit Eindhoven, TU/e (Nederland)* and at LURE *Université Paris XI, Orsay (France)*